Spectroscopic and Adaptive Optics Observations of Protostellar Magnetospheres and Binary Star Evolution

By

Stefan Emile Laos

Dissertation

Submitted to the Faculty of the

Graduate School of Vanderbilt University

in partial fulfillment of the requirements

for the degree of

DOCTOR OF PHILOSOPHY

in

Astrophysics

August 13, 2021

Nashville, Tennessee

Approved:

Keivan G. Stassun, Ph.D.

Andreas Berlind, Ph.D.

David Weintraub, Ph.D.

Thomas P. Greene, Ph.D.

DEDICATION

I dedicate this dissertation to, by far, the greatest privilege and blessing in my life: the extraordinary people. Those that make up my immediate and chosen family, those who inspired and believed in me, and those who made the valleys of life feel ever so slightly less deep.

ACKNOWLEDGMENTS

I don't think I'll ever be able to fully express how grateful I am for my support system. Their sustained support can only be described as deep, unnerving, and profound. My life has been graced by so many remarkable people over the years; I'd like to take an (ambitious) moment and thank them all by name. You have all helped me in unique ways, both knowingly and unknowingly, that have truly made what felt like such an absolute lofty dream a reality. At so many points throughout my academic journey, I have sobbed profusely, been severely frustrated, and thought I didn't have what it takes to reach this point in my life. I would like you all to know that it was only through your support I made it here (with mind and body bruised but intact and during a freaking pandemic!).

Starting chronologically, I'd like to thank some of my oldest friends, whom I consider brothers. They have been so supportive of me along the entire way (even before Swarthmore!), patiently lending their ear to offer their empathy as I struggled and fought to get by. The fact that we have been able to remain close despite it all means more to me than any of you know. All of the visits (all over the country), crying laughing from countless nights of playing games like Super Smash Brothers among others, the phone calls, the concerts. The list of experiences I'm grateful to have shared with you all and kept my sanity strong throughout this process is very, very long. In no particular order, Sean, Jairo, Jude, Frankie, Andres, Christina, Cameron, and Danny. Thank you.

Once at Swarthmore, I was once again blessed with another friend group that I am honored to call some of my absolute best friends. Banko, Tushar, and Timmy. You three have very intimately seen me struggle and pushed me forward both during our challenging four years at Swarthmore and afterwards. Our bond has been nothing short of a fundamental pillar of support and one that I hope to keep for the rest of my life. Know it's difficult for me to truly articulate how much I value your collective presence in my life. I'd like to also deeply thank my Swarthmore mentors Eric Jensen and David Cohen. It's no exaggeration when I say I hope I can be a fraction as good of a professor and guide as them one day. I'd also like to sincerely thank the other, vital people who impacted my life during that time (and now!): my music friends (Shruti, Nate, Tiyé, Harsha, and James), my

friends from the Swarthmore Summer Scholar Program, my League of Legends friends (George, Robert, both Davids, Sayed, Mike, Jake, Kevin, and Henri), and Steve. Your collective kindness and our shared experiences are without a doubt some of the fondest memories in my life and got me through the roughest patches of my undergraduate and graduate time. Lastly, I'd like to extend my gratitude to one last Swattie, Tyler Alexander. As my dedicated astronomy (and skiing) pal, your relentless enthusiasm and encouragement brought up my spirits on more than one occasion, and helped remind me to take the time and appreciate again how amazing studying astronomy is.

During my time at Vanderbilt, I have had the privilege of meeting some of the most amazing people to work with. To my mentor, Keivan, who has truly been invaluable to my development as an astrophysicist. For offering your time and patience to proofread our work, answer emails, give advice while still having time to say hi in the hallways. For helping facilitate the once-in-a-lifetime opportunity I had to travel across the world and observe from Maunakea (among numerous workshops and networking). For always having my best interests in mind and believing I was capable of succeeding here. Thank you. Thank you to my amazing co-authors: Bob, Tom, and Joan. Your dedicated feedback has helped sharpen my abilities and made me feel more confident in them. I keep your words close so often. Thank you to my dissertation committee for taking the time to give me detailed feedback throughout this process. To all of my Vanderbilt colleagues, thank you for your company, your presence as a source of inspiration and camaraderie, and all of our shared experiences. I'd like to especially thank Mehnaaz, Victor, Don, Kyle, Laura, and Susan. In each of your own ways, you really made these four years so much more manageable. Similarly, I'd like to thank my other local Vandy and non-Vandy affiliated friends. Thank you Natasha and Joy, my soccer brothers Alex and Piyush, Charles and Sharon, and everyone at Lyra (especially my friend Andrew). You have all helped make Nashville feel like a home away from home, a non-trivial task to say the least.

To my partner Dana, who I met roughly in the middle of my PhD journey and will be starting a new life in Oklahoma with. You alone have shared the best and worst parts of this journey with me. Having to watch me be tested so deeply, offering your love and patience to me over and over again.

I can't thank you enough for all of the times you've stepped in as my proverbial rock. My eternal best friend. All of the times you've let me vent and cry on your shoulder, cooked the most healing meals I've ever eaten, made me bust out laughing, and made me feel so much more confident. I've never met somebody as amazing as you, and I really hope you acknowledge how inspiring your strength is to me, both in your speciality and as a person who knows their worth and fights. It really does feel like it was all meant to be. United with a person that I can't imagine life without now, who's helped me grow so much, to help see me through the impossible. Words will never be enough to capture my feelings towards you. Thank you so much for everything, Dana.

And last, but by no means least, to my parents. Whom, to this day, I still refer to as "mama" and "didi". They have been by my side since the beginning and have always offered their truly unconditional love to me. Without any pressure or judgement, they have supported me on my journey, making the impossible happen time and time again just so I could have the opportunity to pursue and succeed such an arduous task starting with Swarthmore. I hope both of them one day recognize how profound of a positive impact they've had on me. There's no doubt in my mind that our unique bond is an integral part of my strength. I have been spoiled by an infinite reservoir of love and hope to be a fraction as loving every day in my relationships. To my sister, Sydney, who made me smile so much on trips back home and in Nashville, who would keep asking her brother how things were going. To Grandma Barbara, always sending me surprise care packages and beautiful poems. To my cousins, Dylan and Derek, who have always my closest familial bond. To my loving aunts and uncles. To Abeulo Gaston, who I know has been watching over me as I closely follow in his impressive footsteps. We together made this happen. Thank you all so so much.

TABLE OF CONTENTS

Page

LIST OF TABLES

LIST OF FIGURES

Chapter 1

Introduction

Broadly speaking, the field of stellar astrophysics aims to better understand the properties of the large balls of plasma we call stars, as well as the processes they undergo throughout their lives. Starting as early as $\sim$129 B.C., the Greek astronomer Hipparchus was one of the first to seek out the quantification of stellar properties. Using his naked eye observations, he classified stars based on their apparent brightness, which would later evolve into the magnitude system used by astrophysicists today. Significant technological advancements over the past hundred years have provided astronomers with the tools to ask and answer increasingly pointed questions about stars. Modern day astronomy seeks to derive both the intrinsic (e.g., temperature, size, mass, age) and external (e.g., the surrounding environment, companions) characteristics for the plethora of stars we know exist in the night sky. It was quickly discovered that stars at different points of their lives exhibit unique phenomenon. Understanding the complicated physics encoded in these phenomenon serves as the basis for some of the open questions we as stellar astrophysicists work on today. I have been extremely privileged and grateful to work in the specific realm of young stellar evolution for the past four years of my graduate and two years of my undergraduate study. In the following subsections, I introduce and elaborate briefly on the specialities my graduate work focused on.

1.1 Young Stellar Evolution

In its entirety, my work has focused on better understanding the processes stars undergo in the early portions of their lives. As a reference point, a star like our own Sun is approximately 5 billion years old while the stars I study are generally on the order of $\sim$10-30 *million* years old, or still in the process of forming into a bona-fide star (what we call a protostar). At these, relatively speaking, very young stages, stars have a variety of interesting and complicated characteristics in-

cluding: disks, winds, chromospheric activity, mass accretion, jets, outflows, external companions, magnetic fields, and more. Similar to archaeology, observational stellar astrophysicists rely solely on the light from these objects to better understand the details of these phenomenon. Where does this light tend to come from?

We find forming stellar systems in the densest parts of large clouds of dust and gas, many times larger than our Solar System. The significant amount of surrounding material shrouds the inner protostars, often completely attenuating all of the light we can see with our naked eyes (wavelengths of 300-700nm). However, stars, even during formation, are very hot objects that give off light in a variety of shorter and longer wavelengths. Some of this longer wavelength light has the ability to escape the surrounding dust and gas. Just as infrared cameras pick up on the low body temperature of humans, astrophysicists use near-infrared observations to study the very red light of protostars. Figure 1.1 shows an example of an active stellar nursery called the Lagoon Nebula, with young stars hidden at visible wavelengths (left panel) but revealed in the infrared (right panel).

1.1.1 Class 0 Protostars

Many strides forward have been made towards understanding the complicated process of stellar birth. Figure 1.2 displays a rough sketch encompassing our current view for each evolutionary stage of stellar formation. Stated briefly, parts of a large molecular cloud first begin collapsing under the influence of gravity. The high increase of density, and subsequently temperature, in the inner regions of this collapse form a stellar core. This stellar core will quickly grow in mass as the reservoir of dust and gas in the surrounding envelope (indicated in grey, Figure 1.2) falls onto the star (what astrophysicists call ”mass accretion”). Conservation of angular momentum causes a disk of material to form around the protostar (orange). Lastly, we also often see evidence of fast moving ejected material in the outer regions of the system (blue, referred to as jets or a wind).

For many decades, stellar astrophysicists have worked towards characterizing the later stages of this process (Class II and III). These stages have historically been easier to observe, given the

Figure 1.1: Comparison of the Lagoon Nebula observed at visible (left panel) and infrared (right panel) wavelengths. Note the stars revealed behind the intervening dust and gas in the infrared. Credit: NASA, ESA, STScI

lack of an intervening envelope (more light to work with) and are less chaotic than the early stages, which have been particularly difficult to model. Working from the outside in, stellar astrophysicists have begun learning more about the earliest observable stage, Class 0s, at large scales. This work has helped us learn more about their envelopes and disks, and how they compare to that of the later stages. We show an artist's conception of this dynamic protostellar stage in Figure 1.3.

However, little is known about the inner region of Class 0s. In particular, how Class 0s accrete mass from their disk and envelopes to eventually form into a star as massive as our Sun is not well understood at all. The timescale for this process, which is believed to majorly occur during the Class 0 and I phases, is relatively short-lived at only approximately half a million years. Multiple theories have been argued in the literature, each with different underlying mechanisms to feasibly grow the star. As an example, one possible explanation argues an established magnetic field channels material from the inner regions of a stellar disk onto the stellar surface (called magnetopsheric stellar accretion). A schematic of this process is shown in Figure 1.4. Paper I of this dissertation

uses near-infrared observations to help characterize the inner regions of Class 0s and give insight into their mass accretion.

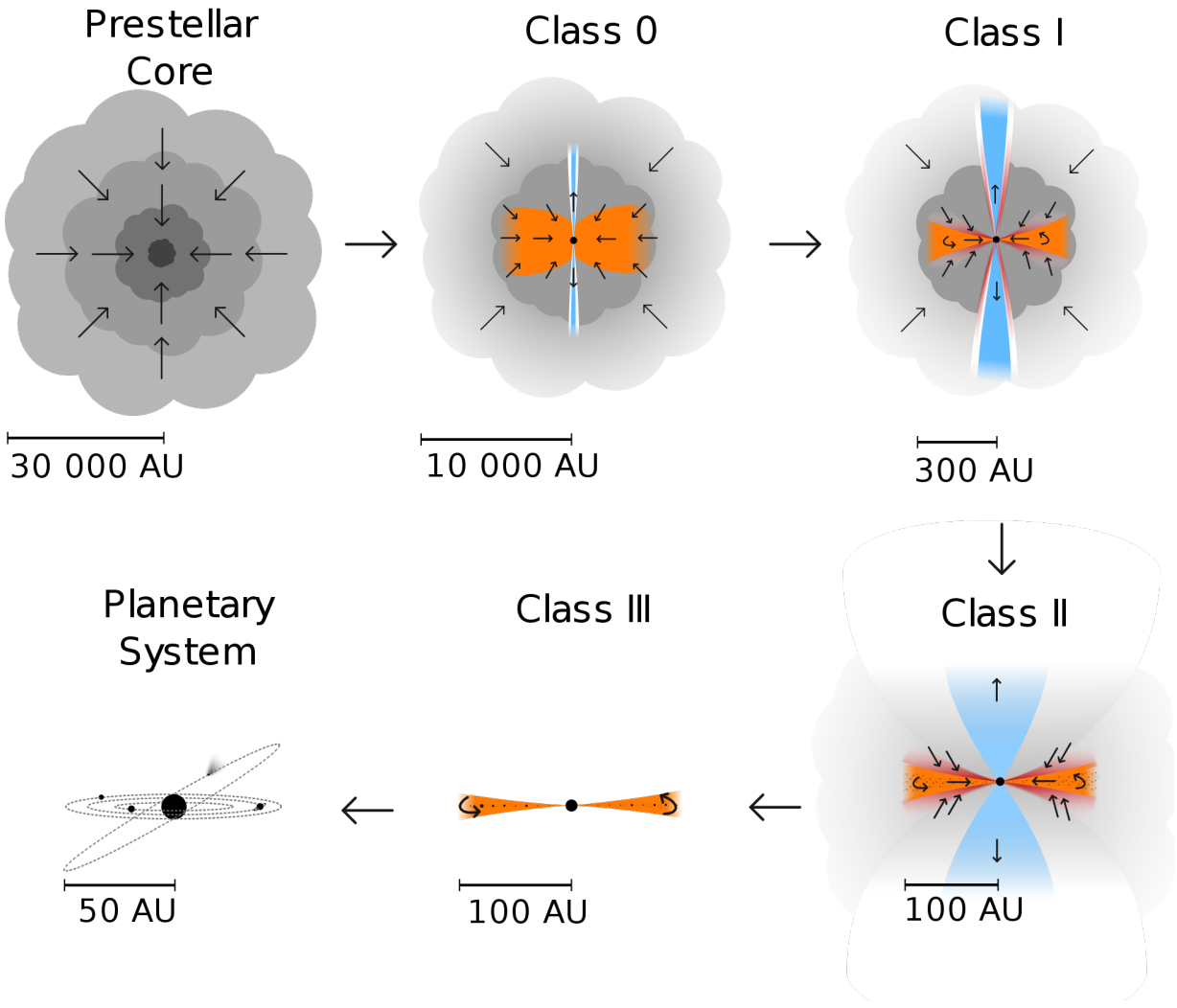

Figure 1.2: A rough sketch of our current view of stellar formation. Paper 1 of this dissertation focuses on the earliest observable evolutionary stage, protostars during the Class 0 phase. Credit: Magnus Vilhelm Pearson

1.1.2 Multiplicity

It is important to note that the simple picture of star formation given in Figure 1.2 does not occur in an isolated vacuum. Our study of prominent star forming regions finds stars often being born in active bursts, within close proximity to one another. This environment naturally evolves to

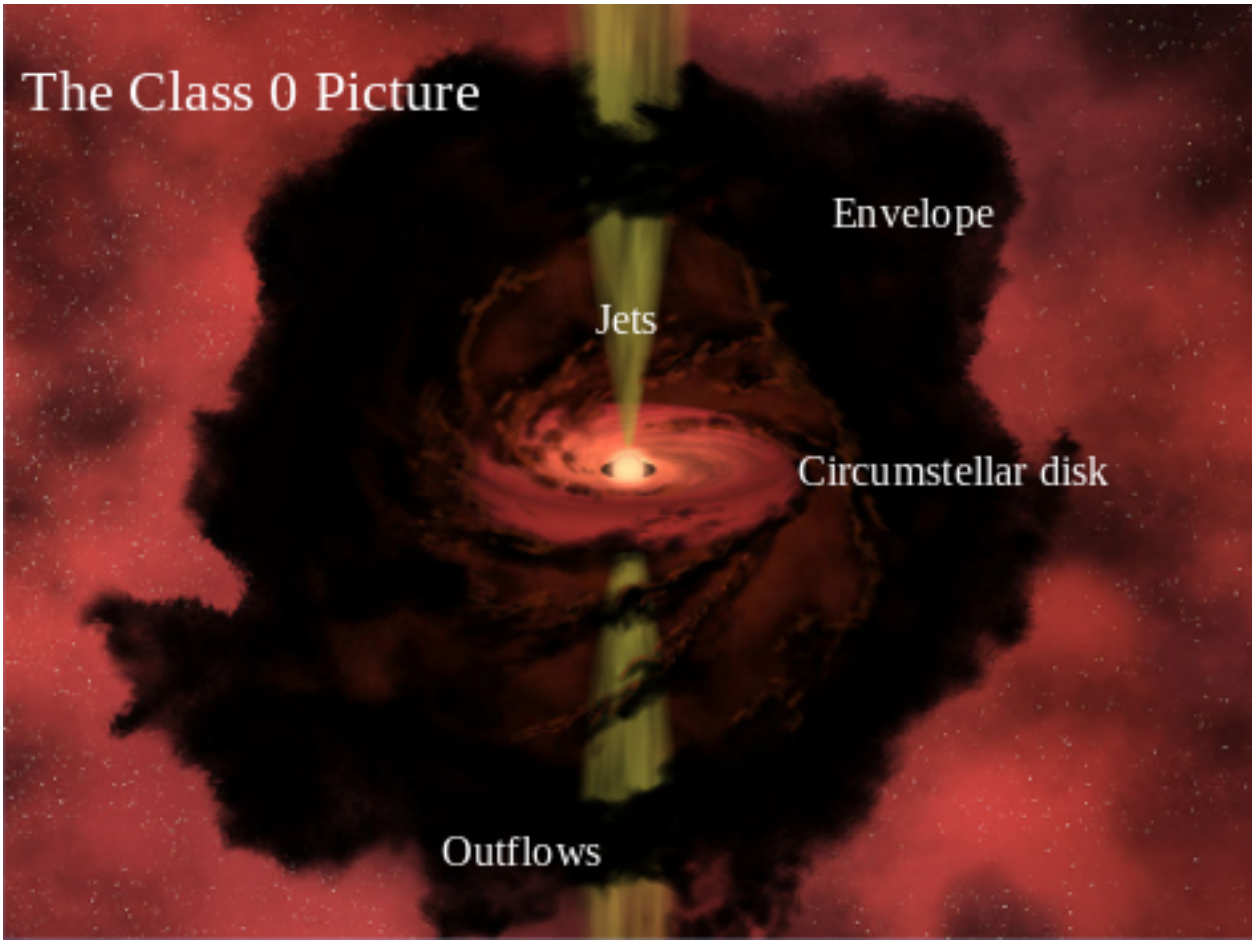

Figure 1.3: Artist's conception of a Class 0 protostar. Different components of the system are labeled in white. Credit (modified): NASA/JPL-Caltech/R. Hurt (SSC)

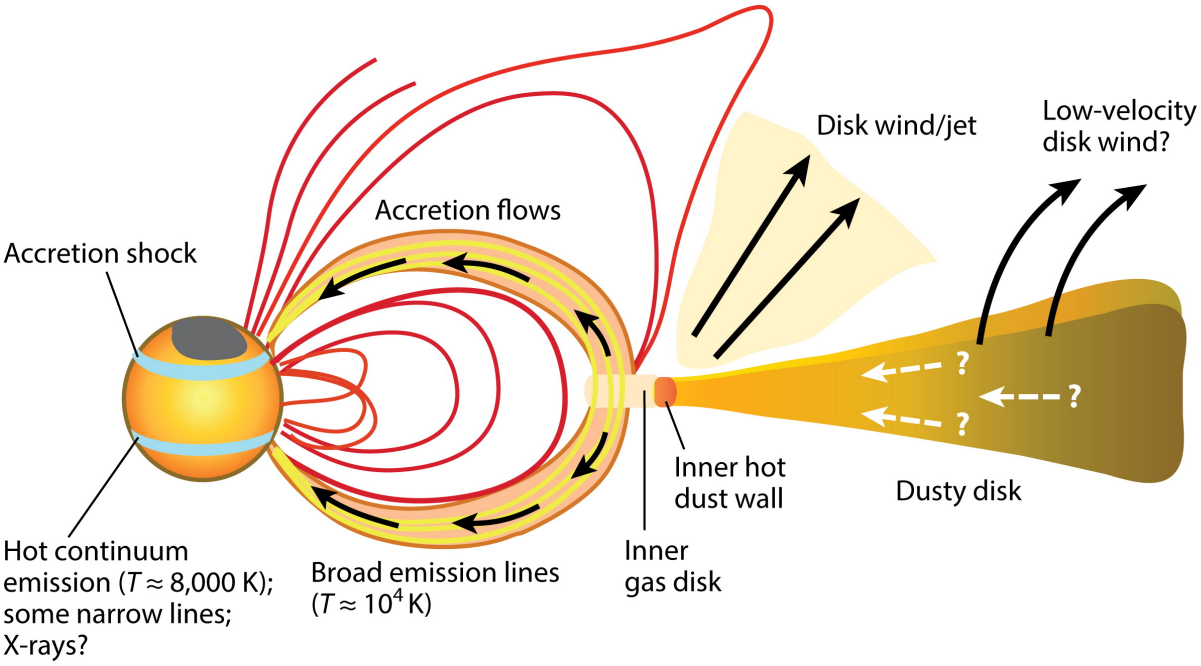

Hartmann L, et al. 2016.
Annu. Rev. Astron. Astrophys. 54:135–80

Figure 1.4: Schematic view of a young star accreting from a disk through a stellar magnetosphere from Hartmann et al. 2016.

pairs and groups of stars being the norm rather than the exception.

Multiple systems (which consist of two or more stars gravitationally bound) are of significant interest to stellar astrophysicists. Their evolution can be extremely dynamic, with their relative orbits changing with time. This progression can have strong implications for the intrinsic properties of the individual stars within the larger system. We show an example of a (simulated) triple system in Figure 1.5.

Many aspects of how triple and higher order (e.g., quadruple, quintuple) systems evolve are not well-understood. However, as the number of observed triple systems increased, a pattern became apparent. Triple systems often consisted of two stars closely orbiting each other with a much more distant third companion. This finding was formalized by Tokovinin et al. 2006, finding strong statistical evidence for a direct connection between the inner binary and tertiary companion. In particular, tighter binaries (e.g. those with the smallest separations) were systematically more likely to have a tertiary companion than wide binaries.

The implication from this work argues that triple systems evolve in such a way to achieve this preferred configuration. Despite being frequently cited, this canonical result has not been reproduced since. Paper II of this dissertation seeks to similarly find evidence of this trend with a unique sample of known binaries with varying separations.

1.2 Dissertation Outline

In order to better understand the open questions regarding young stellar evolution outlined above, this dissertation focuses on using near-infrared observations from both the Keck I and Kitt Peak Observatories. In Chapter 2, we analyze our spectroscopic observations conducted for a small sample of Class 0s, which give insight into their rarely probed near-stellar environments. Notably, we find evidence for the presence of established magnetospheres, with clear signatures of active disk accretion in these objects. In Chapter 3, we analyze our high-contrast adaptive optics imaging data in search of additional companions around a large sample of known spectroscopic binaries. Our results independently reproduce the canonical result found in Tokovinin et al. 2006,

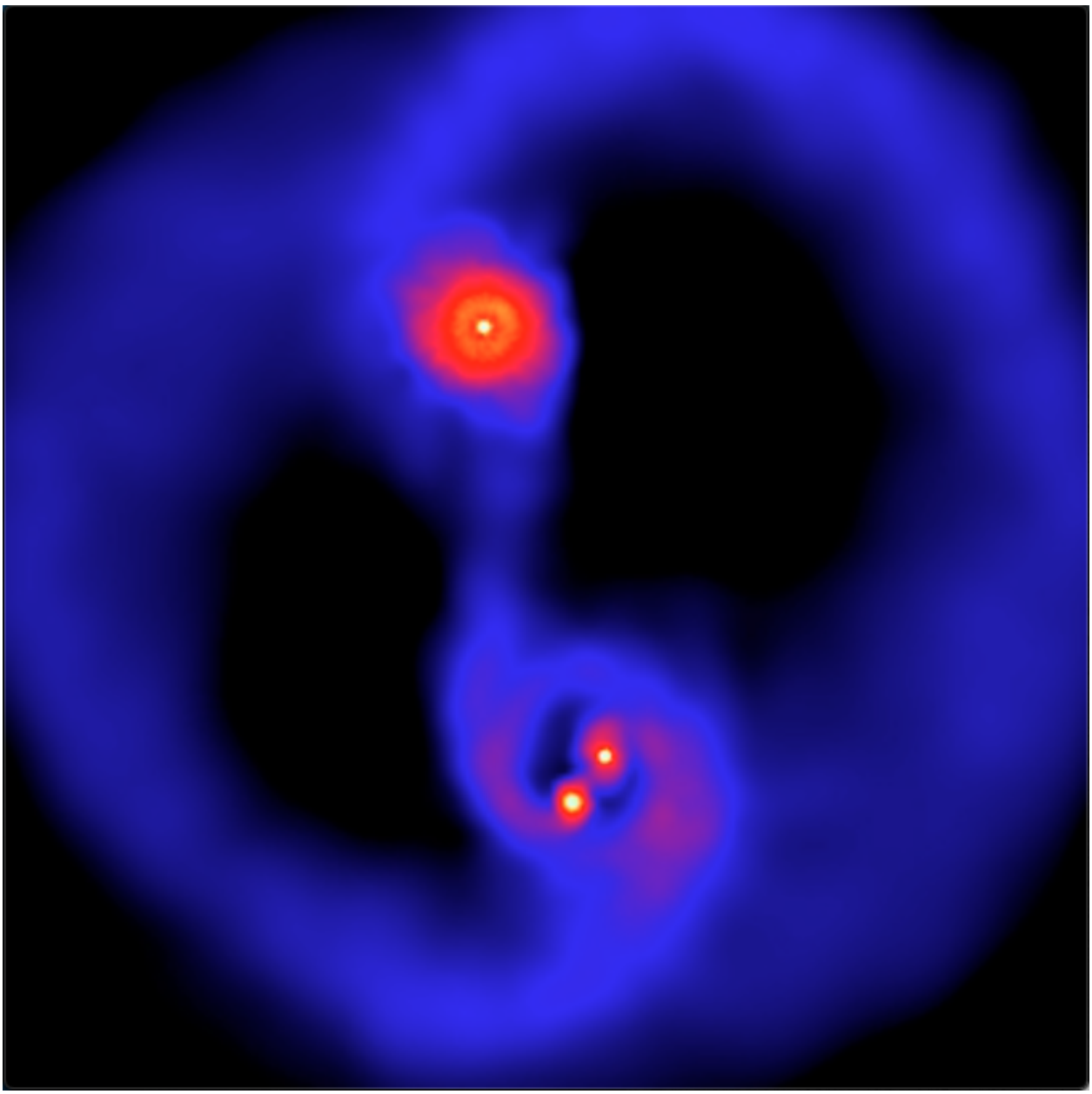

Figure 1.5: Simulated young triple system. Note the tight inner binary (lower) with a more distant third companion (upper). Credit: Matthew Bate from the University of Exeter

with evidence of tighter binaries systematically having higher rates of tertiary companions relative to that of wide binaries. In Chapter 4, we discuss future work. This includes arguing for the need of additional observations in the context of both Chapter 2 and Chapter 3 of this dissertation (Sections 4.2.1-4.2.2). We also elaborate on additional on-going projects that aim to better understand other phenomenon related to young stellar evolution (Sections 4.2.3-4.2.4).

Chapter 2

The Near Stellar Environment of Class 0 Protostars: A First Look with Near-infrared Spectroscopy

The following work was submitted to The Astrophysical Journal (Laos et al., 2021, in prep.) and is reprinted below in its entirety.

Stefan Laos[1], Thomas P. Greene[2], Joan R. Najita[3], Keivan G. Stassun[1,4]

[1]Department of Astrophysics, Vanderbilt University, Nashville, TN 37235, USA

[2]NASA Ames Research Center Space Science and Astrobiology Divison M.S. 245-6 Moffett Field, CA 94035, USA

[3]National Optical Astronomy Observatory, 950 N. Cherry Avenue, Tucson, AZ 85719, USA

[4]Department of Physics, Fisk University, Nashville, TN 37208, USA

2.1 Original Abstract

We present near-infrared K-band spectra for a sample of 7 Class 0 protostars in the Perseus and Orion star-forming regions. We detect Br γ, CO overtone, and H_2 emission, features that probe the near circumstellar environment of the protostar and reveal evidence of magnetospheric accretion, a hot inner disk atmosphere, and outflows, respectively. Comparing the properties of these features with those of Class I sources from the literature, we find that their Br γ and CO emission are generally consistent in strength and velocity width. The Br γ line profiles are broad and centrally peaked, with FWHMs of $\sim$200 km s^{-1} and wings extending to $\sim$300 km s^{-1}. The line ratios of our H_2 emission features, which are spatially extended for some sources, are consistent with shock excitation and indicate the presence of strong jets or a disk wind. Within our small sample, the frequency of CO band emission ($\sim$67%) is high relative to that of Class I samples ($\sim$15%), indicating that Class 0s have high inner disk accretion rates, similar to those of the most actively accreting Class I sources. Collectively, our results suggest that Class 0 sources have similar accretion mechanisms to the more evolved classes, with strong organized stellar magnetic fields established at the earliest observable stage of evolution.

2.2 Introduction

Numerous strides have been made over the past decades to understand the mass accretion of young stellar objects (YSOs), both from an observational and modeling perspective. By the ages of $\sim$1–10 Myr, YSOs fall into the class of T Tauri stars (TTSs, Class II/III). Their dissipated envelopes have allowed for significant observation in both the near-infrared (NIR) and visible. Overall, these phases mark the end of the mass accretion phase, with only the most active Class IIs exhibiting ongoing accretion.

At the age of $\sim$0.5 Myr, the earlier stage of Class I protostars are believed to be actively accreting, in the process of building toward their final stellar mass from the reservoir of material in their surrounding envelopes (Dunham et al. 2014). Observations in the millimeter regime have detected these massive envelopes along with established circumstellar disks (Jørgensen et al. 2009). Additionally, near-infrared observations have given us insight into the embedded central stars, in some cases detecting photospheric absorption features and emission features (Doppmann et al. 2005, Connelley & Greene 2010) that confirm active accretion.

In the past decades, the advent of sensitive, all-sky mid-infrared observatories (*IRAS*, *Spitzer*, *Herschel*) has revealed hundreds of systems younger than Class Is, designated as Class 0 protostars, in nearby dark clouds. Mounting evidence has found these Class 0s share characteristics similar to the more evolved classes at large scales. Class 0s also exhibit massive surrounding envelopes and energetic, high-velocity outflows (Andre et al. 1993), likely powered by strong mass accretion. Recent millimeter observations have begun to reveal the presence of small (on average $\sim$40 AU) circumstellar disks around a fraction of Class 0 objects (Tobin et al. 2013, Segura-Cox et al. 2018, Maury et al. 2019, Tobin et al. 2020).

These Class 0 protostars are also thought to be actively accreting, with the majority of their final stellar mass still in the surrounding envelope. Statistical analyses of large YSO samples support a relatively short duration for the Class 0 phase, with lifetimes of $\sim$0.1–0.2 Myr (Dunham et al. 2015). This brief evolutionary stage likely corresponds to the highest level of overall stellar mass accretion in these objects. Growing evidence finds this accretion is episodic to a degree,

with outflow clump structure (Arce & Goodman 2001) and CO_2 ice features (Dunham et al. 2014) documenting outburst history as frequent and variable.

Historically, however, high visual extinctions ($A_V \geq 70$) have made detailed study of the Class 0 central stars difficult. High sensitivity observations are required to analyze the, often scattered, near-IR light that leaks through less dense parts of the envelope and the outflow cavities. As a result, little is known about the underlying mechanisms governing young stellar mass accretion and the extent to which they differ between the evolutionary classes. In particular, it is still unclear how nascent protostars manage their angular momentum budget during their formation.

As they accrete increasingly high angular momentum material from their molecular envelopes, protostars can eventually be sped up to breakup rotational velocities in the absence of an efficient angular momentum loss mechanism. For molecular core angular rotation rates of a few times 10^{-14} s^{-1}, breakup velocities are reached at a small fraction of a solar mass $\sim 0.2 M_\odot$(Durisen et al. 1989, Tobin et al. 2012), a mass regime that likely corresponds to the Class 0 or early Class I phase.

One proposed mechanism to accrete past this expected mass limit is by launching a powerful stellar wind that removes angular momentum and drives molecular outflows (Shu et al. 1988). This "X-wind" picture was later generalized to account for the stellar accretion and wind generation of T Tauri stars, which have stellar rotational speeds much lower than breakup (Shu et al. 1994). In this case, mass accreting from the inner disk is channeled through a stellar magnetosphere onto the star (Hartmann et al. 1994), while angular momentum is fed back to the disk and out into a strong stellar wind that eventually collimates into a jet (Shu et al. 1995).

Overall, this generalized picture is successful in accounting for many observed properties of T Tauri stars. Study of the younger Class Is finds they similarly exhibit signs of magnetospheric accretion (Doppmann et al. 2005), with evidence for kilo-gauss strength magnetic fields (Johns-Krull et al. 2009). This mounting evidence suggests that Class Is can also be magnetically coupled to their accretion disks, although likely at smaller radii than Class II sources (Greene & Lada 2002) given the observed higher rotation rates for Class Is than Class IIs in the same region (Covey et al.

2005). It is yet to be seen, however, whether organized stellar magnetic fields can arise in the earlier Class 0 phase, and subsequently whether they accrete directly from their disks (e.g., via a boundary layer) or via a stellar magnetosphere.

We investigate these open questions with new near-IR spectroscopic observations, which probe the near stellar environment of our Class 0s. This wavelength regime offers three primary spectral features to diagnose potential accretion activity. Br γ emission has been associated with accretion and a signature for magnetospheric activity in Class Is and IIs (Najita et al. 1996b, Muzerolle et al. 1998). CO overtone emission is another strong indicator of active accretion, implying warm ($\geq$2000K) temperatures and high ($>10^{10}$cm^{-3}) local densities (Geballe & Persson 1987, Carr 1989). High resolution spectroscopy of these features have strongly argued in favor of a Keplerian, rotating disk as the emitting source (Carr et al. 1993, Najita et al. 1996a). Finally, H_2 emission is often interpreted as a signal for strong, bipolar jets or a wind and can offer insight into Class 0 outflow activity.

In this paper, we analyze our observed near-IR spectra of Class 0 protostars using multiple line diagnostics and investigate potential differences to the published results of more evolved Class I and II sources. In Section 2.3, we describe the target selection criteria used to establish our final Class 0 sample. We also report the source and nature of our data along with our data reduction and processing procedures. In Section 2.4, we report the results from the multiple line diagnostics of our near-IR spectra and compare our derived values to that of the literature for Class I and II sources. In Section 2.5, we interpret our results in the context of emission line excitation mechanisms and the circumstellar environments of Class 0 sources. Finally, in Section 2.6, we conclude with a brief summary of our findings.

Table 2.1: Journal of Observations

Object	Region	near-IR R.A. (J2000) (hh mm ss.s)	near-IR Dec. (J2000) (°' ")	UT Date	Int. Time (minutes)	Spatial Extent[a] (")	$v^{a}_{systemic}$ (km/s)
Per-emb 26	Per	03 25 38.8	30 44 06.2	2019 Oct 14	24	3.4	5.4
Per-emb 25	Per	03 26 37.4	30 15 28.4	2019 Oct 12	32	0.9	5.8
				2019 Oct 13	34	1	
Per-emb 21	Per	03 29 10.7	31 18 20.6	2019 Oct 14	16		
Per-emb 28	Per	03 43 51.0	32 03 08.1	2019 Oct 14	14	2.7	8.6
Per-emb 8	Per	03 44 44.0	32 01 36.2	2019 Oct 13	26	0.9	11
				2019 Oct 14	20	0.9	
HOPS 32	Ori	05 34 35.4	-05 39 59.0	2019 Oct 12	20	0.7	10
HOPS 44	Ori	05 35 10.6	-05 35 06.3	2019 Oct 13	12		

The full table is available in the electronic version of the Journal. A portion is shown here for guidance regarding its form and content.

[a] These extents serve as our extractions widths, corresponding to the spatial width of the individual protostellar continnua observed in our 2d spectral images. The low SNRs of our Per-emb 21 and HOPS 44 observations precluded the measurement of their spatial extents.

[b] System velocities used to shift our continuum-detected Class 0 spectra (Figure 2.1) into their corresponding systemic rest frames (Section 2.4.2). For our Perseus sources, we use the derived velocities from the $C^{18}O$(2-1) line fitting in Stephens et al. 2019. For HOPS 32, we average similarly derived velocity values for other HOPS protostars in Nagy et al. 2020 as a rough proxy.

2.3 Sample and Observations

2.3.1 Target Selection

In our efforts to investigate the accretion and jet processes of Class 0 protostars, we compile a sample of the most promising candidates for observation from Earth's Northern Hemisphere. In particular, we adopt criteria to ensure we have bona fide protostars that likely have yet to accrete the majority of their masses and are bright enough in the near-IR to allow for spectrscopic study. We consider both the Perseus and Orion star-forming regions to probe low and high mass regions, respectively.

Protostellar classes are defined observationally by bolometric temperature (T_{bol}), or the temperature of a blackbody having the same mean frequency as the observed continuum spectrum. To this end, we began with the lists of suspected Class 0 ($T_{bol} < 70$ K) protostars in Perseus (c2d *Spitzer* legacy project, Evans et al. 2009) and Orion (*Herschel* Orion Protostar Survey, Furlan et al. 2016). We required significant *Spitzer* IRAC (Fazio et al., 2004) 3.6–5.8μm fluxes (≥ 1 mJy) and inspected mm-interferometer observations (Jørgensen et al. 2009, Maury et al. 2010) when available to verify the existence of massive, extended circumstellar envelopes. For the remaining sources, images from the UKIRT Infrared Deep Sky Survey (UKIDSS, Lawrence et al. 2007) were used to measure positions, integrate K-band fluxes, and estimate source FWHM sizes to assess their observation potential. Ideal candidates had compact spatial extent (FWHM $\leq 2''$) and were bright enough (K $\sim$ 15–16) to maximize the expected S/N of their observation.

From this sample, we observed seven unique targets (5 in Perseus and 2 in Orion). The object positions, UT dates, and total integration times of our observations are given in Table 2.1.

2.3.2 Observations and Data Reduction

We obtained moderate resolution and moderate S/N near-IR *K*-band spectra of our Class 0 protostars on 2019 Oct 12, 13, and 14 UT with mostly clear skies and $0.6''$ – $0.7''$ seeing. All observations were made with the Keck I telescope on Maunakea Hawaii, using the MOSFIRE

facility spectrograph (McLean et al. 2010, 2012) in its long-slit mode.

Spectra were acquired with a 1.″5 (8-pixel) wide slit. We measured a spectroscopic resolving power of $R \equiv \lambda/\delta\lambda$ = 2,400 (120 km s^{-1}) for seeing-limited point sources at a wavelength of 2.24 microns. Some of our objects, however, are fairly extended (their observed spatial extents are listed in Table 2.1), likely reducing our spectroscopic resolving power to R$\sim$1700 in these cases. The plate scale was 0.1798"/pix along the 46″ slit length. The order-sorting MOSFIRE K filter was used to record the λ = 2–2.4 μm wavelength range in each exposure.

Data were acquired in AB pairs of 120 s long exposures, with the telescope nodded 10″ along the slit between integrations. The A0 dwarfs HIP 17971 and HIP 27089 were observed to correct the telluric features in the protostar spectra.

All data were reduced using Pypeit (Prochaska et al., 2020), an open-source Python based data reduction pipeline supporting multiple optical and near-IR spectrographs. In Pypeit, a dome flat exposure is first used to auto-identify and trace the slit edges. Spectra are wavelength calibrated with low-order fits to the OH sky lines present in the science frames. Overall, lower RMS fits were achieved using these lines when compared to fits using the arc spectra of our observed Ne and Ar lamp exposures. Both object and standard images are processed by a cosmic ray masking routine, flat fielded and sky subtracted. Constant extraction widths as a function of wavelength (reported in Table 2.1) are computed from the flux profile of the individual continuua, which do not consider further extended emission. Extracted individual spectra for each pair are then co-added. To remove instrumental and atmospheric features, the co-added object spectra were then divided by the corresponding (co-added) spectra of the A0 dwarf observed at similar airmass. When appropriate, we shifted our protostar spectra slightly in wavelength relative to their telluric spectra to minimize telluric artifacts. We multiplied this result by the (R = 10000 intrinsically, binned to the dispersion of our data) PHOENIX (Husser et al., 2013) spectrum of the dwarf stellar model that most closely matched its corresponding standard to achieve our telluric-corrected spectra. Lastly, we flux calibrated our spectra by scaling to the K-band fluxes of the corresponding telluric star.

2.4 Results

We show our near-infrared spectra in Figure 2.1. From our sample of seven unique targets, we exclude the spectrum of HOPS 44 from the analysis in the following sections, because of its low signal-to-noise. Its reduced spectrum is shown in Appendix Section 2.8. We also do not detect the continuum of Per-emb 21 and only analyze here its observed H_2 emission lines.

Overall, the three main groups of spectral features seen across our near-IR spectra include CO band, HI Brackett (Br) γ, and H_2 emission, with varying intensity. We do not detect any photospheric absorption features for our sample. In Table 2.2, we report measured equivalent widths (EW) for the emission features seen in our sample. All derived strength values presented in Table 2.2 correspond to emission spatially coincident with each object's continuum source. Subsequently, these strength values do not account for emission extended spatially past the extracted continuum extents listed in Table 2.1. For undetected lines, we report 3σ upper limits. In addition to EWs, we compute numerous line diagnostics and compare our values to that of the more evolved Class Is in the following sections.

2.4.1 CO Overtone Emission

We detect emission bands near 2.3 μm in four of our Class 0 objects (Per-emb 25, Per-emb 26, Per-emb 28, and HOPS 32). Their structure is consistent with CO overtone emission. For a direct comparison, we normalize the bands by fitting the shape of the continuum blueward of the first bandhead, with either a linear fit or a low order quadratic, and dividing them by this estimate.

To show that these observed features are consistent with spectrally resolved CO emission, we construct a simple emission model using the family of higher-resolution (R=10000) synthetic spectra in the PHOENIX (Husser et al., 2013) library. The spectra of cool M star giants exhibit broad CO absorption features in a low gravity environment similar to a disk atmosphere. With our starting PHOENIX spectra (T_{eff} = 3500 K, $\log g$ = 1.5, [Fe/H] = 0), we apply the following steps to compare to our data.

The synthetic spectrum is first binned down to match the lower spectral resolution of our data. To invert its CO absorption features into emission, we multiply this spectrum by -1 and then fit its continuum as described for our science objects. We divide the corresponding spectrum by this fit and then add back 2 stellar continnua (setting the baseline to +1). We also allow for an extra scaling factor, equivalent to the potential contribution of veiling, to improve our matches to the individual band amplitudes.

The inverted synthetic spectra are then broadened with a Gaussian filter to match the broader width of each protostar. We manually iterate the width of our Gaussian filter and repeat this process with different PHOENIX model temperatures to achieve the best fit to our data visually (final widths and temperatures shown in Figure 2.2).

The reasonable match between the continuum-normalized CO bands in our Class 0s and their corresponding model spectra (Figure 2.2) demonstrate that spectrally broadened CO emission is detected. For our observed v=2-0 CO bands, we estimate their velocity width by converting our derived sigma of the Gaussian filter to full width half maxes (FWHMs). We report FWHMs ranging from 200 to 350 km s^{-1} (Table 2.3). From our iterative process, we estimate reasonable visual fits allow for a range of $\pm$0.5 sigma units around the best fit sigma value, corresponding to an overall FWHM uncertainty of $\sim$50 km s^{-1} (except in the case of Per-emb 26, which is much less constrained due to the much lower S/N observation).

We find our observed profiles (black, Figure 2.2) are consistent with those observed in more evolved Class Is and energetic Class IIs (Carr et al. 1993, Najita et al. 1996a, Contreras Peña et al. 2017). In these older sources, the emission is well explained as arising from the heated atmosphere of the inner disk (Calvet et al. 1991). Our measured FWHMs are also similar to other previously observed Class I and IIs (Chandler et al. 1993), which have appeared broadened past 100 km s^{-1}. Given the moderate spectral resolution of our data, however, we are unable to constrain other disk properties ($i_{\rm disk}$, $v \sin i$) through a detailed model analysis beyond this estimate.

2.4.2 Brackett γ Equivalent Widths and Line Profiles

We detect Br γ emission in four of our Class 0 objects (Per-emb 8, Per-emb 25, Per-emb 28, and HOPS 32). We begin by comparing our measured Br γ EWs to that of known Class Is. Figure 2.3 plots the measured EWs of the Br γ line and the CO band at 2.293 μm for our sources and the Class Is observed in Connelley & Greene 2010. Overall, we find the broad distribution of the observed Br γ and CO v=2-0 band EWs from these Class Is overlaps with that of our Class 0s. This result implies their near-stellar environments, with accretion and the inner disk sensitively traced by our detected Br γ and CO, appear to be similar between Class 0 and Is.

To examine our observed Br γ line profiles, we first shift them into their systemic rest frame. For our Perseus sources, we use the derived velocities from the $C^{18}O$(2-1) line fitting in Stephens et al. 2019, which primarily traces the envelopes surrounding our protostars. Although this analysis has not been conducted for HOPS 32, we refer to the similarly derived velocity values for other HOPS protostars in Nagy et al. 2020 and use their average as a rough proxy. Collectively, these shifts are small in magnitude (on the order of $\sim$10 km s^{-1}). For a proper comparison, we then normalize our profiles by deriving a linear fit to the continuum redward and blueward of the Br γ emission and dividing the spectrum by this estimate. Using the splot routine in IRAF, we fit each Br γ feature with a Gaussian profile to estimate its width. We report the FWHM of the best fit Gaussian in Table 2.3. All reported FWHMs in Table 2.3 have had our instrumental velocity resolution of 120 km s^{-1} subtracted out in quadrature. We compare these resultant profiles with that of observed Class Is (Doppmann et al., 2005) in Figure 2.4. Overall, we find the Class 0 line shapes to be very similar to that of the Class Is and Class IIs, exhibiting a centrally peaked core (FWHM$\sim$200 km s^{-1}) with broad wings extending to $\pm$300 km s^{-1}. These widths are similar to that found for both T Tauri (Folha & Emerson 2001, Najita et al. 1996b) and Class I (Doppmann et al., 2005) sources, roughly 100–300 km s^{-1}. We discuss the interpretation of our observed profile structure in Section 2.5.1.

2.4.3 H_2 Equivalent Widths and Emission Line Ratios

We detect H_2 emission lines in six of our Class 0 objects (Per-emb 8, Per-emb 21, Per-emb 25, Per-emb 26, Per-emb 28, and HOPS 32). Among the numerous H_2 lines observed, we find the 2.1218 μm H_2 v=1-0 S(1) emission line is strongest across our sample. Similar to our comparison in Section 2.4.2, we plot the measured EWs of the Br γ and H_2 v=1-0 S(1) line between our Class 0s and the Class Is from Connelley & Greene 2010 in Figure 2.5. Three of our Class 0s (HOPS 32, Per-emb 8, and Per-emb 26) show significantly larger H_2 EWs than any of the Class Is from Connelley & Greene 2010. To quantify the magnitude of this difference, we compute the mean H_2 EW between both samples and find they differ by more than the combined standard deviation within each group. We also perform a two-dimensional two-sided KS test between the two samples and find the difference to be statistically significant, reporting a p-value of 0.007.

We note the spectra of our Class 0s do not show any evidence of photospheric absorption features (Figure 2.1), likely reflective of high veiling in these objects. Comparably, only $\sim$60% of the Class Is that exhibit both H_2 and Br γ in emission were found to be highly veiled. The observed Class Is with low veiling do not appear to exhibit significantly higher H_2 EWs. Given this, we may be seeing evidence of higher Class 0 H_2 flux relative to their photospheric continua in our three outlying Class 0s relative to these observed Class Is.

Similar to our Br γ analysis, we fit a Gaussian profile to our observed H_2 v=1-0 S(1) emission lines in IRAF and report their FWHMs in Table 2.3 after subtracting out our instrumental resolution (120 km s^{-1}) in quadrature. The FWHMs of this unresolved line, however, are also subject to the variable spatial extents of our objects (Table 2.1) and are broadly overestimated. We note our derived values likely probe different parts of the corresponding H_2 flows depending on the orientation of our objects. We also report the velocity shift of the emission centroid relative to the rest wavelength of the line (2.1218 μm), typically finding velocities of $\geq |50|$ km s^{-1}. Overall, the shifted, broad widths of our observed H_2 emission lines are consistent with collisional excitation in jets or a wind.

The ratios of particular H_2 emission lines have the ability to constrain the source excitation

mechanism responsible for this observed circumstellar emission. Gredel & Dalgarno (1995) find the H_2 v = 1–0 S(1) (2.1218 μm) to v = 2–1 S(1) line (2.2477 μm) ratio is relatively sensitive for differentiating between different excitation mechanisms and calculate predictions for UV excitation, shock-heated gas in the form of a wind, and X-ray excitation of low ionization H_2. To de-redden our line ratio, we derive rough estimates of the foreground extinction by fitting the spectral energy distributions (SEDs) of our Class 0 protostars. Our methodology is detailed in Appendix Section 2.7. We note this correction is generally minimal, given the small difference in wavelength between these individual H_2 lines.

We report the reddening-corrected line ratios for our Class 0 sample in Table 2.3. Similar to the majority of the Class Is studied in Greene et al. (2010), we find the values of our Class 0s are most consistent with collisional excitation via shocked gas in a wind or X-ray excitation but not UV excitation (Figure 2.6). The more moderate S/N in the fainter H_2 line transitions precludes our ability to compare this result with other line ratios.

2.4.4 H_2 Extended Emission

We find HOPS 32, Per-emb 26, and Per-emb 8 (the strongest H_2 EW sources, Figure 2.5) also exhibit H_2 emission extended from the continuum; an example is shown in Figure 2.7. Our observations of Per-emb 21, while not sensitive enough to detect the continuum, similarly detect variably extended H_2 emission. Per-emb 25 and Per-emb 28 do not show evidence of any off-axis emission. From our 2d images, we report the measured angular extent of the H_2 1-0 S(1) line in Table 2.3. In all cases, we find the emission is far extended spatially ($\geq 5''$, i.e., $\sim$1250 AU across for our Perseus sources, and $8''$, i.e., $\sim$3200 AU for HOPS 32).

We reference the literature for known outflows corresponding to our Class 0 sources in an attempt to find other potential tracers of our extended emission. Numerous Perseus protostars have had their outflow features identified via both sensitive molecular line emission tracing (Lee et al. 2016, Stephens et al. 2017, Tobin et al. 2018) and H_2 2.122-μm imaging surveys (Davis et al., 2008). In Table 2.4, we compare published outflow position angles (PAs) with the slit PAs from

our observations when possible.

We find that, as expected, extended emission is present when the slit PA is aligned with the PA of a known CO outflow. As an example, Per-emb 8 was observed in Tobin et al. (2018), which found evidence for strong, rotational CO 2-1 emission northwest of the system at a PA of 313° lacking a southeast component. We find this asymmetry reflected in our data given the close alignment with our slit PA, showing the extended H_2 emission spatially offaxis from the continuum in only one direction (Figure 2.7). Alternatively, the observed H_2 outflow feature identified for Per-emb 25 (Davis et al., 2008) has a PA close to orthogonal with our slit PA. In this case, its lack of extended H_2 emission is not surprising.

2.4.5 Line Luminosities

To compute individual line luminosities, we deredden our measured line fluxes using our derived extinction values (Appendix Section 2.7). We note these values are estimates with high uncertainty given the complicated physical nature of our Class 0s (e.g., non-symmetrical envelopes, scattered light). Subsequently, it is difficult to draw robust conclusions from our derived line luminosities. Despite these limitations, we tentatively compare these values with that observed in more evolved systems as a first look between Class 0s and Is.

In Figure 2.8, we compare our derived H_2 v=1-0 S(1) line luminosity with that of the Class Is from Connelley & Greene 2010. We find our Class 0s appear to exhibit a wider range of H_2 v=1-0 S(1) line luminosities than Class Is, with a roughly similar median value between both samples.

We also compare our Br γ luminosities with that of observed YSOs, referencing low mass Class I and IIs from the literature. In Figure 2.9, we show their respective luminosity distributions. Although it is perhaps surprising that our Class 0s have median Br γ luminosities $\sim$100 times smaller than those of Class Is, the discrepancy could be resolved if we have systematically underestimated the extinctions of Class 0 systems by a factor of 2. Overall, it remains unclear the extent to which the line luminosities of these two populations differ until more precise Class 0 extinction estimates can be derived. We note our high extinction uncertainties also preclude our

ability to derive robust mass accretion rate estimates from our Br γ luminosities, as has been done for Class Is and IIs (Muzerolle et al. 1998, Fiorellino et al. 2021).

2.5 Discussion

The line diagnostics analyzed in Section 2.4 probe the near-circumstellar environment of our Class 0 sample and lend insight into the accretion and outflow processes underway in these YSOs. Here, we compare our measured Class 0 properties with those of well-studied Class I and II sources to investigate the nature of the near-circumstellar environment at the earliest observable stage of evolution.

2.5.1 Class 0 Stellar Magnetospheres

In Section 2.4.2, we find our Class 0 sample has broad, centrally peaked (Figure 2.4) Br γ line profiles (FWHM $\sim$ 200 km s^{-1}) with wings extending to high velocity (300 km s^{-1}). Similar profiles are observed in many Class II (Najita et al. 1996b, Folha & Emerson 2001) and Class I (Doppmann et al. 2005, Connelley & Greene 2010) sources. In these more evolved sources, the Br γ profiles are often considered strong evidence for magnetospheric accretion, in which the inner region of the hot circumstellar disk is channeled by stellar magnetic field lines onto the surface of the star at high infall velocities.

Models of emission from magnetospheric accretion in the Balmer lines (Calvet & Hartmann 1992, Romanova et al. 2012) and Br γ (Muzerolle et al. 1998) have had success reproducing these observed profile shapes. This interpretation is supported by measurements of strong (approaching 3 kG) stellar magnetic fields in Class II (Johns-Krull 2007) and Class I (Johns-Krull et al. 2009) sources.

While Class 0 magnetic field strengths have yet to be estimated directly, the similarity between our Class 0 Br γ profiles and those of these more evolved sources argues in favor of a shared accretion mechanism. These results provide evidence of protostellar magnetic fields and magnetospheres being established very early in the star formation process, at the earliest times yet probed.

2.5.2 Comparison of Class 0 and Class I/II Accretion Activity

Although our Class 0 sample is small, we note the high frequency of our detected spectral features in emission. There have been few other Class 0s that have had their near-IR spectroscopic observations analyzed for both emission and absorption components. Serpens S68N also exhibited H_2 emission but was absent in Br γ and showed CO bands in absorption rather than emission (Greene et al. 2018). We report the incidence rates of these features in emission among our 5 continuum-detected Class 0s (Figure 2.1) and Serpens S68N in Table 2.5. We compare these rates with those of Class Is in nearby molecular clouds (Doppmann et al. 2005). These Class I statistics are similar to what has also been observed in a larger, all-sky sample of Class I protostars (Connelley & Greene 2010).

We find similarly high rates of Br γ emission between the Class 0 and Class I samples, consistent with the active mass assembly expected at these young ages. For both CO and H_2, however, we find notably higher emission incidence rates for Class 0s relative to Class Is.

The high prevalence of CO emission among our Class 0s suggests differences in the inner accretion disks of these objects relative to that of Class Is. Our observations find that the atmospheres of Class 0 inner disks frequently achieve the warm ($\geq$2000 K), dense environments ($>10^{10}$ cm^{-3}) required for CO emission, strongly suggestive of a higher average disk accretion rate for Class 0s than Class Is. We perform a Fischer's exact test and find this result is statistically significant, with a nominal p-value of 0.01. A high accretion rate for Class 0 sources is consistent with the low incidence rate of photospheric absorption features among Class 0s relative to Class Is. Currently, absorption features (Na I and Ca I, 2.21 and 2.26 μm respectively) have only been observed in Serpens S68N, where it is detected weakly. The low incidence rate is likely a consequence of higher veiling in Class 0s produced by strong continuum emission from their inner warm disks.

The high disk accretion rate implied by these results (CO emission, high veiling) is likely similar to that inferred for active Class Is (Fiorellino et al. 2021) and EXors (Aspin et al. 2010), two groups that have also shown near-IR features in emission and have estimated accretion rates of ($\sim 10^{-7}$–10^{-6} M$_\odot$ yr^{-1}). At a much high disk accretion rate, more similar to that of FU Oris

($\sim 10^{-4}$ $M_\odot$ yr^{-1}), the CO overtone bands would appear in absorption (Calvet et al. 1991) and the magnetosphere would be crushed, reducing or eliminating the Br γ emission. At much lower disk accretion that are typical of Class II T Tauri stars ($\sim 10^{-8}$ $M_\odot$ yr^{-1}), the inner disk would not be warm enough over a large enough vertical column density to produce CO overtone emission.

At a disk accretion rate of $\sim 10^{-6}$ $M_\odot$ yr^{-1}, a protostar can sustain a stellar magnetosphere (and produce the Br γ line profiles we observe) if it has developed a strong, organized stellar magnetic field. If our Class 0 sources have a protostellar mass of 0.2 $M_\odot$ (as measured for the Class 0 source L1527 IRS; Tobin et al. 2012) and a stellar surface gravity ($\log g$) of 2.38 (as measured for Serpens S68N; Greene et al. 2018), protostellar radii are $\sim$4–5 $R_\odot$. If the Class 0 sources further have a disk accretion of $\sim 10^{-6}$ $M_\odot$ yr^{-1} and their stellar magnetospheres truncate the inner disk at $\sim$2 stellar radii (as measured for the Class I YLW 15; Greene & Lada 2002), the required protostellar magnetic field strength is $\sim$1 kG (Hartmann et al. 2016 and references therein). Thus, the CO overtone emission, strong veiling, and Br γ we observe are all plausibly consistent with Class 0 inner disk accretion rates of $\sim 10^{-6}$ $M_\odot$ yr^{-1} and approximately kilogauss strength protostellar magnetic fields.

Even within our small sample, several sources depart from the simple picture described above. Unlike the majority of sources in our Class 0 sample, Per-emb 26 exhibits CO overtone emission but no Br γ emission. This object may be in an intermediate state, with a slightly higher accretion rate than the majority of our Class 0s. An accretion level of this magnitude could plausibly suppress the stellar magnetosphere, explaining the absence of Br γ, while still remaining below an FU Ori accretion level, allowing for CO emission (rather than absorption). As a variant in a different direction, the recent near-IR spectrum of Serpens S68N lacks Br γ emission and exhibited CO bands in absorption (Greene et al. 2018). Serpens S68N is likely in a state of lower disk accretion than our Class 0s, with low veiling indicated by its observed photospheric absorption features (Na I, Ca I). Its modest derived $\log g$ value (2.38) is more consistent with a low-gravity stellar photosphere than a disk. Its inflated radius implied by this derivation may be evidence of a significant, recent accretion episode, depleting the reservoir of available accreting material in its disk.

2.5.3 Nature of the H_2 Emission

We interpret the results from our multiple line diagnostics in Section 2.4 to assess the nature of the H_2 emission seen in our Class 0 sample. We find our Class 0 H_2 emission properties are often similar to that of known Class Is but in some cases enhanced, indicating higher EWs (Figure 2.5) and large spatial extensions (Figure 2.7).

In our attempt to constrain the most likely H_2 excitation, we derived 1–0 S(1)/2–1 S(1) line ratios that argue in favor of either shock-heated gas or X-ray excitation. If excited by collisions in shocks, the molecular hydrogen ortho:para ratio can also be derived with little sensitivity to the H_2 rotation temperature from the v=1-0 S(1) and v=1-0 S(0) line ratio (Kristensen et al., 2007). From their equation 5, we find ortho:para ratios ranging from 2.3–2.9 assuming a rotational temperature of 3500 K across our sample. This result provides further evidence of molecular hydrogen emission in shocks as Wilgenbus et al. (2000) finds the hydrogen atom exchanges in shocks set the high temperature limit to o/p $\leq$ 3.

We query the literature for observations of X-ray activity in our Class 0 sample, which may also suggest ongoing accretion. X-ray activity can be quantified via an object's hardness ratio [HR = (N_h - N_s)/(N_h + N_s)], where N_h and N_s are the detected counts in the hard (2–8 keV) and soft (0.5–2 keV) energy bands, respectively. Stassun et al. (2004) computed the extinction-corrected hardness ratios between a sample of non-accreting weakly-lined TTS and accreting classical TTS, finding the latter population was more likely to have high HRs.

Despite the likely high visual extinctions expected towards our Class 0s, we find Per-emb 8 has been detected by *Chandra* measurements (Wang et al. 2016). Following the analysis of Stassun et al. (2004), we correct our derived value for extinction. The corrected HR value for Per-emb 8 ($\sim$0.3) lies near the very high end of the distribution for PMS stars. We find this result, while not a definitive indicator for accretion, is consistent with our cumulative evidence that our Class 0s are likely undergoing active accretion. In particular, the strong X-ray activity observed in Per-emb 8 could be further evidence of organized magnetic fields being plausibly established by Class 0s, supported by the recent observations of Class 0 HOPS 383 (Grosso et al. 2020).

Collectively, these findings are consistent with the properties expected from strong jets or a wind. In particular, the observed high velocity, often extended, H_2 emission may be evidence of the driving force behind the molecular outflows commonly observed in Class 0s. Future observations of additional Class 0s will be required to further characterize the predominant inner H_2 emission source at this evolutionary stage.

2.6 Summary and Conclusion

We present new observations of near-infrared *K*-band spectroscopy for a sample of 7 Class 0 protostars in the Perseus and Orion molecular clouds. The H_2, Br γ, and CO v=2-0 band features we detect probe the inner circumstellar environments of these systems (Figure 2.1). The lack of observed stellar absorption features indicates high continuum veiling, likely from an inner disk with a high accretion rate.

1. Our Class 0 Br γ line profiles are broad, centrally peaked, and similar in shape to those of previously observed Class Is (Figure 2.4) and strongly suggestive of magnetospheric accretion. This result suggests that organized stellar magnetic fields are established very early, at the earliest observable stage of their evolution.

2. The high frequency of CO band emission observed in our Class 0s (4/6 $\cong$ 67%) relative to observed Class Is (8/52 $\cong$ 15%) is strongly suggestive of a higher average disk accretion rate for Class 0s. A disk accretion rate of $\sim 10^{-6}$ $M_\odot$ yr^{-1} is consistent with the spectral features we observe in our Class 0 spectra, high enough to produce the conditions for CO overtone emission while not high enough to crush the stellar magnetosphere suggested by our Br γ emission if the protostellar magnetic field is approximately kilogauss in strength.

3. Our H_2 line analysis (Section 2.4.3) derives line ratios that argue in favor of shocks as their source excitation mechanism, similar to that of observed Class Is. Along with the large H_2 spatial extensions and prevalence of H_2 emission we observe in our Class 0s, we interpret

this as evidence of strong jets or a disk wind in the near stellar environment, consistent with earlier evidence for strong outflows in these systems on larger scales.

Taken collectively, these results are beginning to characterize the accretion properties of Class 0s. In particular, we find Class 0 protostars may share more similarities with their Class I counterparts than previously thought, with evidence of inner disk accretion properties similar to actively accreting Class Is and magnetospheres being established at the earliest observable evolutionary stages. These organized magnetic fields appear to be plausibly capable of mediating the accretion process, as Class 0s build towards their final mass.

2.7 Appendix Section A: Spectral Energy Distribution Fitting

2.7.1 Motivation

Prominent star-forming regions like the Perseus and Orion complexes have been observed by multiple surveys, recording flux measurements for many young stellar objects (YSOs) over a large range of wavelengths (1–1100μm). These measurements constitute the spectral energy distribution (SED) of an object; for Class 0s, the properties of the central source, its circumstellar disk, and its massive envelope contribute to the overall shape of the SED. Fitting this shape with an SED model can constrain numerous properties including the orientation of the disk along with the foreground extinction to the object along our line of sight.

For the central object of a Class 0, this extinction can be significantly high, with A_V reaching up to 70–80 magnitudes. A proper comparison of our emission line fluxes with that of the more evolved Class I and II sources requires them to first be de-reddened. In extreme cases, this can account for a large correction to the overall luminosity of the spectral feature.

However, due to degeneracies between the star, disk, and envelope properties, the shape of the SED is often not unique, with a family of SED models able to fit the observed SED. The situation is further complicated by the axisymmetrical nature of most Class 0s, as the observed emission leaks out from holes in the envelope and scatters off the walls of the inner cavity. Given

these limitations, we take care to not over-interpret the results, solely focused on deriving a rough estimate of the foreground extinction. We also note the methods used to estimate A_V for Class Is are not as feasible for Class 0s, given the heavily embedded nature of Class 0s often lead to an absence of measurements at J and H wavelengths.

2.7.2 Procedure

When constructing our SEDs, we find our Class 0s have varied sampling at both near-IR and mid/far-IR wavelengths. In the near-infrared, we used J, H, and K_s from the Two Micron All Sky Survey (2MASS; Skrutskie et al. 2006) when available, otherwise supplementing with JHK measurements from UKIDSS (Lawrence et al., 2007) when possible. In the mid-infrared, the Infrared Array Camera (IRAC; Fazio et al. 2004) and the Multiband Imaging Photometer (MIPS; Rieke et al. 2004) on *Spitzer* provided 3.6, 4.5, 5.8, and 8.0 μm and 24 μm photometry, respectively. We consider the reported values of this *Spitzer* data from numerous sources and followup observations including Kryukova et al. 2012, Megeath et al. 2012, Rebull 2015, Dunham et al. 2015, and Getman et al. 2017.

When possible, we also use data from the Infrared Spectrograph (IRS; Houck et al. 2004) on Spitzer. HOPS 32, Per-emb 21, 25, and 28 were observed by both the Short-Low (SL; 5.2–14 μm) and Long-Low (LL; 14–38 μm) modules whereas Per-emb 26 was only observed in SL. In the far-infrared, some of our Perseus sources have recorded *Spitzer* MIPS 70 and 160 μm fluxes while HOPS 32 has recorded Herschel PACS (Poglitsch et al., 2010) data at 70, 100, and 160μm. Similarly, some of our Perseus sources also have 450, 850 μm SCUBA (Sandell & Knee 2001, Kirk et al. 2006) and 1.1 mm Bolocam (Enoch et al., 2006) measurements while HOPS 32 has 350 and 870 μm (Stutz et al., 2013) by the APEX telescope using the LABOCA and SABOCA instruments (Siringo et al. 2009, 2010, respectively).

To fit the observed SEDs, we use the YSO SED models of Robitaille et al. 2006, which consists of a pre-computed grid of 200,000 total models. Overall, our approach adopts the recommendations laid out by Robitaille et al. 2007. In cases where several measurements were available at

similar wavelengths, we only used the highest quality one (i.e. MIPS data was favored over lower-resolution IRAS measurements to avoid confusion).

At a given wavelength, many of our sources have been observed in multiple epochs. In some cases, recorded fluxes (particularly in the *Spitzer* IRAC channels but also 2MASS K-band and MIPS 24 μm) show significant variability, up to an order of magnitude for Per-emb 26. In these instances, we average the highest and lowest recorded flux measurements, inflating the error bars to capture the observed range of values. When applicable, this procedure grants the SED fitter more freedom to fit a variety of models for these sources with well-documented activity.

For IRAS, submillimeter, and Bolocam data, a lower limit of 25% was imposed on the flux uncertainties to account for uncertainties in their absolute calibration. For all other measurements without evidence of variability, flux uncertainties were increased to 10% if the recorded uncertainties were smaller.

In some cases, we find discrepancies between the flux measurements recorded at similar wavelengths but by different instruments (the overlap between IRAC channels 3 and 4 and MIPS 24 μm with our IRS spectra). This could be explained by calibration or extraction problems in the IRS spectrum (extended emission around the target or a close companion), or variability. Following the methodology in Furlan et al. 2016, we assumed the former scenario if the flux deviations between IRS and IRAC and between IRS and MIPS were similar and more than 10%, scaling the IRS spectrum to the MIPS 24 μm flux in those cases. We scale the IRS spectrum of Per-emb 25, Per-emb 28, and HOPS 32 by 0.816, 0.548, and 0.648, respectively. Similar to Furlan et al. 2016, we also bin the IRS spectrum to 3 wavelengths after smoothing over its noisy regions to ensure it does not dominate over the photometry. Incorporating the IRS spectra at these wavelengths characterizes the 10 μm silicate feature and the mid-IR slope of the SED, which crucially constrains the resultant fits. Overall, the SEDs tend to have greater coverage at shorter wavelengths, and are thus expected to reproduce the near and mid-IR fluxes better than the sub-millimeter.

Assumed apertures sizes for the various photometry are similar to those used in Robitaille et al. 2007 ($2''$ for UKIDSS, $3''$ for 2MASS, $5''$ for IRAC channels, $3.6''$ and $10.5''$for IRS in SL mode

and LL mode respectively, 10″ for MIPS 24μm, 20″ for MIPS 70μm, 30″ for MIPS 160μm, and 40″ for SCUBA and Bolocam data).

We adopt a distance search range of 200–300 parsecs (d$\sim$250 pc for the Perseus Molecular Cloud, Enoch et al. 2006) for our Perseus sources and a search range of 400–440 parsecs (d$\sim$420 pc for the Orion Molecular Cloud, Kounkel et al. 2017) for HOPS 32. We adopt an A_v extinction range of 0–100 magnitudes, assuming the extinction law of Kim et al. 1994.

2.7.3 Interpretation of Best-fit Models

In Figure 2.10, we show the final results from the SED model fitting for our Class 0s. We show the best-fit model in black and the family of models for which $\chi^2 - \chi^2_{best}$ per data point < 3 in grey.

For the majority of our sources, we find the overall family of SED models to be well constrained and small in number. In these cases, the derived extinction values have little variation, deviating by at most only a few magnitudes. In the case of Per-emb 26, however, the significant variability in the IRAC channels and MIPS 24 μm allows for a much larger number of reasonable fits along with a subsequent poor constraint on its visual extinction (ranging $\sim$30 magnitudes). Collectively, the family of models capture the depth of the 10 μm well with the available IRS data (for which only Per-emb 8 is lacking). In Table 2.3, we report our best-fit estimates for the visual extinction to each source, noting the greater uncertainty in the case of Per-emb 26.

2.8 Appendix Section B: HOPS 44 Spectrum

Due to the low signal to noise in its spectrum, we choose to exclude HOPS 44 (the faintest object in our sample, $K \sim 16.5$) from the final sample of Class 0 we analyze in Section 2.4. Interestingly, we may be seeing evidence of photospheric absoprtion features in its spectrum. We show its reduced spectrum in Figure 2.11 and encourage follow-up observations of this promising source.

Table 2.2: Emission Line Equivalent Widths

Source	1-0 S(2) EW (Å)	2-1 S(3) EW (Å)	1-0 S(1) EW (Å)	2-1 S(2) EW (Å)	3-2 S(3) EW (Å)	1-0 S(0) EW (Å)	2-1 S(1) EW (Å)	Br y EW (Å)	CO (2-0) EW (Å)	CO (3-1) EW (Å)	CO (4-2) EW (Å)
Per-emb 26	57.3 ± 1.1	29.4 ± 1.0	110.0 ± 1.0	8.3 ± 1.0	5.5 ± 1.0	52.4 ± 1.1	16.6 ± 1.1	$\leq$1.3[a]	25.5 ± 1.6	29.6 ± 1.6	27.6 ± 1.6
Per-emb 25	2.1 ± 0.2	1.9 ± 0.2	1.7 ± 0.2	0.9 ± 0.2	$\leq$0.2[a]	3.3 ± 0.2	$\leq$0.2[a]	4.5 ± 0.3	25.1 ± 0.3	20.3 ± 0.3	19.2 ± 0.3
Per-emb 28	3.9 ± 0.1	2.0 ± 0.1	6.8 ± 0.1	1.1 ± 0.1	$\leq$0.1[a]	1.4 ± 0.1	0.8 ± 0.1	2.9 ± 0.1	12.3 ± 0.1	8.6 ± 0.1	$\leq$0.1[a]
Per-emb 8	51.0 ± 0.3	9.5 ± 0.3	114.1 ± 0.3	5.7 ± 0.3	2.9 ± 0.4	35.0 ± 0.3	6.3 ± 0.4	6.9 ± 0.4	$\leq$0.5[a]	$\leq$0.5[a]	$\leq$0.5[a]
HOPS 32	55.4 ± 0.3	14.1 ± 0.3	149.8 ± 0.3	6.2 ± 0.3	3.2 ± 0.3	25.5 ± 0.3	12.5 ± 0.3	4.5 ± 0.4	25.9 ± 0.4	17.5 ± 0.4	11.0 ± 0.4

All EWs correspond to emission features. We report their absolute values in this table. These EWs do not account for emission extended from the continuum.

[a] We report a 3σ upper limit for this undetected emission line.

Table 2.3: Emission Line Derivations

Source	A_v^a	i^a	CO (2-0) FWHM^{b,c}	Br γ FWHM^b	1-0 S(1) FWHM^{b,d}	1-0 S(1) Offset	1-0 S(1)/2-1 S(1)	1-0 S(1) extent
	mag	deg	km/s	km/s	km/s	km/s		(")
Per-emb 26	29.6^e	18	352		119	68	10.5	13
Per-emb 25	9.9	32	201	307	129	58		
Per-emb 21	8.5	87			26	-46	14.9	10
Per-emb 28	2.5	81	202	244	42	75	12.2	
Per-emb 8	19.6	18		219	139	68	11.2	5
HOPS 32	24.9	87	239	237	50	-15	9.5	8

[a] Best-fit values from SED model analysis (Appendix Section 2.7). We note these derivations are rough estimates given the complicated physical nature of Class 0 SEDs and could differ significantly from the true extinctions and inclinations (Section 2.4.5).

[b] The intrinsic instrumental line width of 120 km s^{-1} has been removed in quadrature.

[c] These FWHMs are derived via the width of our Gaussian filter in our synthetic spectra comparison (Section 2.4.1).

[d] These FWHMs are subject to the variable spatial extents of our objects (Table 2.1) and are broadly overestimated. (Section 2.4.3).

[e] Poorly constrained due to significant variability in the IRAC photometry of Per-emb 26 (Appendix Section 2.7.3).

Table 2.4: Position Angle Comparison

Object	Slit PA	Outflow PA	Reference[a]
Per-emb 26	4	162, 165	1, 2
Per-emb 25, Oct 12/13	0, 0	104, 105	1, 2
Per-emb 21	320	48	3
Per-emb 28	150	112	3
Per-emb 8, Oct 13/14	313, 133	314	4

[a] Reference IDs: Stephens et al. (2017) (1), Davis et al. (2008) (2), Lee et al. (2016) (3), Tobin et al. (2018) (4)..

Table 2.5: Emission Incidence Statistics

Emission Feature	Class 0s[a]	Class 1s[b]
Br γ	4/6 $\cong$ 67%	34/52 $\cong$ 65%
H_2	6/6 = 100%	23/52 $\cong$ 44%
CO	4/6 $\cong$ 67%	8/52 $\cong$ 15%

[a] This Class 0 sample constitutes the 5 continuum-detected Class 0s from this work (Per-emb 8, Per-emb 25, Per-emb 26, Per-emb 28, and HOPS 32) and Serpens S68N (Greene et al. 2018).
[b] This Class 1 sample corresponds to the Class 1s observed in nearby dark clouds (Doppmann et al. 2005).

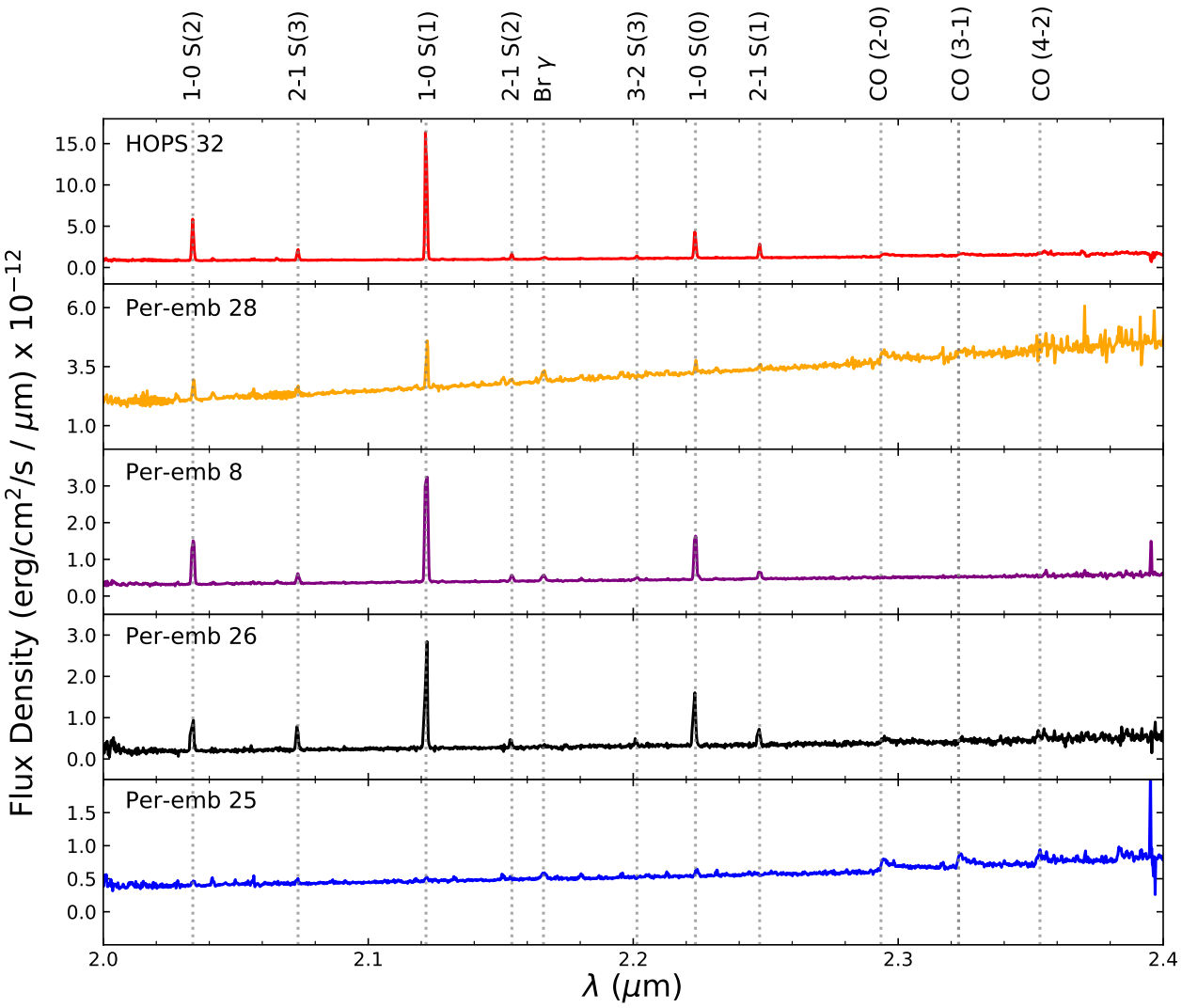

Figure 2.1: *K*–band spectra of our Class 0 protostar sample, excluding Per-emb 21 and HOPS 44 (see Section 2.4). We identify the major atomic and molecular emission features present across the spectra (numerous H_2 emission line transitions, Br γ emission, and CO band emission). We refer the reader to Table 2.2 for a complete census of line feature detection per individual source.

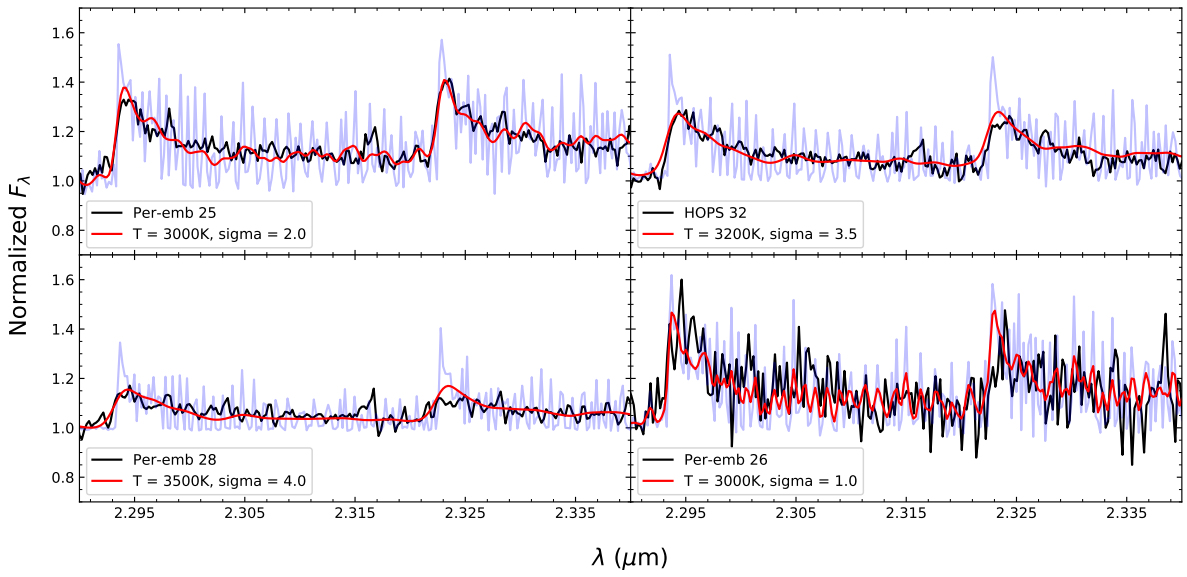

Figure 2.2: Our observed CO v=2–0 emission bands (black) overplotted with that of inverted PHOENIX model spectra before (light blue) and after (red) smoothing with a Gaussian filter (Section 2.4.1). The reasonable match between our data and model spectra demonstrate that spectrally broadened CO emission is detected in these four Class 0 objects.

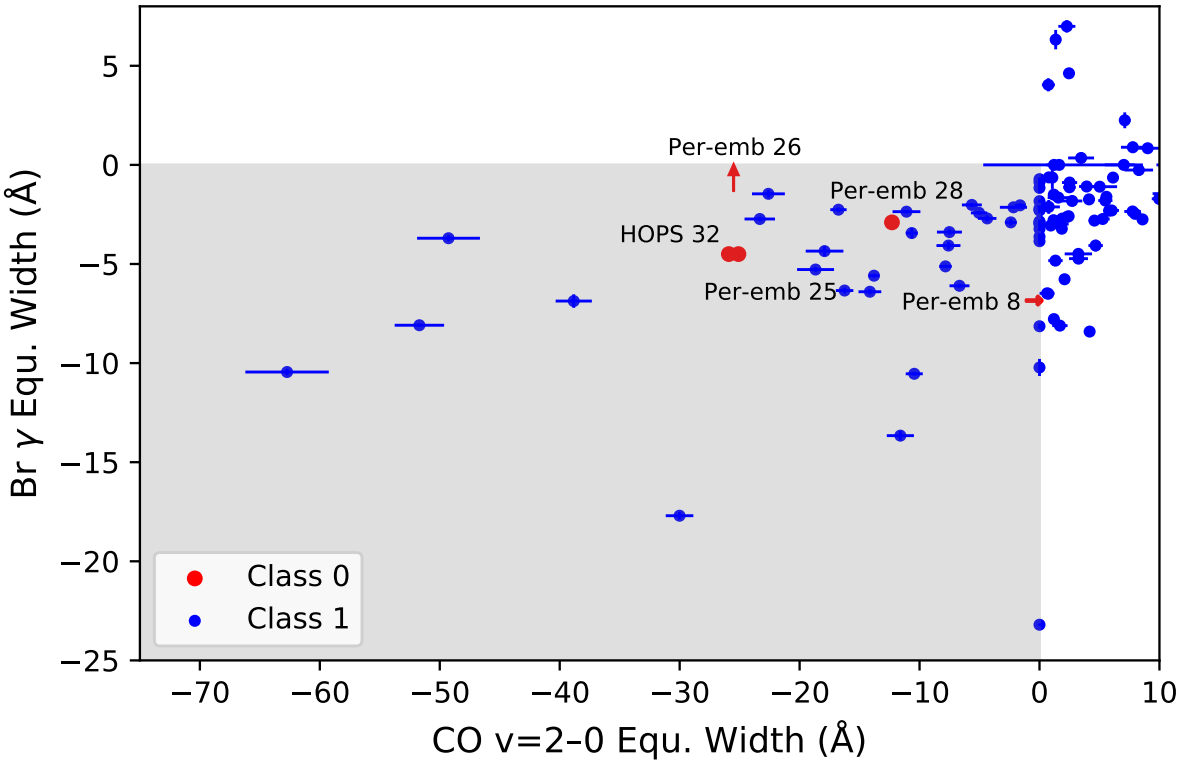

Figure 2.3: Br γ equivalent widths vs. the CO v=2–0 band equivalent widths. Red points correspond to observed Class 0 sources (this work) while blue points correspond to observed Class I sources (Connelley & Greene, 2010). The shaded region demarcates sources with observed emission in both features. Undetected lines are represented with arrows, corresponding to 3σ upper limits. We find the broad distribution of these EWs appear to overlap between Class 0 and Is (Section 2.4.2).

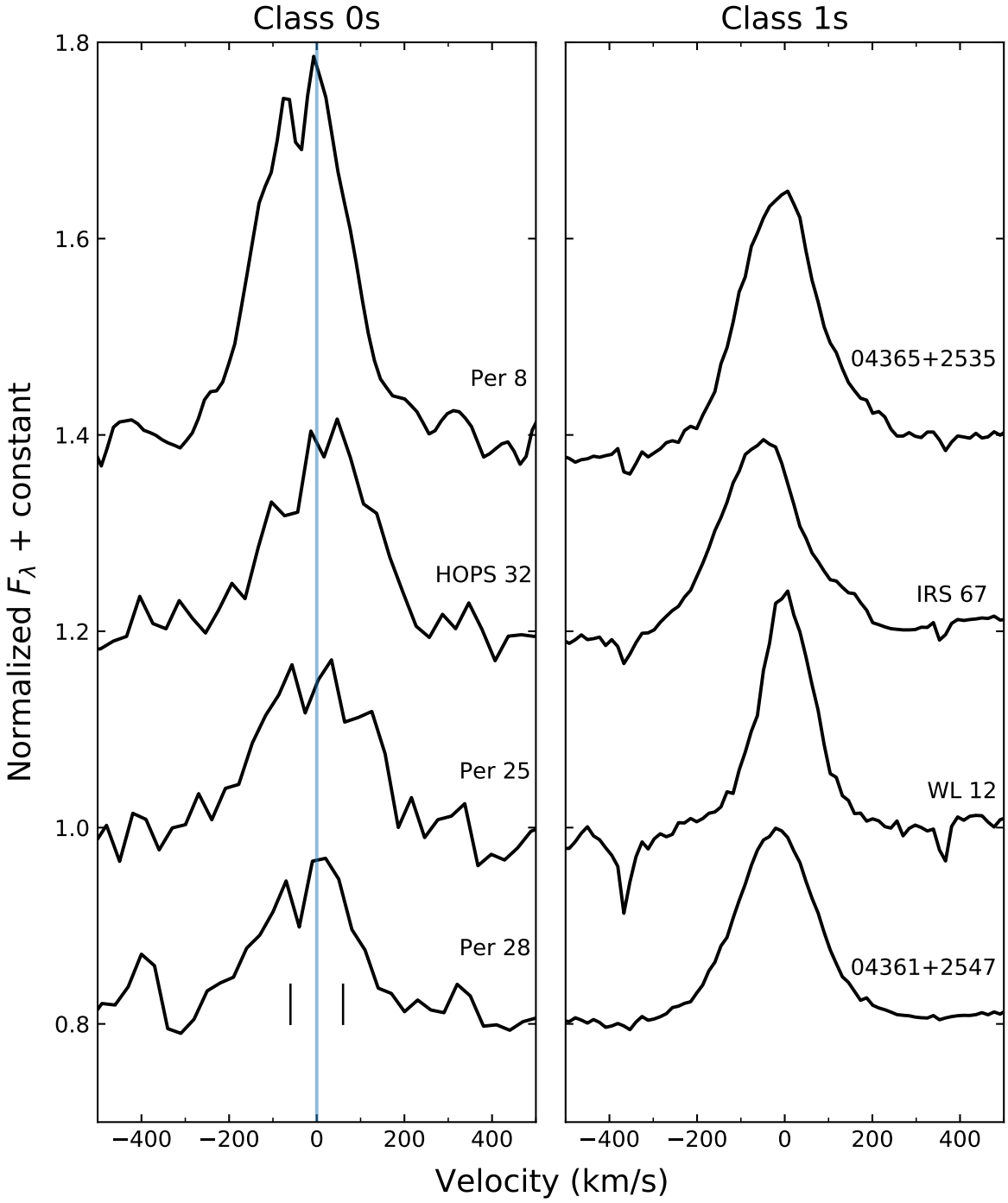

Figure 2.4: Comparison of observed Br γ line profile between our Class 0s (left) and the Class Is from Doppmann et al. (2005) (right). Spectra have been normalized with a linear fit to the continuum and shifted into the systemic reference frame (Section 2.4.2). We overplot a bisecting line in blue to roughly quantify the relative blue and red shifted flux contributions visually. The black ticks represent the approximate velocity resolution of our data ($\sim$120 km/s). The high resolution spectra of the Class Is (R=18,000) has been downgraded to match our moderate MOSFIRE resolution (R=2,400). In Section 2.5.1, we argue the similarity between our Class 0 line profiles and that of Class 1s hints towards the presence of a magnetosphere at the Class 0 stage.

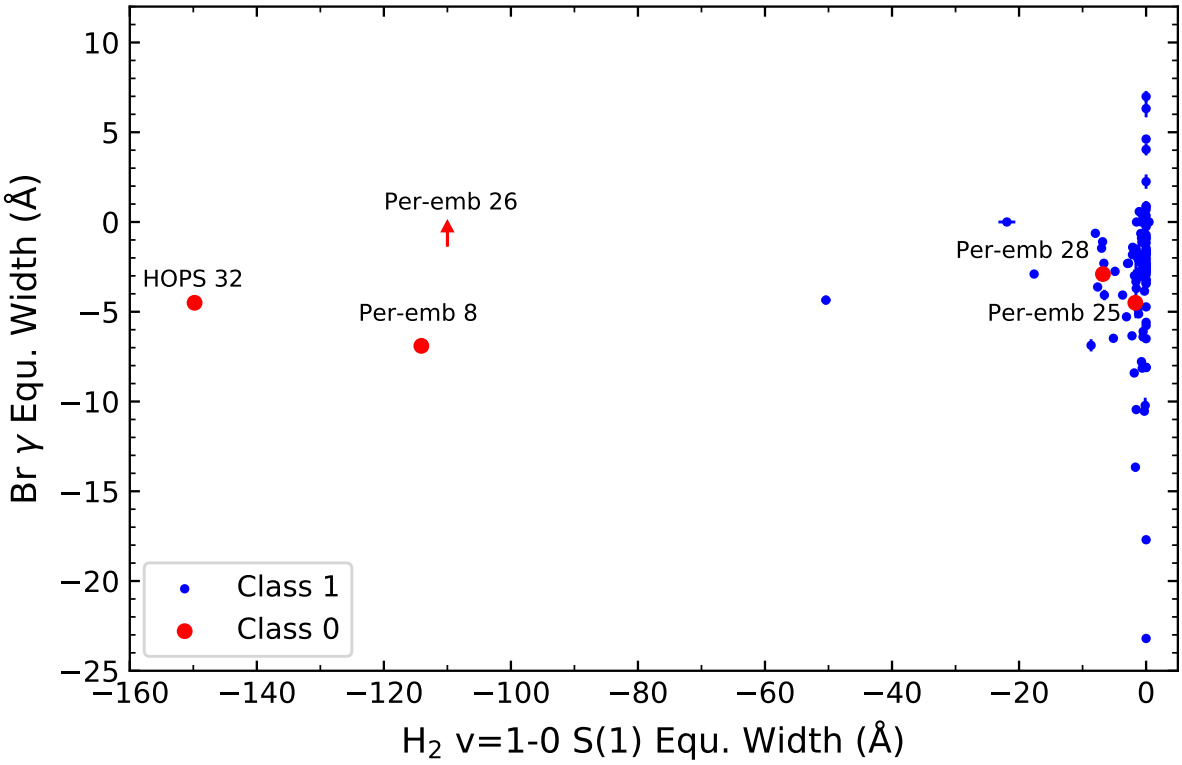

Figure 2.5: Br γ equivalent widths vs. H_2 v=1-0 S(1) equivalent widths. Red points correspond to observed Class 0 sources (this work) while blue points correspond to observed Class I sources (Connelley & Greene, 2010). Undetected lines are represented with arrows, corresponding to 3σ upper limits. We find some of our Class 0s exhibit significantly higher H_2 v=1-0 S(1) EWs than this sample of Class Is (Section 2.4.3).

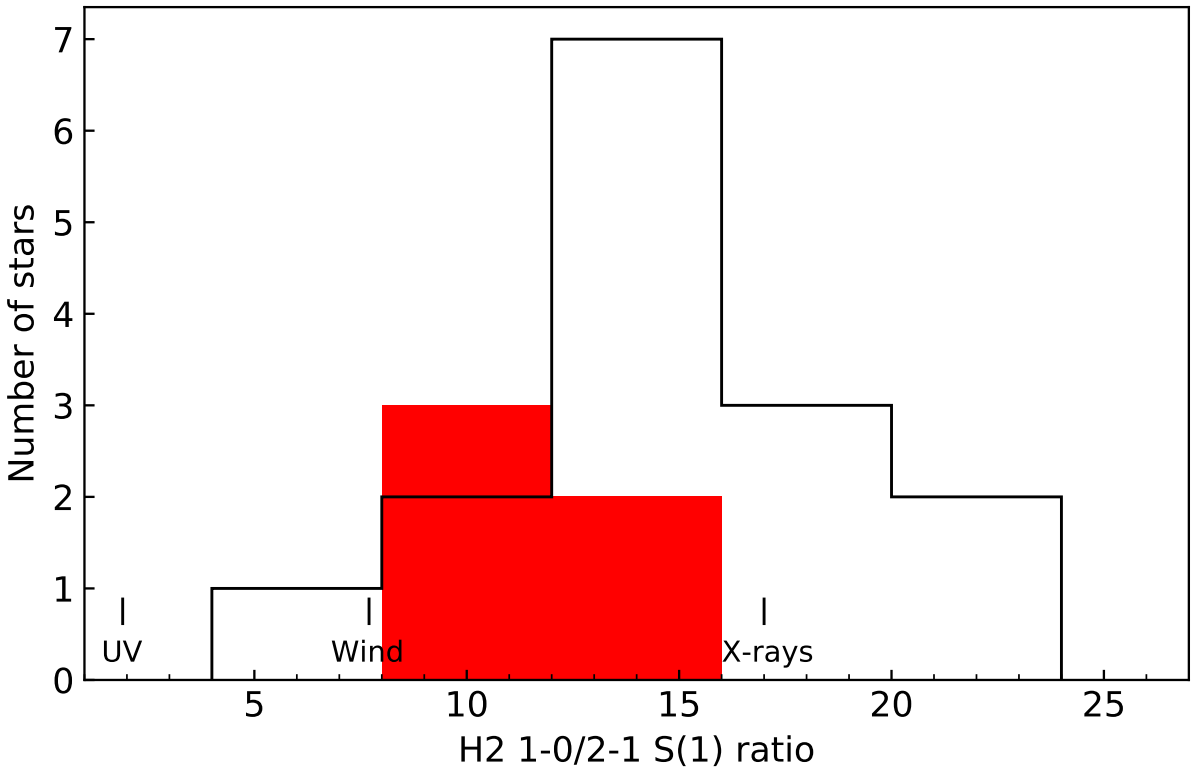

Figure 2.6: Histogram of H_2 ν = 1–0/2-1 S(1) line ratios between our Class 0s (red) and the Class Is observed in Greene et al. (2010) (black). We find the line ratios of our Class 0s argue in favor of shocks in a wind or X-rays as the most likely H_2 source excitation mechanism.

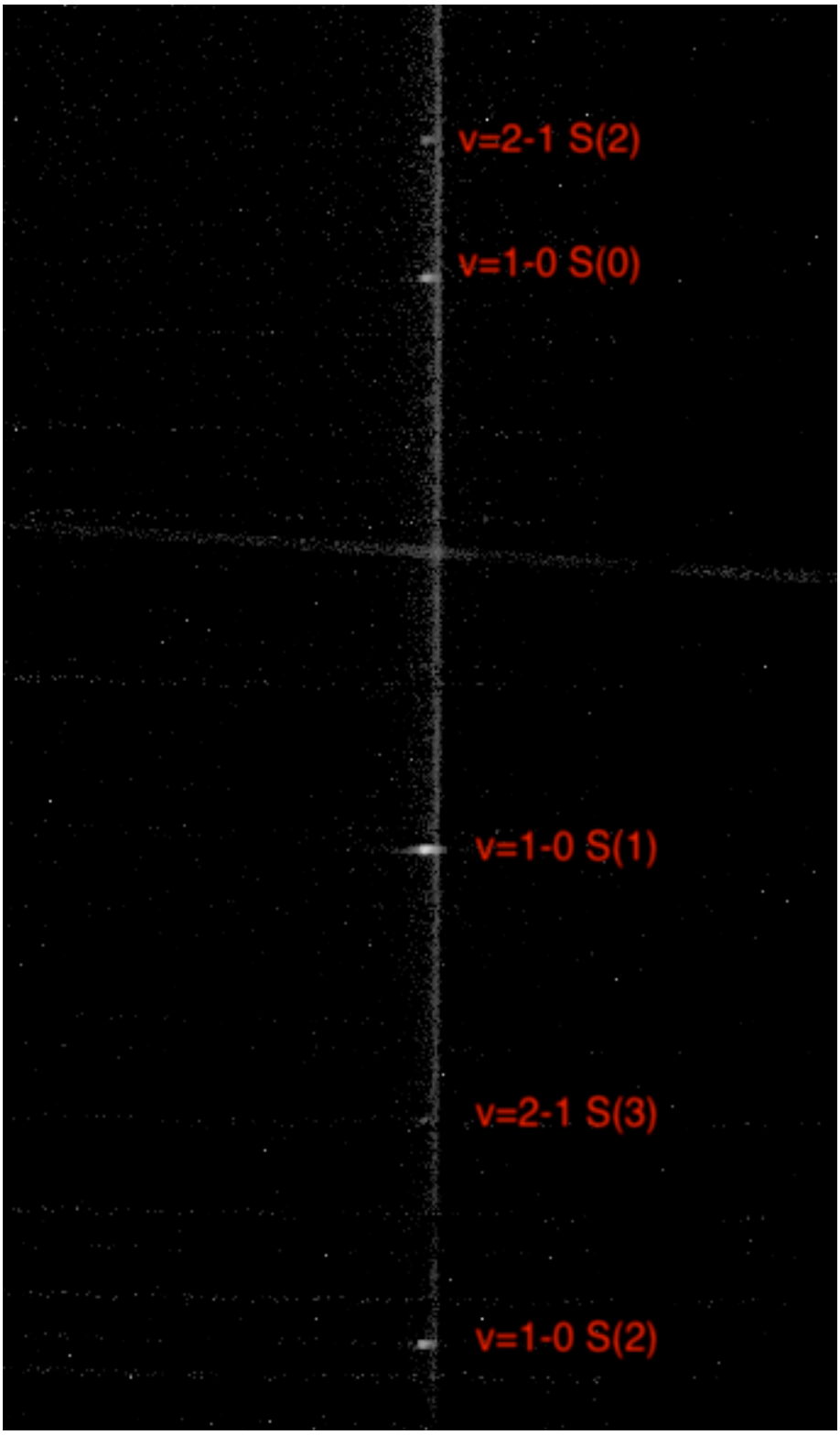

Figure 2.7: An example of the extended H_2 emission seen in our reduced 2d spectral images. The frame cut is centered on the observed continuum of Per-emb 8 from a single 120s exposure observed on UT date 2019 October 14. We label the individual features and discuss the slit position angle (PA) alignment with the PA of known outflows in Section 2.4.4.

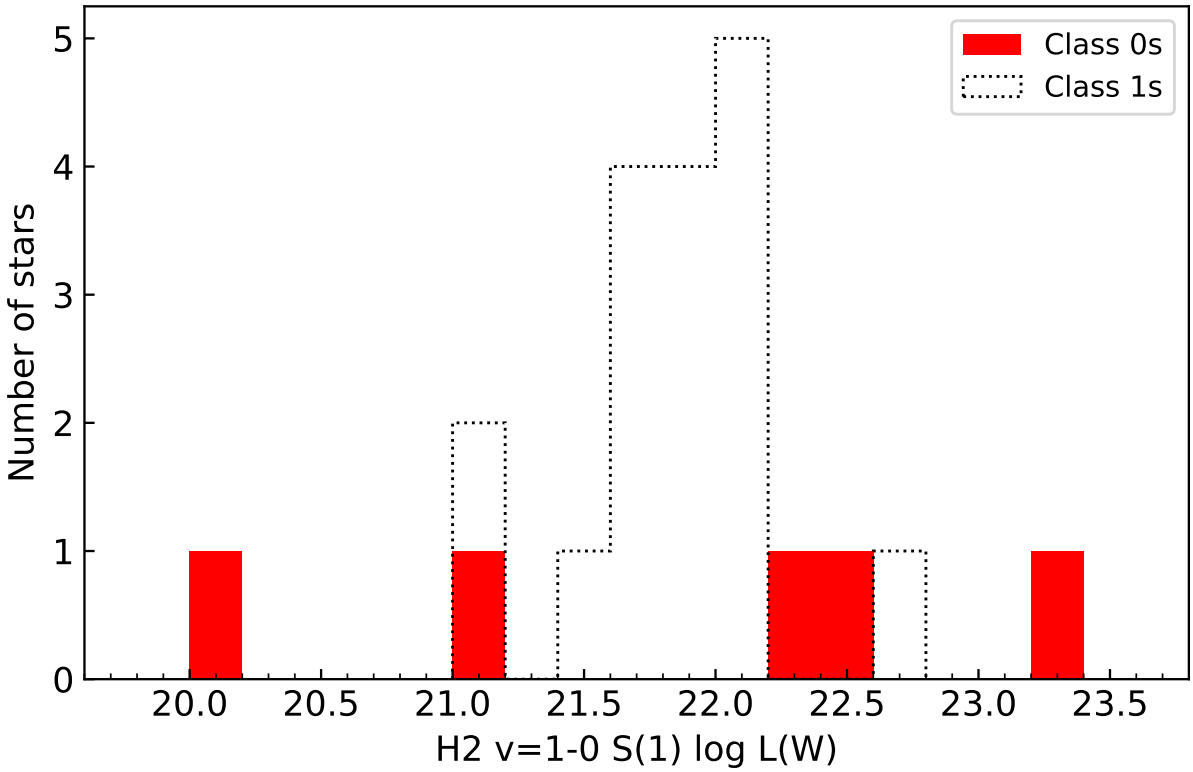

Figure 2.8: Histogram of H_2 v = 1–0 S(1) line luminosities between our Class 0s (red) and the Class Is observed in Greene et al. (2010) (black). We note our Class 0 line luminosities have high uncertainties (Section 2.4.5); the visual extinctions derived for de-reddening may be underestimated given the complicated physical nature of our Class 0s (e.g. non-symmetrical envelopes, scattered light). It remains unclear the extent to which the line luminosities between these two populations differ until more precise Class 0 extinction estimates can be derived.

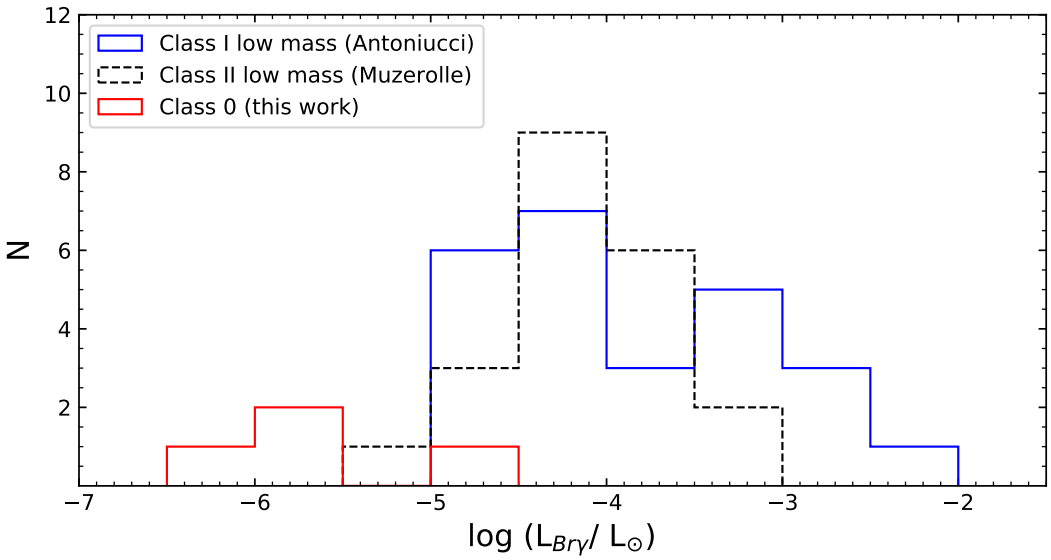

Figure 2.9: Histogram of Br γ line luminosities between our Class 0s (red), low mass Class Is (Antoniucci et al. 2008) (blue), and low (Muzerolle et al. 1998) mass Class IIs (black). As in Figure 2.8, we note our Class 0 line luminosities have high uncertainties (Section 2.4.5). The discrepancy seen between our low Class 0 Br γ luminosities and that of Class I/IIs could be resolved if we have systematically underestimated the extinctions of Class 0 systems by a factor of 2. Overall, it remains unclear the extent to which the line luminosities of these two populations differ until more precise Class 0 extinction estimates can be derived.

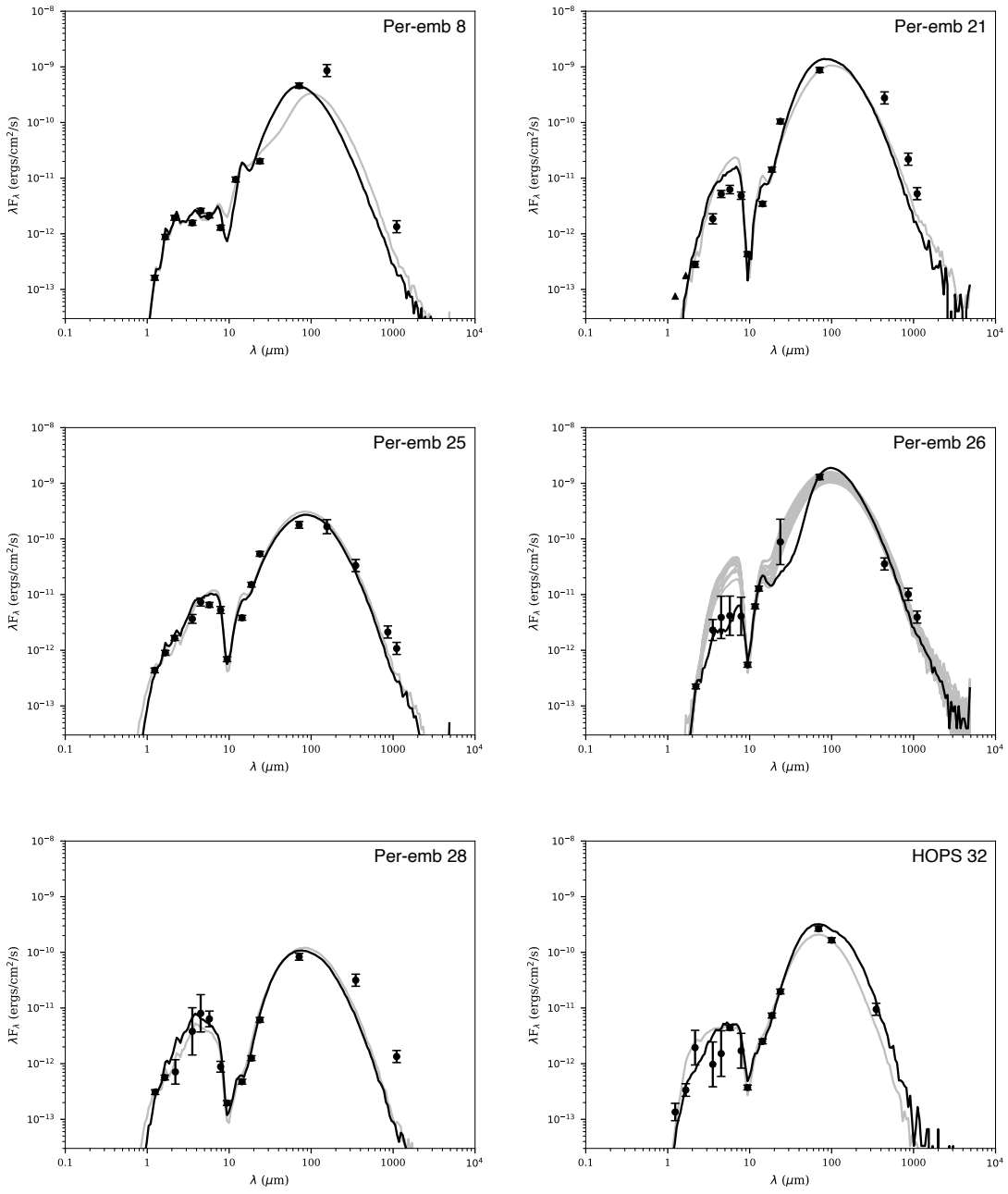

Figure 2.10: The results of SED fitting for our Class 0 sources using the SED models of Robitaille et al. (2006). We show both the best-fit model (black) and the family of models for which $\chi^2 - \chi^2_{best}$ per data point < 3. We detail our methodology and interpret these results in Appendix Section 2.7.

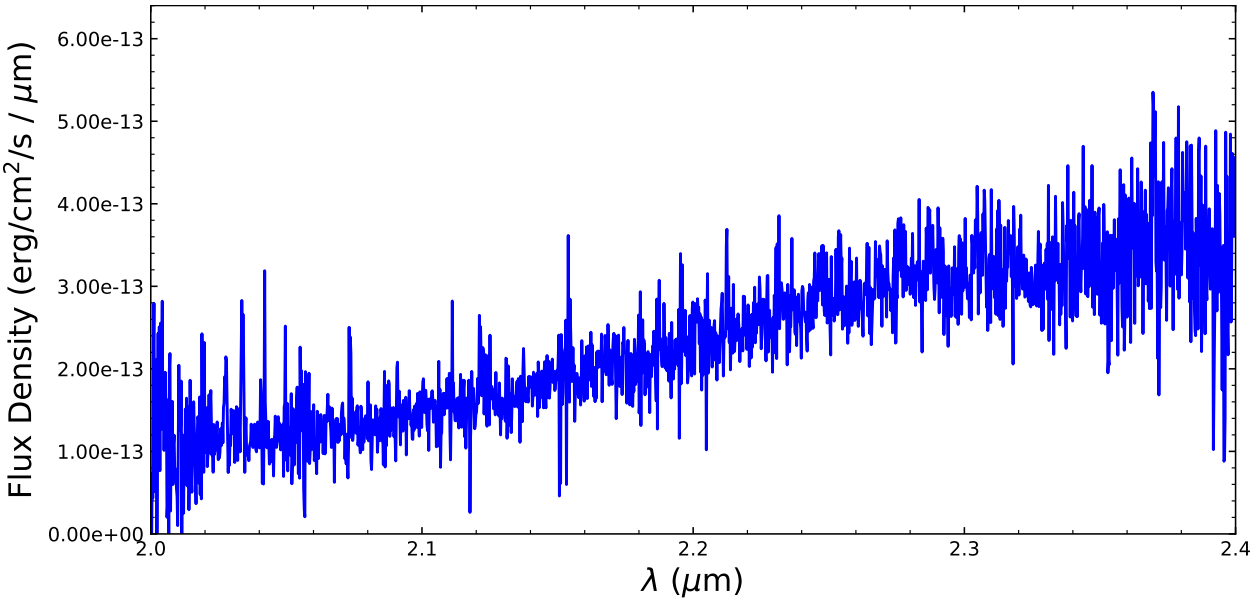

Figure 2.11: Near-IR MOSFIRE spectrum of HOPS 44 taken on UT Oct 13 for a total integration time of 12 minutes. We exclude HOPS 44 from the final sample of Class 0 we analyze in Section 2.4 due to the low S/N of its observation (Appendix Section B).

Chapter 3

Assessing Spectroscopic Binary Multiplicity Properties Using Robo-AO Imaging

The following work was originally published in The Astrophysical Journal (Laos et al., 2020) and is reprinted below in its entirety.

Stefan Laos[1], Keivan G. Stassun[1,2], Robert D. Mathieu[3]

[1]Department of Astrophysics, Vanderbilt University, Nashville, TN 37235, USA

[2]Department of Physics, Fisk University, Nashville, TN 37208, USA

[3]Department of Astronomy, University of Wisconsin-Madison, Madison, WI 53706, USA

3.1 Original Abstract

We present higher-order multiplicity results for 60 solar-type spectroscopic binaries based on 0.75μm imaging data taken by the Robotic Adaptive Optics system (Robo-AO) at the Kitt Peak 2.1m telescope. Our contrast curves show sensitivity of up to $\sim$5 mag at $\sim 1''$ separation; at very small separations, we identify candidate companions from image deviations relative to the point spread function. We find candidate tertiary companions for 62% of our binaries overall, but find this fraction is a strong function of the inner binary orbital period; it ranges from $\sim$47% for $P_{\rm bin} > 30^d$ to as high as $\sim$90% for $P_{\rm bin} \lesssim 5^d$. We similarly find increasing tertiary companion frequency for shorter period binaries in a secondary sample of *Kepler* eclipsing binaries observed by Robo-AO. Using *Gaia* distances, we estimate an upper limit orbital period for each tertiary candidate and compare the tertiary-to-binary period ratios for systems in the field versus those in star-forming regions. Taken all together, these results provide further evidence for angular momentum transfer from three-body interactions, resulting in tight binaries with tertiaries that widen from pre-main-sequence to field ages.

3.2 Introduction

Although many of the underlying mechanisms and outcomes of the star-formation process remain under debate, the prevalence of stellar multiplicity is undisputed, with more than half of all stars having at least one companion. In the past decade, stellar multiplicity studies (e.g., Raghavan et al., 2010; Sana et al., 2014; Tokovinin, 2014a; Fuhrmann et al., 2017) have focused on volume-limited samples in distinct spectral-type ranges to achieve unbiased statistical inferences of multiple systems. Others (e.g., Rucinski et al., 2007; Riddle et al., 2015; Hillenbrand et al., 2018) have used high-resolution, adaptive-optics imaging to identify and characterize new systems.

In particular, high spatial resolution campaigns at longer wavelengths have the ability to maximize detections of faint distant companions. Tokovinin et al. (2006) surveyed 165 solar-type spectroscopic binaries (SBs) and found that virtually all ($\sim$96%) short-period binary systems ($P_{\rm bin} < 3^d$) had tertiary companions.

This seminal finding has motivated a number of follow-on studies to explore the potential effects of, as well as the evolutionary pathways of, binaries in tertiary systems. The dynamics introduced by tertiaries could have significant consequences for the evolution of young stellar objects. For example, in the most recent review of benchmark pre-main-sequence (PMS) eclipsing binaries (EBs), Stassun et al. (2014) found that the properties of those in triple systems constituted the most highly discrepant cases when compared to PMS stellar evolution models, which may be explained if the tertiary inputs significant energy into one or both binary stars during periastron passages (see, e.g., Gómez Maqueo Chew et al., 2019).

More generally, the dominant physical mechanism by which the tertiary influences the creation of tightly bound binaries has not yet been established. Lidov-Kozai cycles with tidal friction (KCTF; Eggleton & Kiseleva—Eggleton, 2001) have been hypothesized but require a long dynamical timescale and only operate for certain mutual orbital inclinations. Thus, KCTF is suspected to only be capable of producing a fraction of the total known population of close binaries.

Recent simulations of newborn triple systems (e.g., Reipurth & Mikkola, 2012) have found binary orbital hardening occurring early in the systems' evolution, whereby compact triple sys-

tems dynamically unfold into wider hierarchical structures. In this scenario, triple systems find themselves in the tight binary – wide tertiary configuration well before evolving onto the main sequence. These findings have been corroborated by recent population synthesis work (e.g., Moe & Kratter, 2018), which found $\sim$60% of close binaries form in this manner, with additional energy dissipation arising from primordial gas-disk interactions in the binary.

Making progress in determining the respective rates of these different mechanisms requires a greater number of binary-star systems with well known periods, distances, and ages, and for which the presence of a tertiary companion is well established. In addition, the fundamental result of an increased tertiary occurrence among the tightest binaries (Tokovinin et al., 2006) should ideally be reproduced with independent samples, given its importance in motivating and constraining these questions.

In this paper, we seek to test the reproducibility of the cornerstone result of Tokovinin et al. (2006) and explore the evidence of potential evolutionary pathways for triple systems. In Section 3.3, we describe our sample of observed binaries and list some of their fundamental physical properties. We also describe the source and nature of our data along with data reduction and processing procedures. In Section 3.4, we describe our search for additional companions to our sample using published catalogs and with *Gaia* DR2, in some cases offering additional confirmation of our Robo-AO multiplicity identifications. In Section 3.5, we report the results of our Robo-AO SB multiplicity survey and compare with complementary Robo-AO observations of *Kepler* EBs. In Section 3.6, we discuss the implications of our results on current star-formation and binary-evolution theory. Finally, in Section 3.7, we conclude with a brief summary of our findings.

3.3 Data and Methods

3.3.1 Spectroscopic Binary Star Samples Used

The goals of this study include examining multiplicity fractions as a function of inner binary period and comparing the derived properties of our identified tertiaries with known multiples from

the literature. Therefore, our Robo-AO target list required a large sample of spectroscopic binaries (SBs) with known orbital periods and distances. To this end, we use the Troup et al. (2016) sample of main-sequence Apache Point Observatory Galactic Evolution Experiment (APOGEE) stars identified with stellar and substellar companions, which includes 178 systems within 1 kpc. In addition, we also include the Torres et al. (2010) sample of benchmark eclipsing binaries (EBs which are also SBs). These 94 systems have known orbital periods and distances (Stassun & Torres, 2016) as well as component masses and radii derived to an accuracy of 1–3%.

These two samples constitute the master list of SBs in our Robo-AO survey, of which we have observed 33 EBs from the Torres et al. (2010) sample and 43 targets from the Troup et al. (2016) sample, with orbital periods of the combined sample spanning the range 0.3–1880 d. Although all 43 Troup sources are radial velocity variable, we verify a clean sample of SBs by requiring the derived minimum mass of the companion to be greater than that of a brown dwarf ($0.013 M_{\odot}$). We also conservatively require the significance of the RV variations in sigma units to be greater than 10. This identifies 27 Troup et al. (2016) SBs (thus 33 + 27 = 60 SBs in total) for our sample. We do not consider the remaining 16 Troup et al. (2016) stars in our analysis in Sections 3.4 or 3.5, but for the benefit of future studies we report any companions that we identified in our Robo-AO imaging in Table 3.5. All of the targets in our sample have parallaxes reported in the *Gaia* second data release (DR2) with distances in the range 40–2200 pc. Graphical summaries of some basic parameters for our Robo-AO SB sample are displayed in Figure 3.1. Their properties and identifications are listed in Table 3.1.

For an independent test sample, we also made use of the published Robo-AO observations of *Kepler* EBs from Law et al. (2014), originally drawn from the master sample of *Kepler* objects of interest (KOIs). To enable a direct comparison with our Robo-AO sample, we trim the initial sample of 1065 KOI EBs as follows. To remove potential EB false positives, we required a minimum primary eclipse depth of 1 mmag, as fit by the *Kepler* EB pipeline's `polyfit` algorithm (Prša et al., 2008). Similarly, we also required all systems to have a successful "morphology" classification (between 0 and 1) as output by the Local Linear Embedding (LLE) of the *Kepler* EB

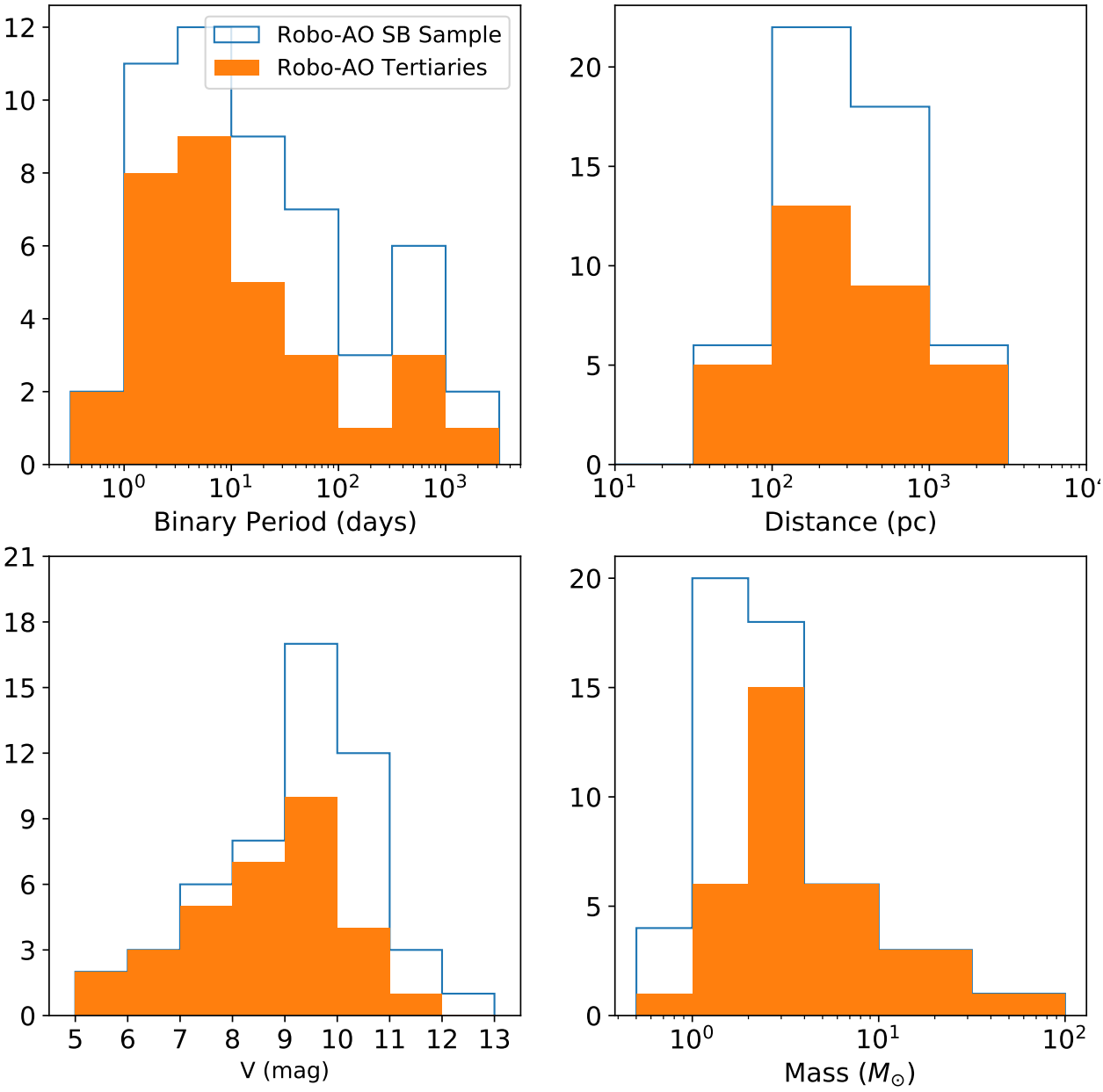

Figure 3.1: Representative histograms of stellar properties for the Robo-AO SB sample (unfilled) and the subset with candidate tertiary companions (filled). We note the mass histograms refer to binary mass except for our Troup et al. (2016) sources, which only have known mass values for the primary. The bias against detection of very low-mass companions (lower-right panel) is a reflection of the sensitivity limit of our data for faint sources (lower-left panel).

Table 3.1: Robo-AO SB Sample

Name	R.A. (deg)	Dec. (deg)	$P_{\rm bin}$ (d)	V (mag)	Multiplicity Flag[a]	Sample ID[b]
V432 Aur	84.38524	37.08689	3.082	8.05	T	Stassun & Torres - EB
WW Aur	98.11313	32.45482	2.525	5.82	T	Stassun & Torres - EB
HS Aur	102.82702	47.67335	9.815	10.05	B	Stassun & Torres - EB
HD 71636	127.48465	37.07095	5.013	7.90	U	Stassun & Torres - EB
KX Cnc	130.69238	31.86242	31.22	7.19	T	Stassun & Torres - EB
2MASS J10352794+2512348	158.86626	25.20971	25.09	9.73	B	Troup - SB
2MASS J11452973+0159347	176.3738	1.99299	1033.875	9.96	B	Troup - SB

The full table is available in the electronic version of the Journal. A portion is shown here for guidance regarding its form and content.

[a] Multiplicity flag: B = binary, T = candidate triple, U = undetermined (Section 2.2).

[b] Sample ID: Stassun & Torres - EB = EBs from Stassun & Torres (2016); Troup - SB = SBs from Troup et al. (2016).

Table 3.2: Robo-AO KOI EB Sample

KOI	R.A. (deg)	Dec. (deg)	P_{bin} (d)	V (mag)	Multiplicity Flag[a]
5774	283.86634	47.22828	2.4275	10.834	T
5993	285.14501	39.18703	4.2647	13.0	T
971	286.01929	48.86677	0.5331	7.642	B
6109	287.83336	39.22124	22.9135	11.911	T
1728	288.97163	44.62465	12.7319	12.069	B
2758	289.74253	39.26713	253.3623	12.168	B
1661	290.73807	39.91969	1.8955	11.601	T

The full table is available in the electronic version of the Journal. A portion is shown here for guidance regarding its form and content.
[a] Multiplicity flag: B = binary, T = triple.

pipeline (Matijevič et al., 2012). We excluded all targets fainter than the faint limit of our sample ($V < 12.5$) by converting their *Kepler* magnitudes to V via the published *Kepler* color-temperature relation. This also requires the EBs to have nominal effective temperatures listed in the *Kepler* Input Catalog. This leaves a remaining sample of 109 KOI EBs.

Of these 109, 52 have Robo-AO observations, of which 22 have clear determinations of the presence or absence of a companion (Table 3.2). These identifications correspond to multiple Robo-AO KOI survey efforts taken at the Palomar 1.5m telescope, including Law et al. (2014), Baranec et al. (2016) Ziegler et al. (2017), and Ziegler et al. (2018).

3.3.2 Robo-AO Imaging

Robo-AO is an autonomous laser adaptive optics system stationed at the Kitt Peak 2.1m Telescope from November 2015 to June 2018. Robo-AO has a field size of $36''$on a side with a pixel scale of 35.1 milli-arcsec per pixel (Jensen-Clem et al., 2017). High spatial resolution images of the target stars were taken between November 2017 and June 2018. We observed 76 unique targets in the i' bandpass (6731 - 8726Å) with 90-s exposures. Over the 90 second exposure, about 773 individual frames are generated. Target images were initially processed with the Robo-AO "bright star" pipeline as described in Law et al. (2014).

While this pipeline was appropriate for the majority of our Robo-AO SB images, we note five faint SB systems (2MASS IDs: J07381910, J16515260, J19301035, J19305116, and J19412976) that were not properly reduced. As noted in Jensen-Clem et al. (2017), the images in these cases failed to correctly center the PSF, leading to a single noticeably bright pixel in the center of the image. We remove these targets from the sample to avoid biasing our multiplicity analysis in Section 4, leaving 55 SBs. To maximize our detection of tertiaries at small angular separations, the images were further processed by the "high contrast imaging" pipeline described in Jensen-Clem et al. (2017).

This pipeline first applies a high-pass filter on a $3\farcs5$ frame windowed on the star of interest to lessen the contribution from the stellar halo. A synthetic point spread function (PSF) is then subtracted, generated via Karhunen-Lo'eve Image Processing (KLIP, a principal component analysis algorithm that whitens correlated speckle noise; Soummer et al., 2012). A representative sample of PSF diversity is achieved using a reference library of several thousand $3\farcs5$ square high pass filtered frames that have been visually vetted to reject fields with more than one point source. This technique of Reference star Differential Imaging (RDI; Lafrenière et al., 2009) results in the final PSF-substracted image, from which we make our multiplicity determinations.

Measurement of multiple star systems' position angles and separations also require a precise astrometric solution for the optical instrument. Nightly observations of densely populated globular clusters are used to establish and update this solution as described in Section 6 of Jensen-Clem et al. (2017). After each science target is fully reduced, the pipeline also produces a 5σ contrast curve by simulating companions and properly correcting for algorithmic throughput losses using the Vortex Image Processing (VIP) package (Gomez Gonzalez et al., 2017). Examples of our Robo-AO images pre- and post-processing, along with their corresponding contrast curves, are shown in Figure 3.2.

The expected Robo-AO error budget and performance is summarized in Table 2 of Jensen-Clem et al. (2017). At our observed Strehl ratios of a few percent, we expect a delivered FWHM of $\sim 0\farcs15$. The majority of our SB sample have unambiguous non-detections or else distortions

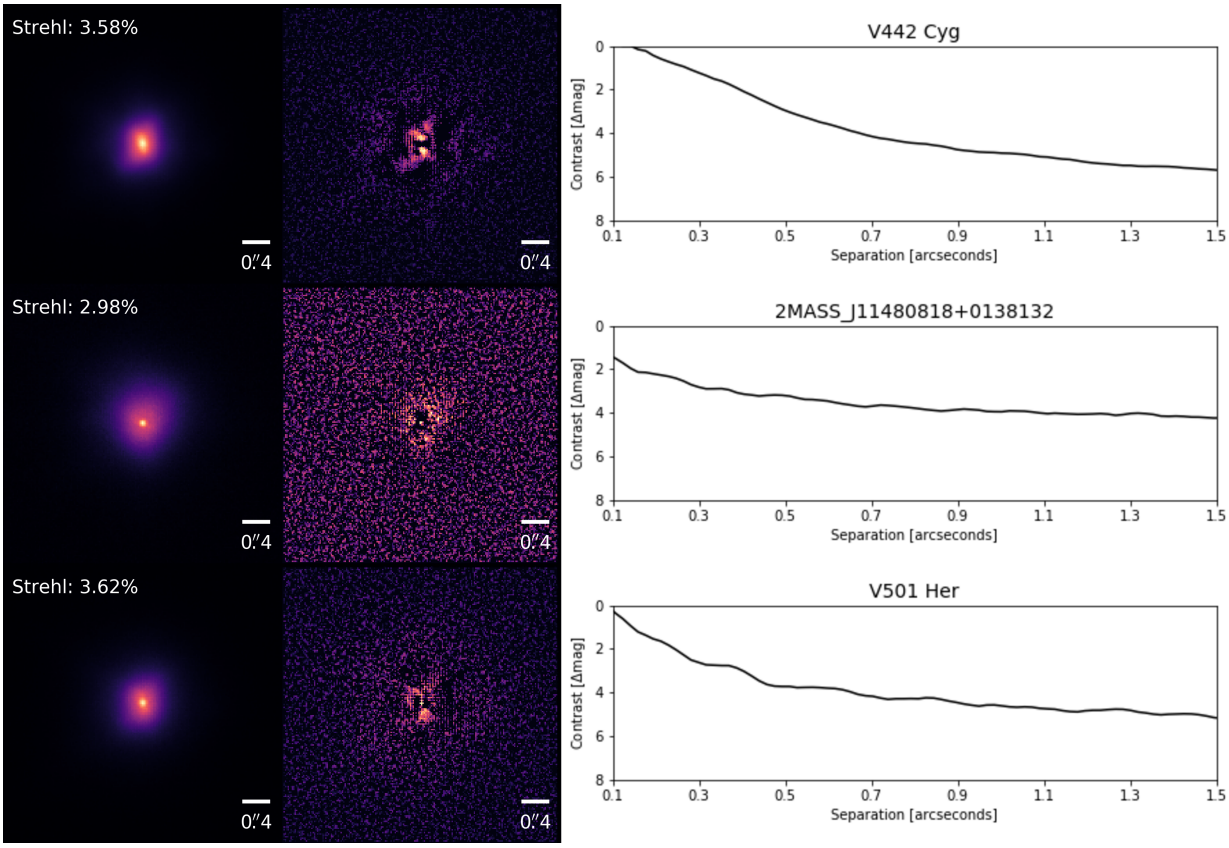

Figure 3.2: Top Panel: Robo-AO image (left), PSF subtracted image (middle), and constrast curve (right) of V442 Cyg; residuals reveal distortion in the pre-subtracted image that suggests a tertiary companion to the unresolved spectroscopic binary. Middle Panel: Robo-AO Image, PSF subtracted image, and contrast curve of 2MASS J11480818+0138132; residuals clearly do not suggest a tertiary companion. Bottom Panel: Robo-AO Image, PSF subtracted image, and contrast curve of V501 Her; residuals indicate an unclear case.

suggestive of a tertiary companion upon visual inspection of their PSF subtracted images. We assign a multiplicity flag of "T" for the cases with clear image distortions, or "B" for cases of undetected companions. In a small number of cases, we observe residuals that weakly imply a quadruple but are suspected to be artifacts from the PSF-subtraction process. We assign these cases a multiplicity flag of "T(Q?)" in Figures 3.9–3.11. Lastly, three cases have difficult to interpret residuals for which we are unable to determine identifications for (Figure 3.2, lower right) and are thus assigned a multiplicity flag of "U". Our analysis in Section 3.5 excludes all unclear cases, resulting in a remaining sample of 52 SBs.

To be clear, we do not resolve individual components for the majority of our Robo-AO obser-

Table 3.3: Robo-AO and Gaia Identified Candidate Tertiaries

Name	P_{bin} (d)	Sep. (")[a]	Dist. (pc)	Proj. Sep. (AU)[a]	Mass ($M_\odot$)[b]	~log (P_3) (yr)[a]	GOF_AL[c]	D[d]
V432 Aur	3.082	0.12	127.1	15.6	2.3	1.2	5.45	0.0
WW Aur[f]	2.525	0.13	90.9	12.2	3.8	0.9	29.27	32.69
KX Cnc	31.22	0.12	49.3	6.1	2.3	0.5	11.84	0.0
2MASS J11480818+0138132[e]	400.82	119.1	235.0	27988.1	1.1	6.2	64.57	223.42
2MASS J12260547+2644385	300.056	0.22	127.4	27.7	0.8	1.8	33.07	80.09
BH Vir	0.817	0.19	149.3	28.1	2.2	1.5	7.75	0.0
AD Boo[f]	2.069	0.25	195.4	49.6	2.6	1.9	25.38	13.91

The full table is available in the electronic version of the Journal. A portion is shown here for guidance regarding its form and content.

[a] We note the reported quantities in these columns are upper limits.

[b] For Stassun & Torres SBs, masses are sourced from the detached eclipsing binary catalogue (DEBCat, Southworth (2015)).

[c] *Gaia* Astrometric Goodness of Fit in the Along-Scan direction.

[d] *Gaia* significance of the Astrometric Excess Noise. [e] Wide tertiary companion identified by Gaia CPM analysis (Section 3.1).

[f] Multiple status astrometrically confirmed by Gaia (Section 3.2).

vations (Figures 3.9–3.11). Many of the triples suggested in the PSF-subtracted images are the result of clear elongation compared to the point-source like observations of SBs with no detected companions. While the residuals from this process do not allow us to unambiguously identify the presence of a companion, we use them to flag candidates and then further vet the sample with *Gaia* astrometry and with previous observations (Sec. 3.4).

We note the image residuals cannot be used to reliably measure flux contrasts; for each identified candidate tertiary, we only measure an upper limit to its angular separation and a position angle (PA) by measuring the positions of the two peaks in the PSF subtracted images, representing the angular scale of the image distortion (i.e., the combined effect of the central unresolved SB and the putative tertiary companion), carefully accounting for the slight difference in x and y pixel scales (noted in the appendix of Jensen-Clem et al., 2017). While the distribution of PAs (Figure 3.3) is statistically consistent with a uniform distribution as expected, there may be a slight preference for PAs near 180/360 degrees that could be non-physical; these systems would benefit from followup observation (but see also Sec. 3.4).

The angular separations are translated into physical upper limit projected separations using the *Gaia* DR2 distance to each system. We note the masses for each target have been sourced from the literature and correspond to the binary mass, except for our Troup et al. (2016) sources, which only have known mass values for the primary. These masses are used to derive a rough upper limit estimate of the tertiary period. We report its logarithm along with our measured angular and projected separations for all of our multiple systems in Table 3.3. We note that our period estimates, however, can significantly vary from the true period in cases where the projected separation is much different than the true semi-major axis of the system.

The resolution and sensitivity limits of our Robo-AO observations hinder our ability to detect long period ($P_3 \gtrsim 10^4$ yr) tertiaries. The $3\farcs5$ frame centered on each of our sources corresponds to a maximum detectable angular separation of $1\farcs75$. For a typical tertiary in our sample, this corresponds to a tertiary period of $\sim$9200 yr. Thus, very long period ($P_3 \gtrsim 10^4$ yr) tertiaries generally do not fall within our Robo-AO field of view.

3.4 Catalog Search for Additional Companions

As the most sensitive probe of parallaxes and proper motions, *Gaia* provides a powerful opportunity to search more comprehensively for additional companions to our Robo-AO SB sample. Resolved common proper motion (CPM) companion matches have the ability to corroborate, or in some cases refine, our prior multiplicity determinations. Additionally, astrometric quality information of unresolved companions can similarly serve to confirm Robo-AO-identified multiples. As a final companion check, we also query the WDS catalog for prior multiplicity information on our Robo-AO targets.

3.4.1 Gaia Common Proper Motion Candidates

We begin by crossmatching our Robo-AO SBs with the *Gaia* DR2 catalog to obtain both parallax and proper motion information for each target. We then query *Gaia* DR2 to list all targets found within a $5'$ aperture centered on each Robo-AO binary. The aperture size chosen searches for any wide companions outside of our $3.''5$ Robo-AO field of view while minimizing those with separations that are unlikely to be bound. For both this larger sample as well as our Robo-AO-Gaia crossmatch, we apply the suggested corrections to the published *Gaia* DR2 magnitudes following Evans et al. (2018) and Maíz Apellániz & Weiler (2018), depending on the magnitude range considered. For the brighter ($G < 11.5$) stars in both samples, we also apply a proper motion correction due to the inertial spin of the Gaia DR2 proper motion system (Lindegren, 2018).

Our wide search returns 49343 sources, 6810 of which do not have parallax or proper motion information. With the remaining 42533 sources, we follow a similar procedure to the Gaia companion candidate cuts chosen by Jiménez-Esteban et al. (2019) to find wide co-moving binaries. In our case, we choose more lenient fractional error cuts on parallax (20%) and proper motion (50%) to maximize our chances of identifying fainter companions while still ensuring reasonably high quality measurements. This vetting reduces the total number of candidate companions to 5332.

To check for CPM companions that are likely to be physically associated, we then compare

the parallax and proper motion information of these candidates with their corresponding Robo-AO counterpart. We require their respective parallax and proper motion measurements to agree within 2.5σ, with σ being the larger error of the two. For the remaining 10 candidates, we estimate their projected separations, with distances derived from the error weighted arithmetic mean parallax of each pair. Again, we note these estimates can vary significantly from the true semi-major axis of the orbit. As a final requirement, we set a generous separation threshold of 50000 AU to exclude pairs that are most likely not physically bound while recognizing the approximate nature of our derivations.

The result is the identification of three CPM companion candidates. We report a faint ($G \sim 18.9$) companion to RT CrB at an angular separation of $9\farcs5$. We change its multiplicity designations from triple candidate to quadruple candidate and make a note of its non-hierarchical ($2 + 1 + 1$) configuration. We also report a faint ($G \sim 18.9$) companion to BK Peg at an angular separation of $104\farcs4$ and a ($G \sim 11$) companion to 2MASS J11480818+0138132 at an angular separation of $119\farcs1$. We change their multiplicity designations from binary to triple.

Lastly, we return to the subsample of 7108 sources that *Gaia* does not record parallax or proper motion information for. Although these sources cannot be vetted for association, we check for those that have separations from their Robo-AO counterpart near Gaia's resolution limit of $1''$. We find one match to 2MASS J12260547+2644385, a confirmation of the wide ($\sim 1''$) triple companion seen in our Robo-AO imaging. Considering the other Robo-AO system with a relatively wider companion in the Robo-AO field of view, we find the ($\sim 1''$) triple companion for CG Cyg is not detected by *Gaia*. However, considering the proximity to *Gaia*'s resolution limit as well as the rarity of chance alignments at these separations, we choose to leave its multiplicity designation unchanged.

3.4.2 Gaia Astrometric Candidates

Significant deviations from *Gaia*'s astrometric fit, manifesting as large values of the Astrometric Goodness of Fit in the Along-Scan direction (GOF_AL) and the significance of the Astrometric

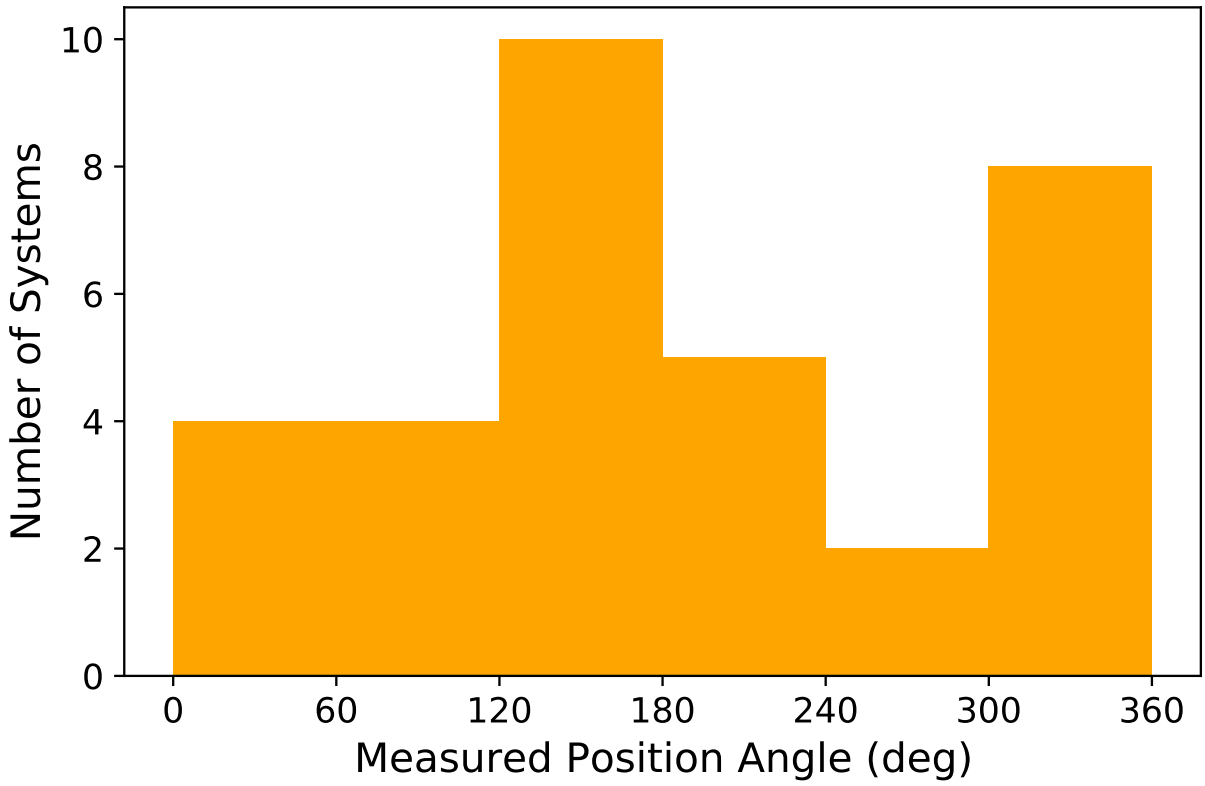

Figure 3.3: Distribution of measured position angles from Robo-AO PSF-subtracted image residuals.

Excess Noise (D), hint at the presence of unresolved companions. In particular, Evans (2018) finds a cutoff of GOF_AL > 20 and D > 5 to best separate confirmed binaries from confirmed singles. To confirm the source of the astrometric noise, we explore its dependence as a function of inner binary separation using the slightly relaxed criterion of GOF_AL > 15 and D > 3.

As we show in Figure 3.4, Gaia does not register significant astrometric noise (threshold marked by the dotted line) for the majority of our Robo-AO SBs, which typically have inner binary separations $\lesssim$ 1.5 mas (left of dashed line). For those that do register astrometric noise in this regime, we find all (10) systems also have a candidate companion identified in our Robo-AO imaging. We conclude that systems whose central SBs are tighter than $\sim$1.5 mas are not noticed as multiples by *Gaia*, unless they also possess a wider tertiary.

In contrast, we find the vast majority (12/14) of our wider SBs ($\gtrsim$1.5 mas, right of dashed line) register significant astrometric noise values (above dotted line), even if they do not possess an identified tertiary companion. In this regime, *Gaia* is likely detecting the photocenter motion of the relatively wide SBs, regardless of whether there is a wider tertiary.

A similar analysis for our Robo-AO KOI EB sample also confirms our tertiary designations. The sole exception is KOI 6016, for which *Gaia* identifies significantly high values of GOF_AL $=$ 166 and D $= 2095$. Assuming a total binary mass of 2 $M_{\odot}$, we estimate the angular separation of the EB (0.677 mas) to be much smaller than its measured astrometric excess noise (2.38 mas), thus we argue its source is an unresolved tertiary companion. We change its designation from binary to tertiary.

3.4.3 Washington Double Star Catalog Comparison

In this section, we carefully compare our observations to those listed in the WDS catalog. We find 8 of our Robo-AO SB targets have entries and describe them individually below.

2MASS J11480818+0138132 The most recent companion identification listed in WDS entry 11482+0136 refers to observations in 2015 by the Garraf Astronomical Observatory (OAG). Its

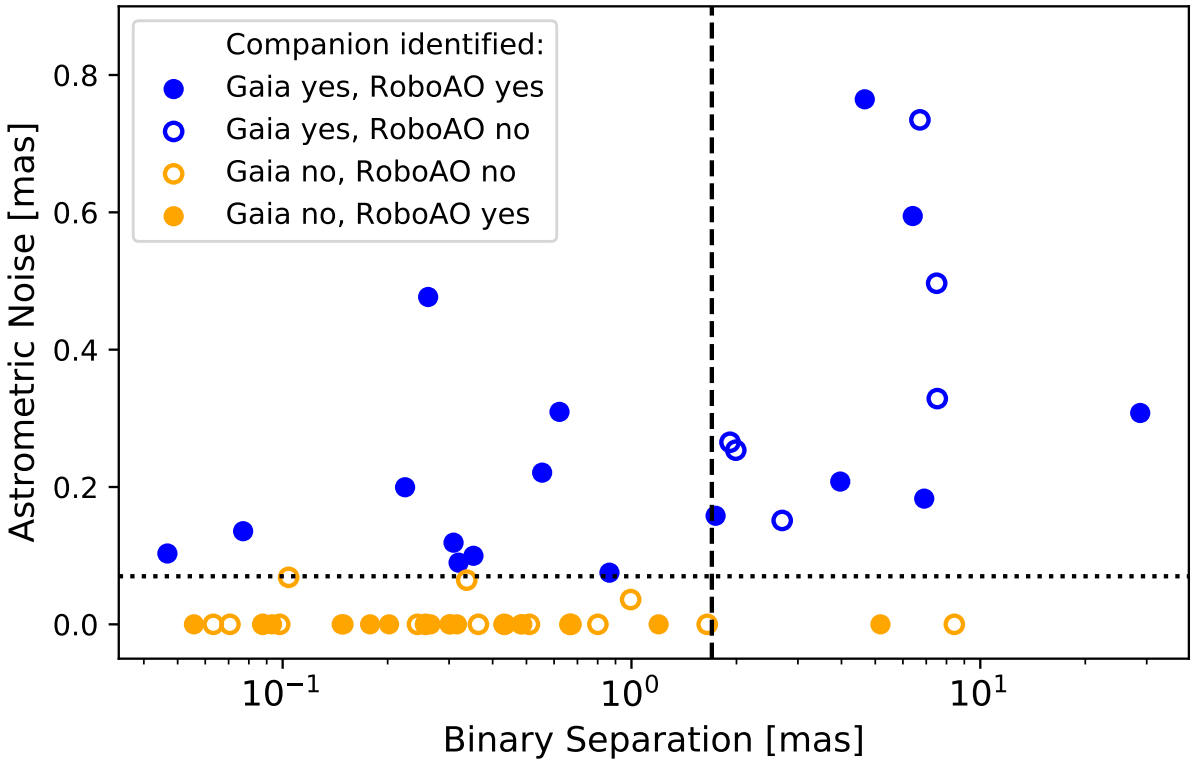

Figure 3.4: Gaia recorded astrometric noise for our Robo-AO SBs as a function of inner binary separation. Systems that (do not) pass our Gaia astromeric criterion (GOF_AL $>$ 15 and D $>$ 3) are shown in blue (orange). Filled (unfilled) dots correspond to cases where our Robo-AO imaging (did not) identified a candidate companion within 3.5″. The dotted line denotes the minimum astromtric noise observed for systems which pass our astrometric criterion. The dashed line separates our tighter (left) and wider (right) Robo-AO SBs.

CPM wide pairs (WP) survey identified[1] a $V\sim$11.1 companion at a separation of 119.″1 with a position angle of 334°. While this target is outside of the field of view of our Robo-AO imaging, our *Gaia* CPM analysis (see Section 3.1) also identifies this wide companion.

2MASS J12260547+2644385 WDS entry 12261+2645 refers to a singular speckle-interferometric observation that identified a $V\sim$9.7 companion at a separation of 1.″1 with a position angle (PA) of 167°(ASCC number 684901 in Guerrero et al. (2015)). Our Robo-AO observations find 2MASS J12260547+2644385 to be a candidate triple, with an upper limit separation of 1.″11 and a PA of 346°. Given our convention of measuring PA with respect to the SB (346°−180°=166°), we find these results to be in agreement and confirm this companion.

2MASS J16063131+2253008 The most recent companion identification listed in WDS entry 16065+2253 refers to Pan-STARRS observations from 2015 as detailed by Deacon et al. (2014). They report a companion separation of 35.″5 at a PA of 22°. The proposed source, 2MASS J16063229+2253337, is resolved by *Gaia* but faint ($G\sim$19.3). *Gaia* reports a parallax, R.A. proper motion, and Dec. proper motion of 11.734 ± 0.418 mas, −84.088± 0.538 mas/yr, and 90.03±0.571 mas/yr. In comparison, *Gaia* reports 11.601±0.075 mas, −88.263±0.105 mas/yr and 72.873±0.124 mas/yr for 2MASS J16063131+2253008. Given in particular the difference in Dec. proper motion, our *Gaia* CPM analysis does not find this pair to be associated.

2MASS J16074884+2305299 The most recent companion identification listed in WDS entry 16078+2306 refers to a 2004 observation (Alam et al., 2015) that identified a $V\sim$13.3 companion at a separation of 12.″2 with a position angle (PA) of 81°. A source at this separation does not fall into our Robo-AO field of view. *Gaia* resolves one other source within 15″, Gaia DR2 1206535963616734976, and reports a parallax, R.A. proper motion, and Dec. proper motion of 0.735±0.02 mas, 3.58±0.03 mas/yr, and −9.18±0.03 mas/yr. In comparison, *Gaia* reports

[1] The OAG CPMWP catalog can be found at https://www.oagarraf.net/Comunicacions/OAG%20CPM/GWP%20CATALOG%20EQUATORIAL%20ZONE%202016_ASCII__1.0.txt.

2.04±0.036 mas, −3.48±0.04 mas/yr and −9.38±0.05 mas/yr for 2MASS J16063131+2253008. These sources are clearly not physically associated.

V2368 Oph WDS entry 17162+0211 refers to a singular 1985 speckle-interferometric observation from the Center for High Angular Resolution Astronomy (CHARA) (McAlister et al., 1987). They reported a separation of 0.″136 at a PA of 69°. As detailed in the auxiliary WDS notes, the WDS entry was recalled after repeated attempts at confirmation by McAlister but later restored. While the most recent effort to confirm this companion (Roberts & Mason, 2018) was unsuccessful, our Robo-AO imaging suggests a companion at an upper limit separation of 0.″175 at a PA of 68°. Given the close agreement in separation and PA, we tentatively confirm this companion but encourage continued monitoring of this clearly complex case.

V624 Her The most recent companion identification listed in WDS entry 17443+1425 refers to a 2015 Gaia DR1 observation (Knapp & Nanson, 2018) that identified a $V\sim$11.75 companion at a separation of 40″with a position angle (PA) of 151°. *Gaia* DR 2 reports a parallax, R.A. proper motion, and Dec. proper motion of 7.1119 ± 0.0628 mas, −2.271± 0.098 mas/yr, and 15.134±0.096 mas/yr for V624 Her. In comparison, *Gaia* DR2 reports 0.7206±0.0457 mas, −0.446±0.074 mas/yr and −3.962±0.070 mas/yr for WDS 17443+1425B. These sources are clearly not physically associated.

V478 Cyg The most recent companion identification listed in WDS entry 20196+3820 refers to a 2015 listing in the Webb Deep-Sky Society's Double Star Section Circulars (DSSC)[2]. The listing, a 2006 observation from UKIDSS DR6 identifies a $V\sim$14.5 companion at a separation of 3.″61 with a position angle (PA) of 258°. A source at this separation does not fall into our Robo-AO field of view. *Gaia* resolves one other source within 5″of V478 Cyg but shows the pair to have discrepant parallaxes. We opt to retain our original identification.

[2] The DSSC catalog can be found at https://www.webbdeepsky.com/dssc/dssc23.pdf

CG Cyg The most recent companion identification listed in WDS entry 20582+3511 refers to two speckle-interferometric observations in 2014 that identified a $V\sim12$ companion at a separation of $1\farcs1$ with a position angle (PA) of 310°(Horch et al., 2015). Our Robo-AO observations suggest CG Cyg to be a triple, with a tertiary companion at an upper limit separation of $1\farcs16$ and a PA of 313°. Given the close agreement in separation and RA, we confirm this companion.

Given the faintness of the two wide companions we identified in Section 3.1 ($G\sim19$), it is not surprising the WDS catalog does not list entries for RT Crb or BK Peg. Similarly, the remaining 43 Robo-AO SBs do not have entries in the WDS catalog, likely a consequence of the difficulty of finding visual companions at the proximity of the (upper limit) separations of Robo-AO identified candidate companions ($\leq0\farcs25$).

3.5 Results

To summarize our analysis in Sections 3.3–3.4, out of our initial sample of 55 SBs, we obtain Robo-AO determinations in 52 cases. After our catalog search for additional CPM and astrometric candidate companions, we report a final tally of 20 binaries, 31 candidate triples, and 1 candidate quadruple system.

We begin by exploring the dependence of tertiary companion frequency on inner SB period for our Robo-AO SBs. Our 52 systems are sorted into SB period bins, with bin edges of 0, 3, 6, and 30 days (Figure 3.5, orange). Systems with periods greater than 30 d are grouped together (rightmost point). We find a trend of increasing incidence of tertiary companions toward shorter period SBs (orange points), with 90% of ($3^d < P_{\rm bin} < 6^d$) SBs having a tertiary companion compared to $\sim$47% of the longest period ($P_{\rm bin} > 30^d$) SBs. In the shortest period bin ($P_{\rm bin} < 3^d$), we find a slightly decreased fraction of 75% relative to the next bin ($3^d < P_{\rm bin} < 6^d$). We report the resultant tertiary fraction we derive for each period bin with its error in Table 3.4.

To compare with the canonical trend originally reported by Tokovinin et al. (2006), in Figure 3.5 we represent the Tokovinin et al. (2006) tertiary fractions with a simple exponential (note

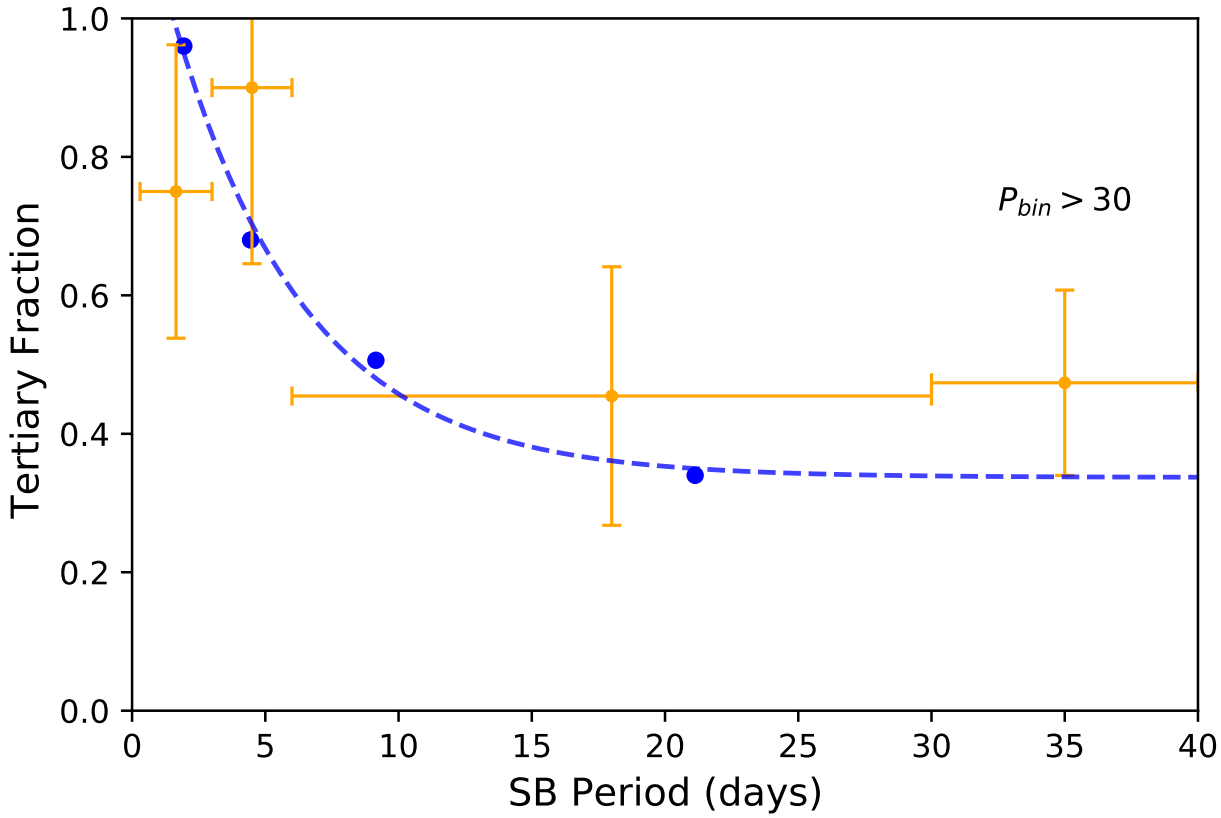

Figure 3.5: Fraction of SB systems with a candidate tertiary companion as a function of binary period (orange). The final bin represents all SBs with $P_{\rm bin} > 30^d$. In blue, we overplot the tertiary fractions found in Tokovinin et al. (2006), fit with a decaying exponential. Individual error bars correspond to the adjusted Poisson error for a multinomial distribution.

that this is not intended to represent a physical model). The tertiary fractions that we observe as a function of inner binary period are broadly consistent with the Tokovinin et al. (2006) result. We find this trend also extends to binary periods of $P_{\rm bin} > 30^d$, which are even longer than those considered by Tokovinin et al. (2006).

Next, as outlined in Section 2.1, we use the KOI EBs observed by Robo-AO as an additional, independent test sample of this trend. These systems had their PSF-subtracted images analyzed to look for stars within 4" of the central target (references in Section 2.1). Our *Gaia* analysis (Section 3.1) rules out the wider ($\gtrsim$2-3$''$) identified candidate companions. Candidate companions within $\sim$1$''$of the targets are considered to be likely physically associated. The resulting tertiary fractions as a function of SB period are shown in Figure 3.6 and again reported with errors in Table 3.4.

Table 3.4: Derived Tertiary Fractions

Period Bin	N	f
Robo-AO SBs		
$P_1 < 3$	12	0.75 ± 0.21
$3 < P_1 < 6$	10	0.9 ± 0.25
$6 < P_1 < 30$	11	0.45 ± 0.19
$P_1 > 30$	19	0.47 ± 0.14
Robo-AO KOI EBs		
$P_1 < 3$	5	0.96 ± 0.4
$3 < P_1 < 6$	3	0.68 ± 0.47
$6 < P_1 < 30$	8	0.51 ± 0.18
$P_1 > 30$	6	0.34 ± 0.24

Although there are only 10 KOI tertiaries among the SBs with $P_{\rm bin} < 30^d$, we find general agreement between our Robo-AO results (Figure 3.5) and the KOI EB sample Figure 3.6. We again find a systematically higher fraction of tertiary companions with shorter period SBs, with both trends clearly consistent with the findings of Tokovinin et al. (2006). We again note this trend also seems to extend to binary periods of $P_{\rm bin} > 30^d$.

3.6 Discussion

3.6.1 Tertiary-to-Binary Orbital Period Ratios

The increasing number of known multiples with well-defined orbital periods has lead to a thorough probing of the distribution of tertiary orbital period as a function of inner binary period. In Figure 3.7, the large sample of known triples from the updated Multiple Star Catalog (MSC) (Tokovinin, 2018) (grey crosses) and the smaller sample of triples from the volume-limited Raghavan et al. (2010) sample (black crosses) clearly indicate the wide range of permitted tertiary-binary period ratios. However, as noted in both Tokovinin (2014a) and Tokovinin (2018), the rarity of systems with small period ratios (< 10), and in particular short tertiary periods ($P_3 < 10$ yr), is evident from the lack of points along the dynamical stability limit $P_3 = 4.7P_1$ (solid line; Mardling & Aarseth, 2001 in the lower left corner.

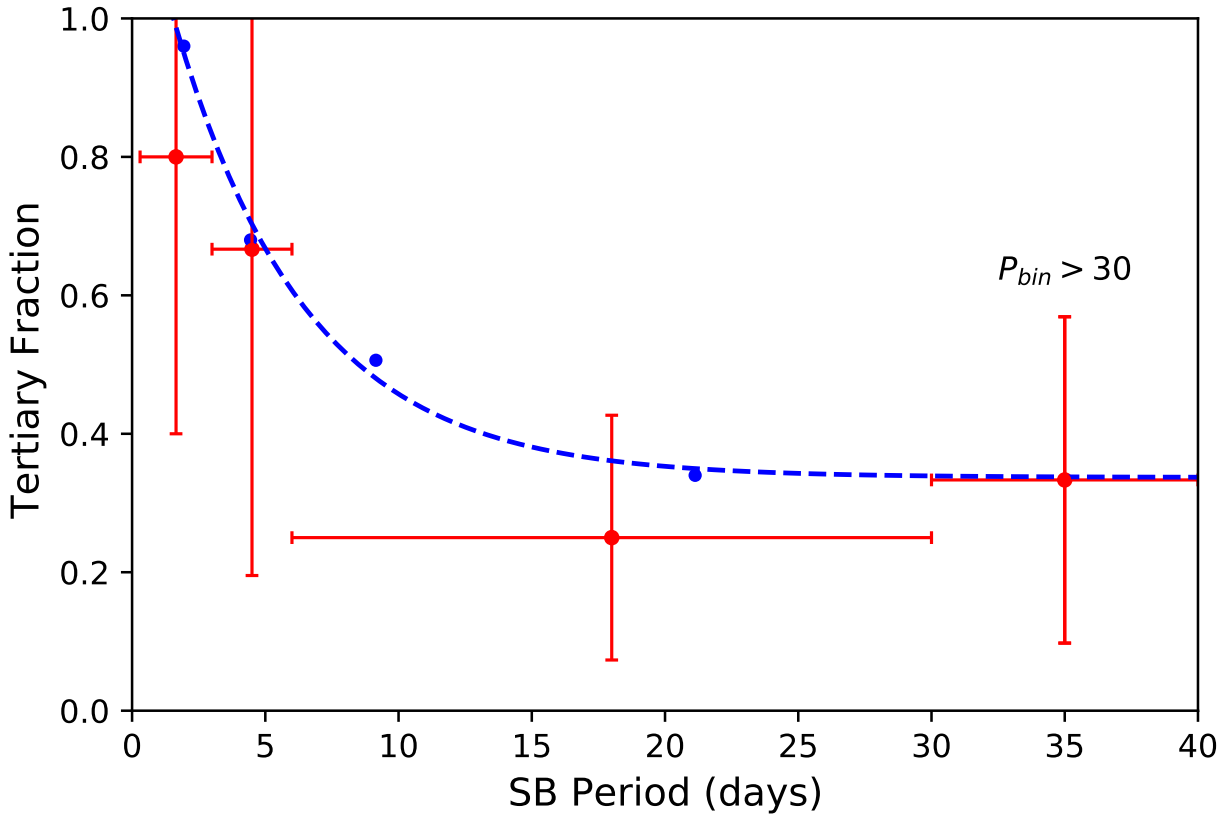

Figure 3.6: Same as Figure 3.5, but for KOI EBs observed by Robo-AO (red). The final bin represents all SBs with $P_{\rm bin} > 30^d$.

In an effort to explore a potential correlation with age, we refer to the benchmark PMS EB sample (Stassun et al., 2014), of which 7 of the 13 are identified with or have evidence of a tertiary companion. Three of these systems (RS Cha, TY CrA, and MML 53; Woollands et al., 2013; Corporon et al., 1996; Gómez Maqueo Chew et al., 2019) have tertiaries with orbital solutions; their ages range from 3–15 Myr. A literature search for additional PMS tertiaries also reveals orbital solutions for V1200 Cen (Coronado et al., 2015), GW Ori (Czekala et al., 2017), TWA 3A (Kellogg et al., 2017), V807 Tau (Schaefer et al., 2012), as well as TIC 167692429 and TIC 220397947 (Borkovits et al., 2020).

The tendency for these PMS systems to lie at low tertiary-binary period ratios is evident in Figure 3.7. To probe the potential significance of this apparent difference relative to the older field population, we perform a two-dimensional, two-sided KS test between the PMS sample and

the volume-limited Raghavan et al. (2010) sample, reporting a p-value $< 10^{-4}$. The difference is statistically significant, which corroborates the visual impression that indeed the PMS sample occupies a different distribution of tertiary-to-binary orbital periods than the field-age sample.

For our Robo-AO sample, we note the upper limits of our estimated tertiary periods (red and yellow arrows in Figure 3.7) are consistent with the larger field-age samples of Tokovinin (2018) and Raghavan et al. (2010).

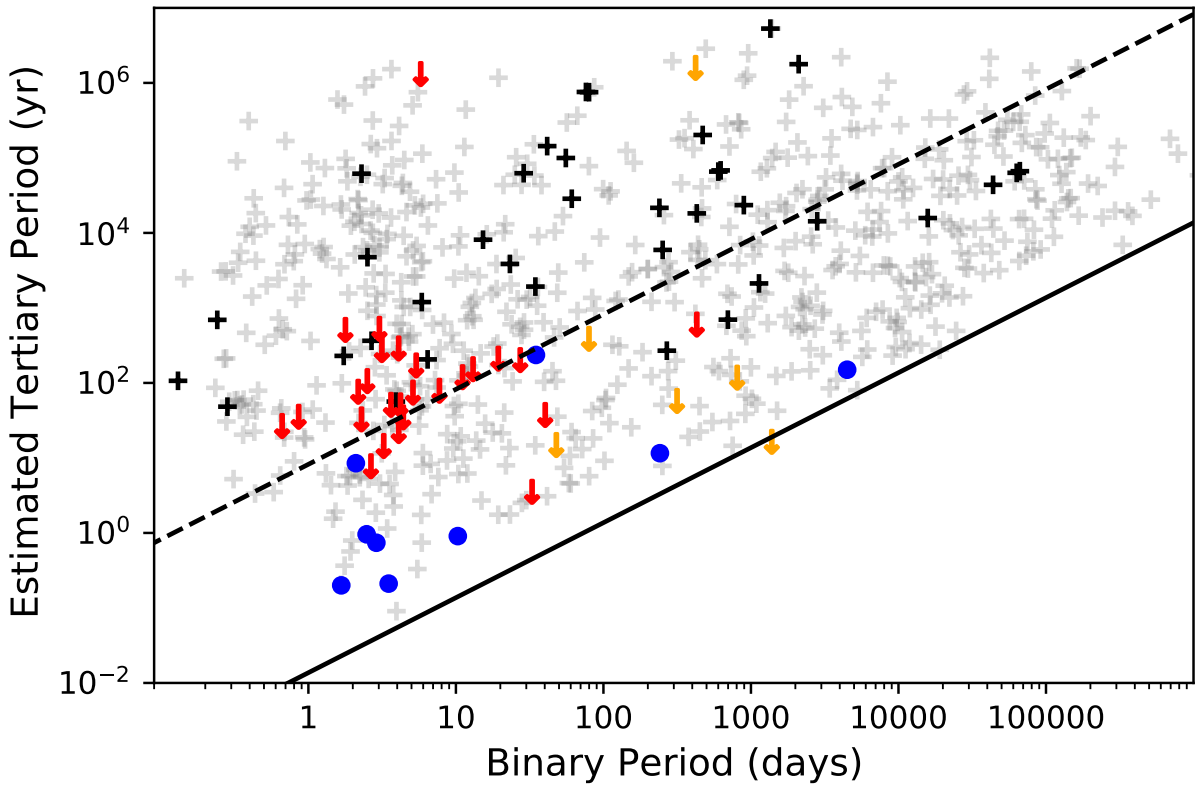

Figure 3.7: Estimated tertiary periods as a function of inner binary period. Identified Robo-AO candidate triples are marked as red (Torres et al., 2010) and orange (Troup et al., 2016) arrows, given our estimates are upper limits. For comparison, we plot the updated MSC triples (Tokovinin, 2018) as grey crosses while overplotting the triples from the volume-limited Raghavan et al. (2010) sample as black crosses. For reference, the dashed line represents $P_3 = 10^{3.5} P_1$. The dynamical stability limit for triples ($P_3 = 4.7 P_1$) is shown by the full line. Known PMS ($\lesssim$30 Myr) triples are shown in blue.

3.6.2 Hierarchical Unfolding

Although tertiary-induced inner binary period shortening is evident, there is growing evidence that a single mechanism, such as Lidov-Kozai cycles with tidal friction (KCTF), cannot recreate the entire population of known close binaries (e.g., Kounkel et al., 2019; Bate, 2019). As has already been shown for individual cases (e.g., Gómez Maqueo Chew et al., 2019), we find that many of the well-characterized EBs in young (<30 Myr) triple systems have already achieved close separations ($\lesssim$0.1 AU). Evolution by the KCTF mechanism, which has an effective timescale on the order of $\sim$100 Myr, is unable to account for these (<30 Myr) systems.

The alternative mechanism of hierarchical unfolding (e.g., Reipurth & Mikkola, 2012), in which the orbit of a newly bound wide (100–1000 AU) binary is shrunk by ejecting a third body into a distant orbit, is unable to achieve the close separation of a spectroscopic binary alone. However, because these interactions often result in a highly eccentric orbit for the binary, the additional dissipative interactions with the primordial gas expected in the disks of these young binaries also aid in the observed orbital decay. Recent population synthesis work (Moe & Kratter, 2018) finds that $\sim$60% of close binaries ($P_{\rm bin} < 10^d$) form during the PMS phase and in a compact configuration with a tertiary companion as a consequence of this process.

Known PMS triples with estimated orbits are notably compact and weakly-hierarchical, with significantly smaller tertiary-to-binary period ratios than the majority of known triples in the field (see Figure 3.7). The majority of our Robo-AO candidate triples with known ages (12/15) are field-age ($\sim$1 Gyr) systems, and have thus had sufficient time to dynamically evolve. In comparison to the PMS systems, they all lie in the cluster of points with upper limit period ratios of $10^{3.5}$ or greater. Although it is not feasible to reconstruct the dynamical pathway taken by each system, as both hierarchical unfolding and KCTF are able to account for the current orbital configurations, their hierarchical nature is evident, with a range of hardened inner binaries ($P_{\rm bin} < 30^d$) and large tertiary-to-binary period ratios ($\geq 10^{3.5}$).

This apparent difference between the field-age and PMS sample could be equally explained from the standpoint of the tertiary companion or the inner binary. The simulations of Reipurth

& Mikkola (2012) find the most extreme wide systems take on the order of $\sim$100 Myr to fully unfold and thus it is possible some of the tertiaries in these PMS systems still have significant dynamical evolution to undergo. Alternatively, if the reservoir of primordial circumstellar disk gas is not yet exhausted, it is possible some of our PMS binaries are still in the process of hardening if young enough. Thus, the conditions for evolution via hierarchical unfolding with dissipative gas interactions appear to be in place for the youngest systems.

Another question is whether the dynamical evolution of triple systems leads to tertiaries that are wider than would be expected to arise from the formation process alone. Tokovinin (2014b) argued that overall distributions of inner and outer orbital periods in multiple-star systems is consistent with dynamical sculpting that produces inner binaries populating the short-period part of the overall distribution and outer companions populating the long-period part of the overall distribution. But is there evidence that tertiaries come to reach wider separations than the widest binaries? To this end, we compare the period distributions of simple binaries versus triples within the volume-limited Raghavan et al. (2010) and Tokovinin (2014a) samples (Figure 3.8).

The upper bound of the appropriate period range for the comparison considers the longest period for which both binaries and tertiaries are observed ($\sim 10^7$ years). Because inner binaries of triple systems cannot be as wide as their tertiaries, we do not extend the lower bound to the period for which the tightest tertiaries are observed (10 years); instead, we consider the longest period binaries in the triples identified in the larger volume-limited sample of Tokovinin (2014a). We choose a generous lower bound of 10^3 years, with only a small number of binaries (identified through CPM) exceeding this period.

Within this period range ($10^3 < P < 10^7$ years), we perform a two-sample Anderson-Darling test on the lone Tokovinin binaries versus tertiaries (dotted distributions in Fig. 3.8) to probe the differences in the tails of these distributions. We do not find strong evidence (p-value $= 0.06$) that tertiary companions find themselves at wider separations than their simple binary counterparts. We find a similar result when considering the Raghavan sample (solid distributions in Fig. 3.8). There is therefore not strong evidence to suggest that the mechanisms governing the underlying popu-

lations of the widest binaries and tertiaries are distinct, consistent with the findings of Tokovinin (2014b).

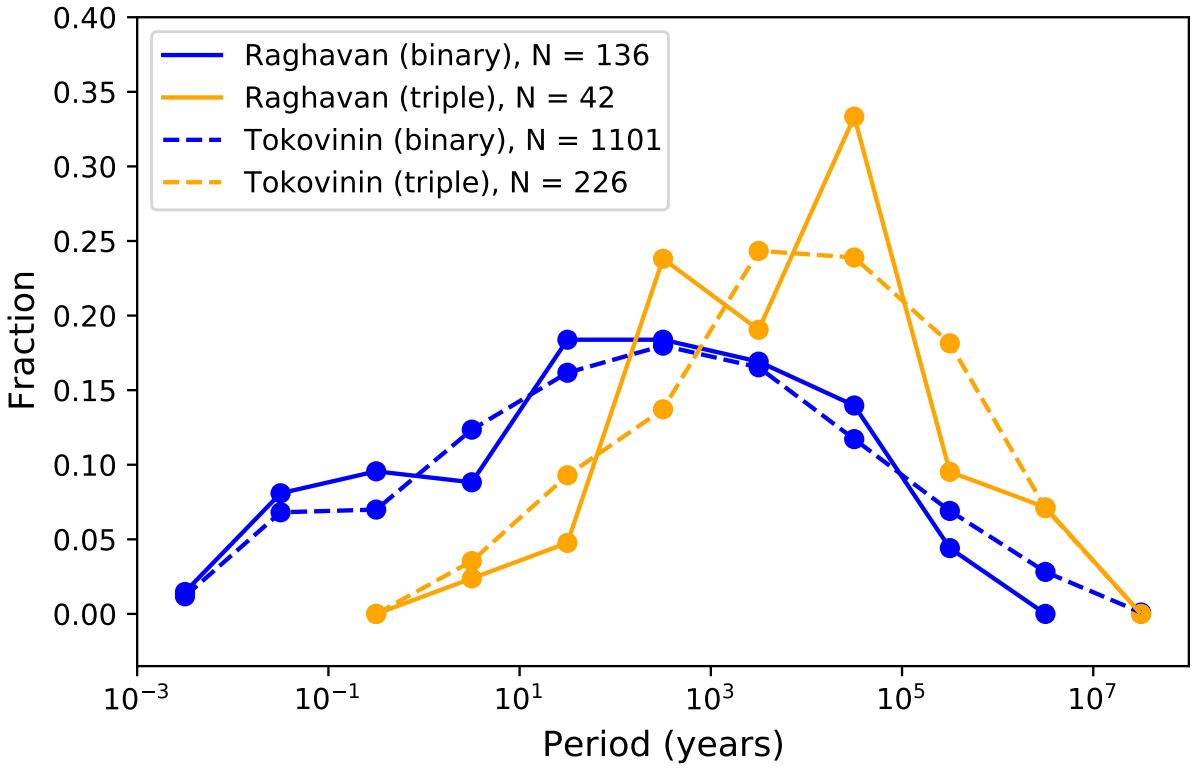

Figure 3.8: Distribution of orbital periods between the lone binaries (blue) and tertiaries (orange) from the volume-limited Raghavan et al. (2010) (solid) and Tokovinin (2014a) (dashed) samples.

3.7 Summary

In this paper, we have conducted robotic adaptive optics (Robo-AO) imaging for a sample of 60 spectroscopic binaries (SBs) with known periods and distances. For 52 individual sources, we identify candidate companions, or lack thereof, through a visual inspection of their PSF subtracted images and search for additional candidates using *Gaia* parallaxes, proper motion, and astrometric information. Overall, we identify 31 candidate tertiary systems and 1 candidate quadruple systems.

A principal aim of this paper was to test the reproducibility of the canonical result from Tokovinin et al. (2006), namely that tertiary frequency is a strong function of inner binary or-

bital period. For our Robo-AO candidate tertiaries, we find higher fractions of tertiary companions around shorter period binaries, with 75% of $P_{\rm bin} < 3^d$ systems having a tertiary companion compared to $\sim$47% of the longest period ($P_{\rm bin} > 30^d$) systems, consistent with the findings of Tokovinin et al. (2006) and extending that result to even longer-period inner binaries. A separate test sample of the smaller number of Robo-AO observed KOI EBs also shows this trend. The two samples, thus, appear to independently reproduce the canonical result of Tokovinin et al. (2006).

We have roughly estimated the tertiary period for each of our candidate triples, exploring the dependence of their distributions on inner SB period and age. Although we are unable to determine the prominent mechanism at work for their dynamical evolution, we note all of our field-age Robo-AO systems find themselves in hierarchical configurations, with large ($P_3/P_1 > 10^{3.5}$) tertiary-binary period ratio upper limits. In comparison, we find known young PMS triples are much more compact in comparison, with the conditions for hierarchical unfolding (e.g., Reipurth & Mikkola, 2012) already in place. We find these results to be consistent with the recent population synthesis predictions of Moe & Kratter (2018).

Taken together, the results of this investigation can be interpreted through a framework in which stellar triples evolve from relatively compact configurations to increasingly hierarchical configurations, in which the hardest binaries arise almost exclusively through tertiary interactions, and in which the widest tertiaries arise through interactions with their inner binaries.

3.8 Appendix: Mosaic of Point Spread Function Subtracted RoboAO Images

To display the companions identified from our RoboAO imaging, we first show a mosaic of our pre-PSF-subtracted images for each SB system, followed by a mosaic of our PSF-subtracted images with visual aids pointing to residual features that indicate image distortions suggestive of companions; these features are PSF residuals and do not represent resolved detections of the putative companions (see Section 3.3.2). Additional vetting of companions via *Gaia* astrometry and previous observations is described in Section 3.4.

Table 3.5: Robo-AO Non-SB Observations

Name	R.A. (deg.)	Dec. (deg.)	V (mag)	Strehl Ratio (%)	Multiplicity Flag[a]
2MASS J05130342+2423489	78.264217899	24.396841655	6.707	2.06	T
2MASS J08140761+3145095[b]	123.531723248	31.752562931	12.44	6.52	
2MASS J08145689+3208572	123.736957886	32.149168567	8.3	4.51	B
2MASS J09303285+2735099	142.636911616	27.585936424	10.722	3.56	N
2MASS J10404394+2348227	160.18296347	23.806274661	10.382	2.3	N
2MASS J11040722+4415409	166.029847747	44.261378235	9.685	3.66	B

The full table is available in the electronic version of the Journal. A portion is shown here for guidance regarding its form and content.

[a] Multiplicity flag: B = binary, T = candidate triple, N = no companion detected.

[b] Faint systems that were not reduced properly (see Section 2.1) (no companion information could be deduced from RoboAO imaging.)

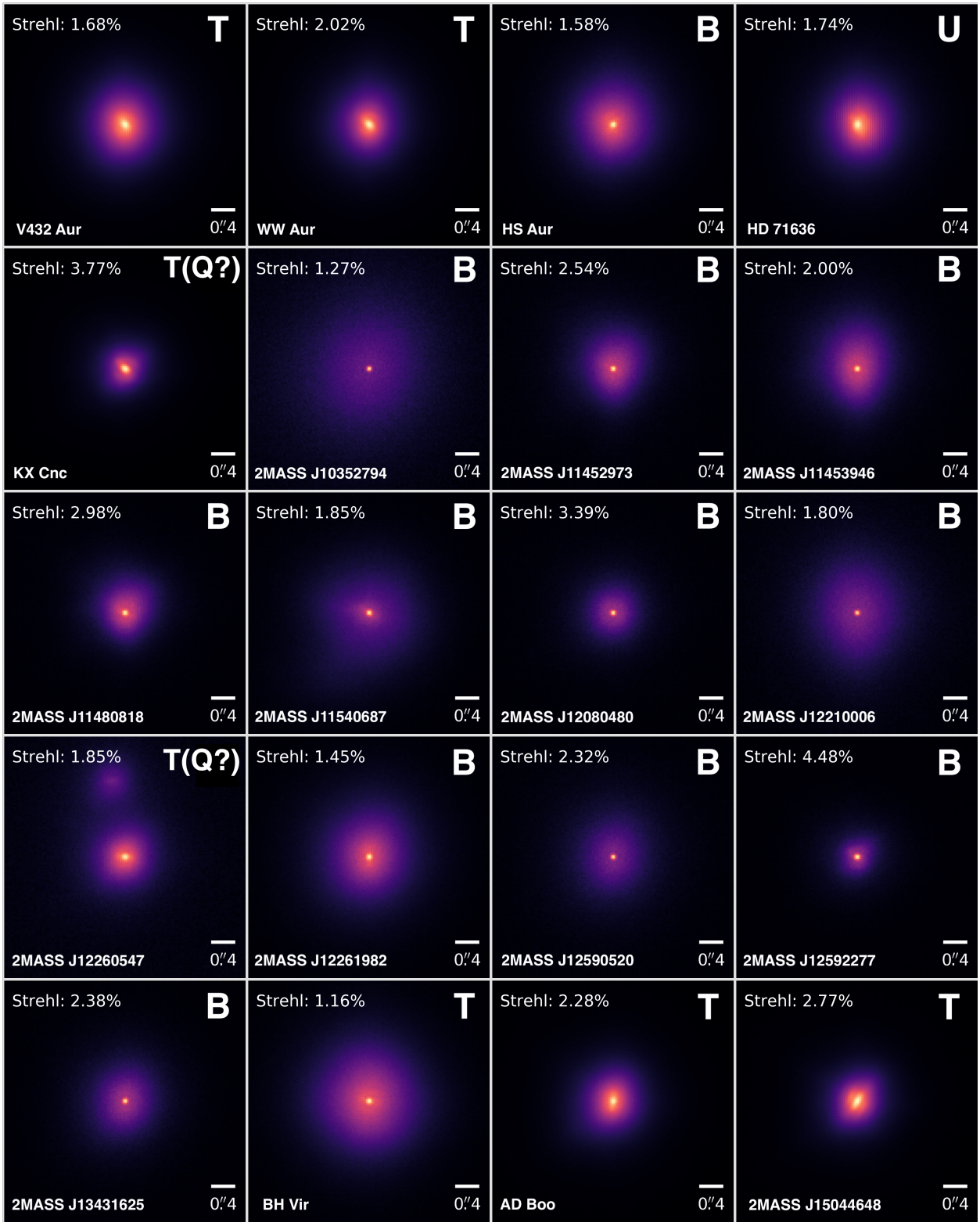

Figure 3.9: Pre-PSF-subtracted images for RoboAO SBs (continued in Figure 3.10 and Figure 3.11). We note the designation in the top right corner of each image corresponds to that determined strictly by our RoboAO imaging and thus does not include the results of our wide companion identifications in Section 3.4. Our final identifications are that listed in Table 3.1.

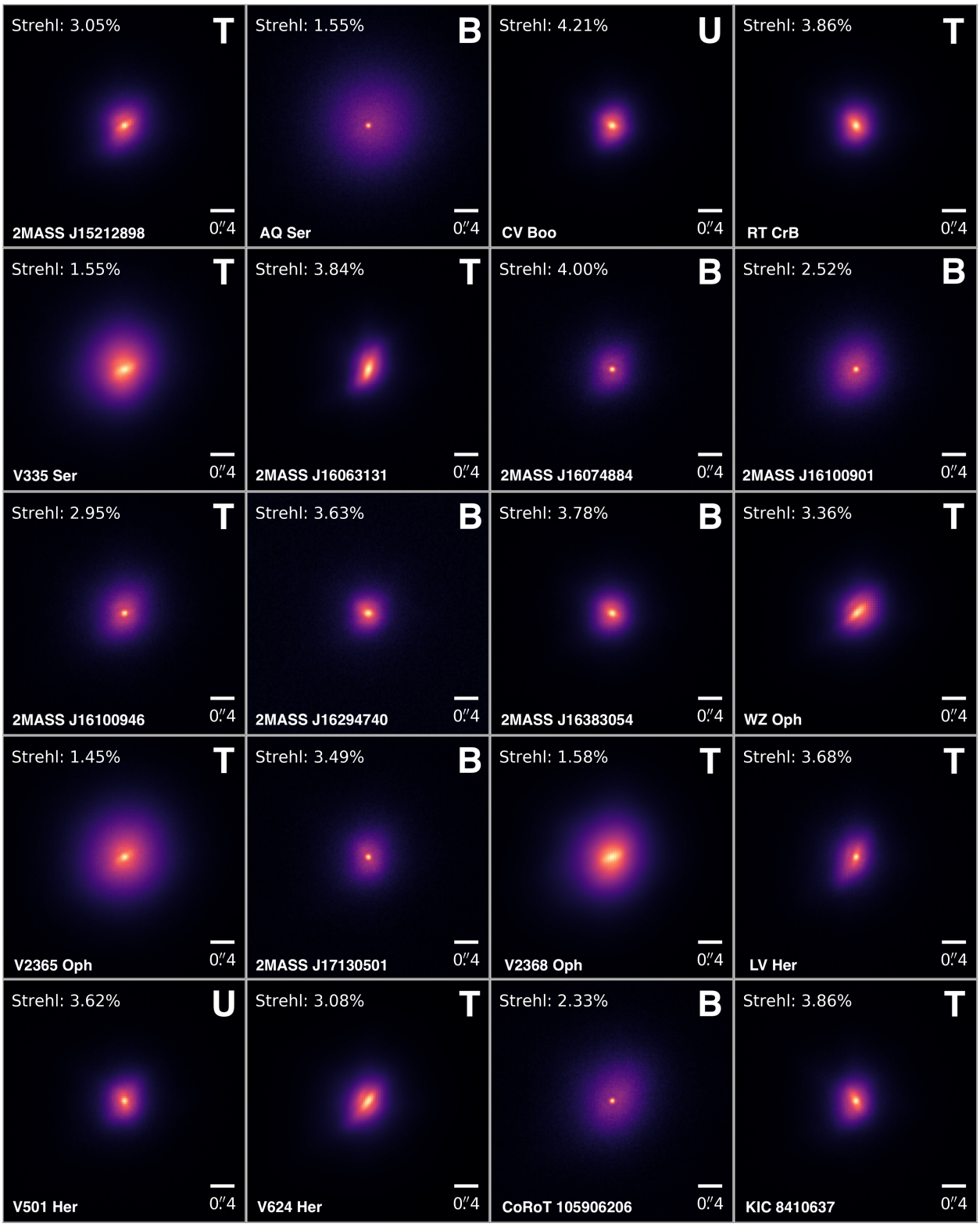

Figure 3.10: Pre-PSF-subtracted images for RoboAO SBs (continued from Figure 3.9). We note the designation in the top right corner of each image corresponds to that determined strictly by our RoboAO imaging and thus does not include the results of our wide companion identifications in Section 3.4. Our final identifications are that listed in Table 3.1.

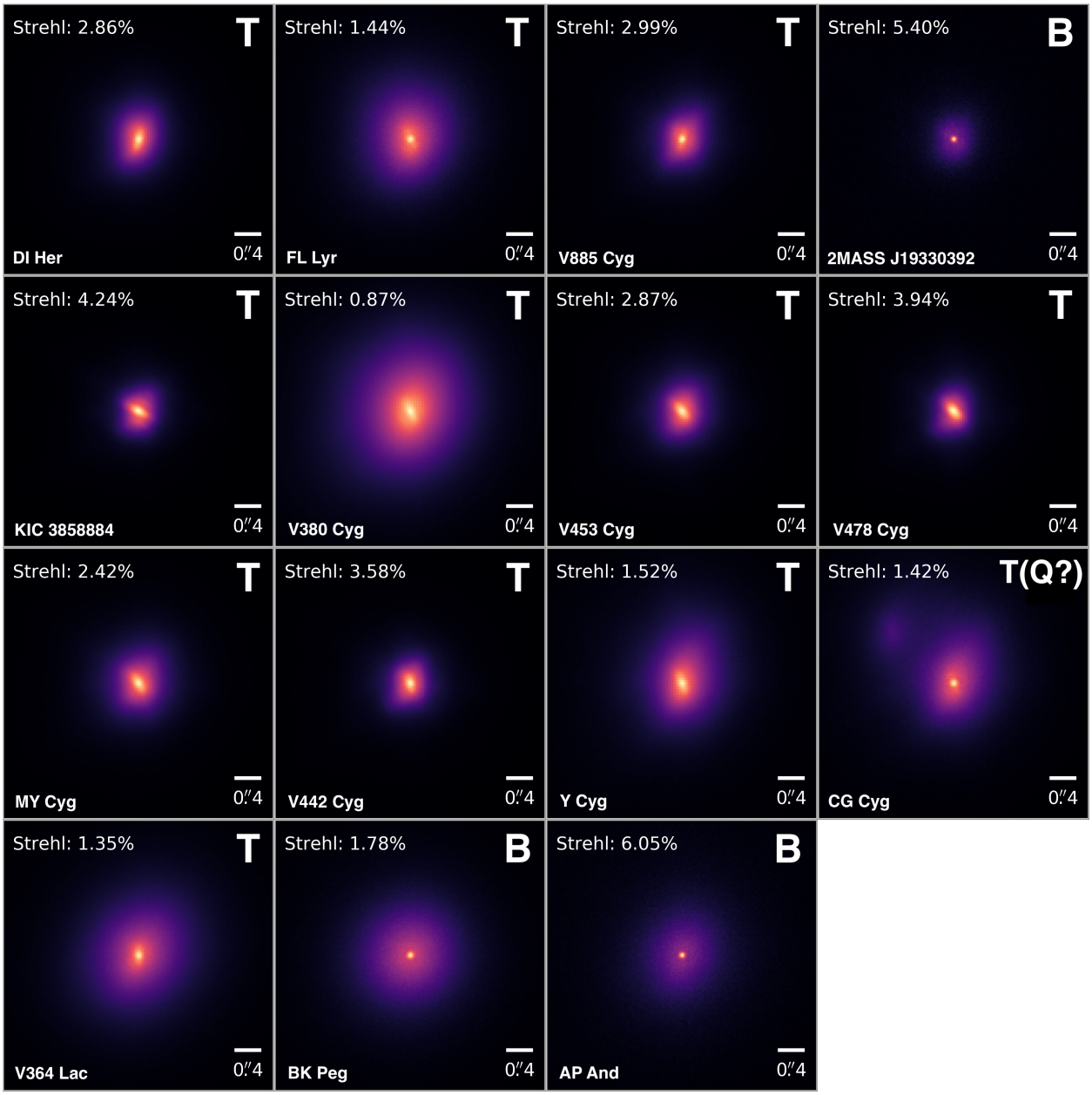

Figure 3.11: Pre-PSF-subtracted images for RoboAO SBs (continued from Figure 3.10). We note the designation in the top right corner of each image corresponds to that determined strictly by our RoboAO imaging and thus does not include the results of our wide companion identifications in Section 3.4. Our final identifications are that listed in Table 3.1.

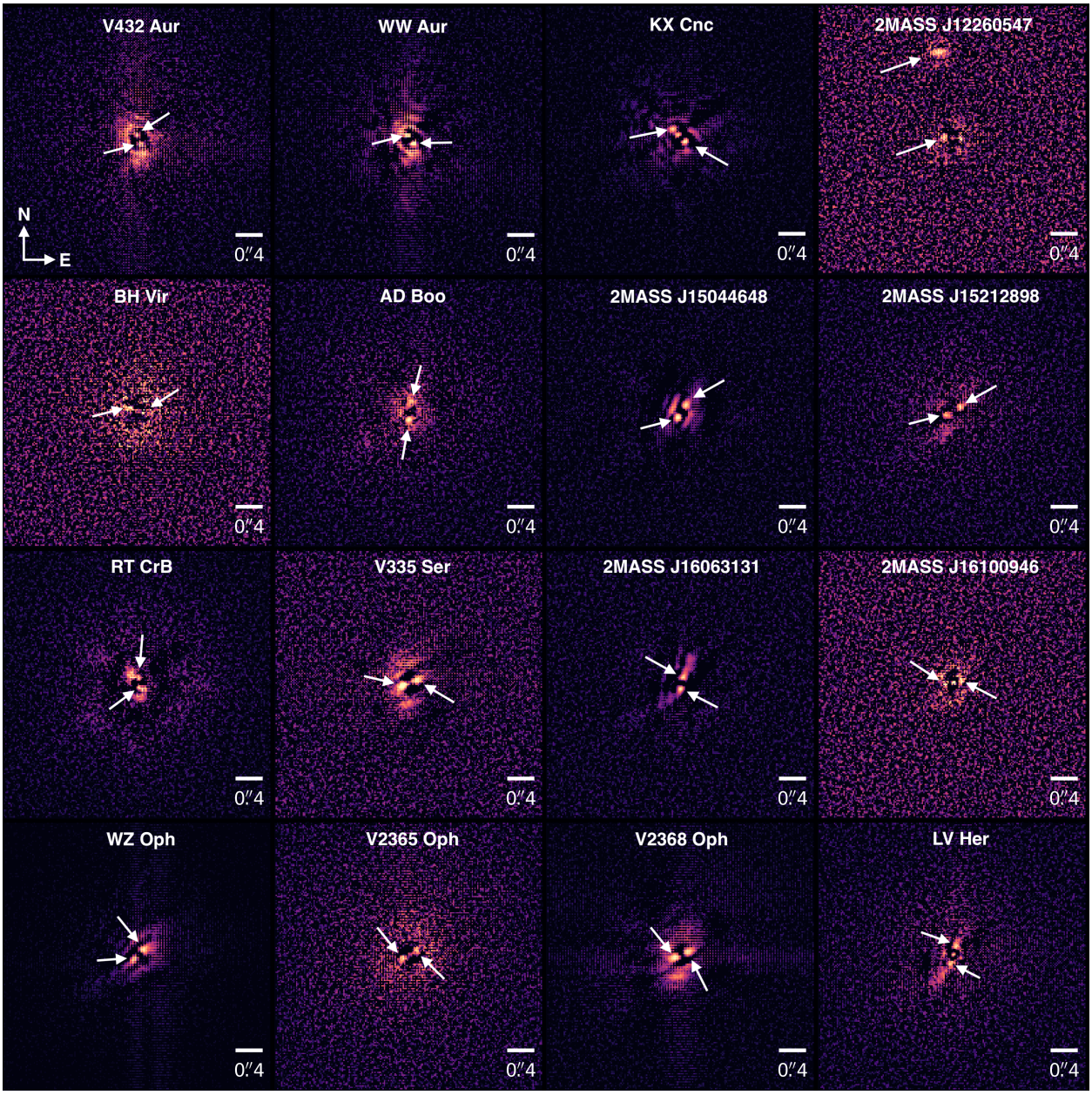

Figure 3.12: PSF-subtracted images for RoboAO identified candidate multiples (continued in Figure 3.13). Visual aids point to residual features that indicate image distortions suggestive of companions; these features are PSF residuals and do not represent resolved detections of the putative companions (see Section 3.3.2). Additional vetting of companions via *Gaia* astrometry and previous observations is described in Section 3.4.

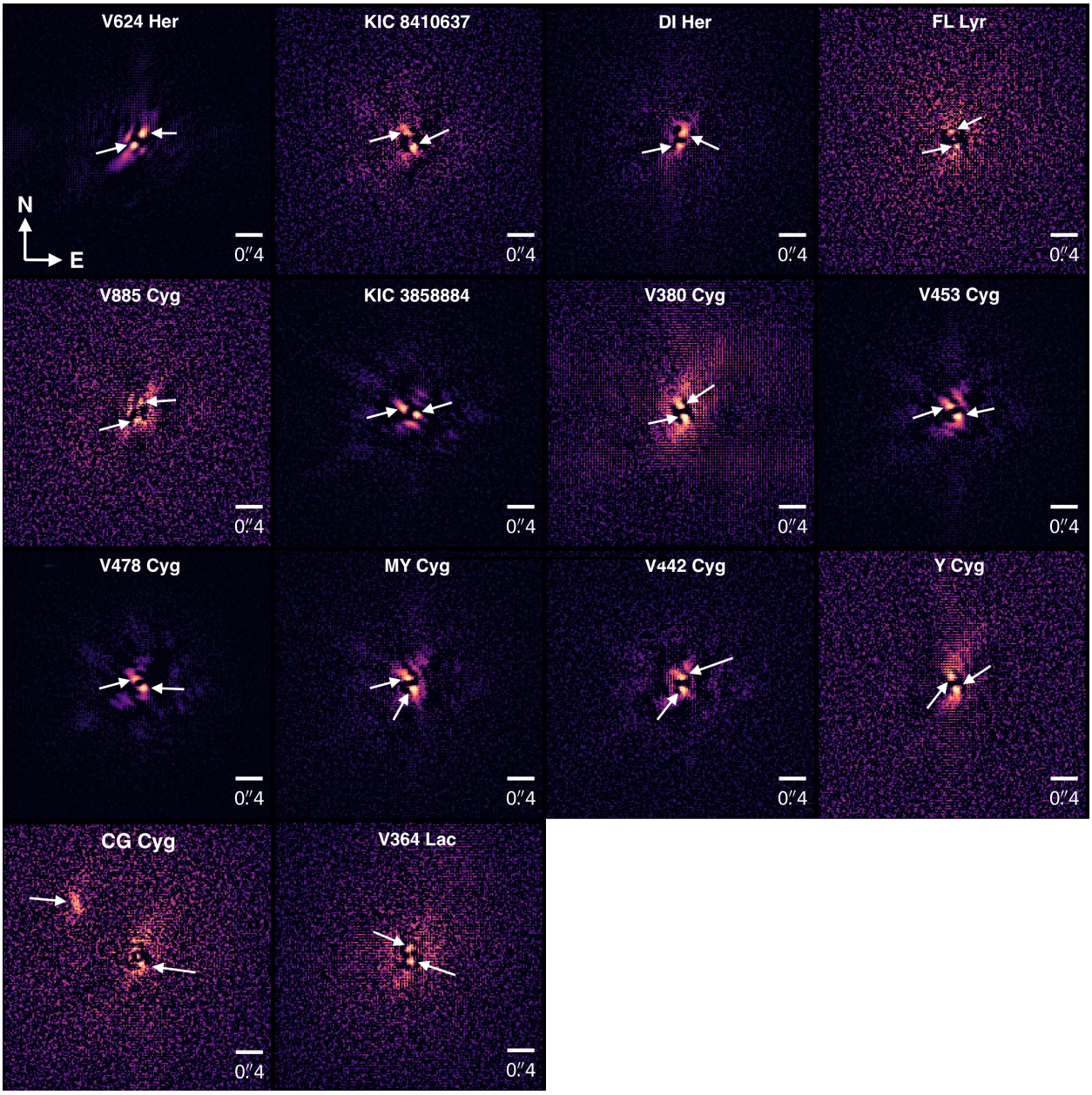

Figure 3.13: PSF-subtracted images for RoboAO identified candidate multiples (continued from Figure 3.12). Visual aids point to residual features that indicate image distortions suggestive of companions; these features are PSF residuals and do not represent resolved detections of the putative companions (see Section 3.3.2). Additional vetting of companions via *Gaia* astrometry and previous observations is described in Section 3.4.

Chapter 4

Conclusions and Future Work

4.1 Conclusions

Overall, there has been growing progress in the astrophysical literature towards the characterization of young stellar evolution phenomenon. The use of sensitive, near-infrared observations continues to unravel these mysteries, with this work providing insight into the short, active periods during stellar formation and early binary dynamics. In Chapter 2, we analyzed our K-band spectroscopy of Class 0 protostars taken by the Keck I MOSFIRE instrument. This data revealed the properties of their near-stellar environment, finding clear signatures of active disk accretion in the form of CO overtone emission. In particular, we found evidence for the presence of an established magnetosphere in Class 0s (the earliest observable stage of young stellar evolution) from our observed Brackett γ line profiles.

In Chapter 3, we analyzed adaptive optics near-infrared imaging data of spectroscopic binaries (SBs) taken by the Robo-AO imaging system at the Kitt Peak National Observatory. With this high-contrast data, we searched for nearby companions in our field of view and found image distortions from our PSF-subtracted images that were suggestive of companions. When comparing our incidence rate of suggested tertiary companions with the orbital period of the observed SB, we found $\sim$90% of our short period ($\lesssim 5^d$) SBs had suggested companions as opposed to only $\sim$47% in our long period ($\gtrsim 30^d$) SBs. This result provides further evidence for the relation originally found by Tokovinin et al. 2006; shorter period SBs are systematically more likely to be in a higher order system than longer period SBs. Collectively, our findings support the mechanisms of angular momentum transfer from three-body interactions during early evolution, ultimately resulting in tight binaries with tertiaries that widen from pre-main-sequence to field ages. We briefly discuss future work and ideas in the next section.

4.2 Future Work

4.2.1 Near-IR Spectroscopic Observations of Class 0 Protostars

Our results in Laos et al. 2021 (in prep., submitted to ApJ) are beginning to see the diversity of observed near-IR emission features among Class 0s. Additional spectroscopic observations of Class 0s are needed to characterize the underlying Class 0 population beyond our small initial sample of 7 objects and discern the significance of our emission incidence statistics. Promising (i.e. satisfying our selection criteria, Section 2.3) targets from the Southern Hemisphere could potentially serve as a future sample for study.

The near-IR spectroscopic observations in Laos et al. 2021 were of moderate spectral resolution (our effective resolving power was $\sim$1700-2400 depending on the spatial extent of our Class 0s, Table 2.1). As noted in Section 2.4.1, the limited velocity resolution of our data precluded our ability to perform detailed spectral modeling of our observed CO bands. This analysis would have the potential to constrain properties of the Class 0 disk (T_{gas}, v $\sin i_{disk}$), given high S/N and spectral resolution observations (Najita et al. 1996a, Fedriani et al. 2020). Constraining the disk inclination could also help guide the model fitting to our Class 0 SEDs, resulting in greater confidence for our extinction estimates.

The main limitations of this proposal are observational logistics. As our most spatially compact (and relatively bright) Class 0 with prominent CO bands detected, HOPS 32 serves as our most promising candidate. We consider the observing constraints using the high-resolution (R$\sim$45000) spectrograph IGRINS located at the Gemini Observatory. The minimum S/N for producing science (30) would require $\sim$2.2 hours of total integration time for an ABBA quad on a point-source target as bright as HOPS 32 (K$\sim$15.3). The fact that HOPS 32 will be spatially extended at a value greater than the effective IGRINS slit width ($0.34''$) will decrease our S/N, ultimately requiring longer exposure times. Binning down our data by a factor of 4 would double our S/N and potentially still give us a high enough spectral resolution for this work (R$\sim$10000) while being logistically tractable (total integration time $<$5 hours). Overall, this would serve as the first high-resolution

spectrum taken of a Class 0 source.

To bolster a potential observing proposal for the 2022A semester, promising Class 1s with previously observed evidence of CO emission will need to be considered in addition to HOPS 32. Ideal candidates would have lower than average derived T_{bol}s, potentially indicating a slightly earlier evolutionary stage (i.e. a transitionary source between Class 0 and Class I). A lack of sufficient, reasonable targets may require the increased observing power of JWST to identify additional Class 0s feasible for sensitive, spectroscopic study.

4.2.2 Robotic Adaptive Optics Imaging Data of Spectroscopic Binaries

The final SB sample observed in Laos et al. 2020 (N = 60) was ultimately smaller than the original sample size of Tokovinin et al. 2006 (N = 165). A more robust statistical comparison will require a larger sample of SBs to observe. These future targets are already scheduled to be observed with the establishment of Robo-AO 2 at the University of Hawaii 2.2m telescope (expected in the 2021B and 2022A observing semesters). The improved seeing at this location (relative to the effective, average seeing at the Kitt Peak Observatory) will allow for more definitive companion identifications (compared to the observed image distortions only suggestive of companions in Laos et al. 2020).

A subset of these new targets will also include suspected younger SBs, with pre-main-sequence, as opposed to field, ages. Their observation will increase the low number of PMS SBs with known orbital parameter information given the measured distances from Gaia DR2. Systems with newly identified companions can have their hierarchical compactness compared relative to that of previously observed PMS and field multiples (Figure 3.7).

4.2.3 The Characterization of 3 New Pre-Main-Sequence Eclipsing Binaries Systems: Detailed Modeling with PHOEBE 2

Pre-main-sequence (PMS) stellar evolutionary models are indispensable to our understanding of stellar formation and early evolution. They shed light on the most fundamental mysteries of

star formation, including the nature and origin of the initial mass function, the initial distribution of stellar angular momentum, and the timescale for circumstellar disk evolution. Ensuring the accuracy of these models requires precise calibration by stringently testing against a benchmark sample. Eclipsing binaries (EBs) serve as the ideal candidates; through photometric and spectroscopic analysis, it is possible to rigorously derive their fundamental physical properties with few theoretical assumptions. Although successful for EBs with masses $\gtrsim$1, current stellar models struggle to constrain the low-mass regime of PMS EBs, predicting systematically higher effective temperatures and smaller radii than observations indicate (Stassun et al. 2014).

As part of the YSOVAR survey (Morales-Calderón et al. 2011), multi-wavelength light curve data has been acquired for three new PMS EBs in the Orion Nebula Cluster (J0535-0447, J0535-0522, and J0535-0523). These three systems have also been observed by the GNIRS near-infrared spectrograph on the Gemini Observatory. This data has already been partially reduced, with radial velocity (RV) curves extracted for a subset of this sample.

Once these data have been fully reduced, we will use the sophisticated EB orbit solver, PHOEBE 2, to add to the benchmark sample of PMS EBs, which have had their masses derived to an accuracy of $\sim$1%. The PHOEBE 2 workshop, attended in June 2019 and annually offered, has helped prepare me to use and optimize (support for MPI parallelization, the Python package EMcee) this modeling code, with advanced features that were not available in the PHOEBE legacy suite (accounting for star spots, third light, and limb-darkening). This work will also benefit greatly from the use of the sensitive light curves recently observed by the Transiting Exoplanet Survey Satellite (TESS).

4.2.4 Collaboration with the Long-term Spectroscopic Monitoring Program at Tennessee State University

A large sample of spectroscopic binaries have been monitored for over a decade by the 2m Automated Spectroscopic Telescope (AST) at the Fairborn Observatory. Headed by Dr. Michael Williamson, this Tennessee State University (TSU) program aims to publish full orbital solutions

for this sample. The data are well-catalogued and have data reduction, RV extraction, and orbital fitting pipelines already in place. Our Vanderbilt-TSU collaboration will work towards a full characterization of this large SB sample.

In addition to this bulk analysis, we have begun to identify interesting sub-populations within this larger sample for more detailed study. These populations include but are not limited to discovering SBs with additional suspected companions, derived ages, or particularly low mass (e.g. brown dwarf components) systems. With the machinery developed as part of Laos et al. 2020 (Section 3.4), we have now begun to search for potential tertiary companions to our individual SBs using *Gaia* DR2 parallaxes and proper motions.

Information from *Gaia* DR2 5D data set can also be used to derive age estimates for a fraction of our SB sample. Using unsupervised machine learning, Kounkel & Covey 2019 identified numerous local (within 1 kpc) clusters, associations, and co-moving groups (classified as "Theia" strings) and derived age estimates. From our collaboration with Dr. Kounkel, we have cross-matched the SB sample observed by the AST with known strings, finding a subset of SBs with high likelihood for membership. From this subset, we have determined a small handful of systems with young suspected ages ($\sim$20-30Myr). These rare systems are promising candidates for further observations and study.

BIBLIOGRAPHY

Alam, S., Albareti, F. D., Allende Prieto, C., et al. 2015, ApJS, 219, 12, doi: 10.1088/0067-0049/219/1/12

Andre, P., Ward-Thompson, D., & Barsony, M. 1993, ApJ, 406, 122, doi: 10.1086/172425

Antoniucci, S., Nisini, B., Giannini, T., & Lorenzetti, D. 2008, A&A, 479, 503, doi: 10.1051/0004-6361:20077468

Arce, H. G., & Goodman, A. A. 2001, ApJ, 554, 132, doi: 10.1086/321334

Aspin, C., Reipurth, B., Herczeg, G. J., & Capak, P. 2010, ApJ, 719, L50, doi: 10.1088/2041-8205/719/1/L50

Baranec, C., Ziegler, C., Law, N. M., et al. 2016, AJ, 152, 18, doi: 10.3847/0004-6256/152/1/18

Bate, M. R. 2019, Monthly Notices of the Royal Astronomical Society, 484, 2341, doi: 10.1093/mnras/stz103

Borkovits, T., Rappaport, S. A., Hajdu, T., et al. 2020, MNRAS, doi: 10.1093/mnras/staa495

Calvet, N., & Hartmann, L. 1992, ApJ, 386, 239, doi: 10.1086/171010

Calvet, N., Patino, A., Magris, G. C., & D'Alessio, P. 1991, ApJ, 380, 617, doi: 10.1086/170618

Carr, J. S. 1989, ApJ, 345, 522, doi: 10.1086/167927

Carr, J. S., Tokunaga, A. T., Najita, J., Shu, F. H., & Glassgold, A. E. 1993, in American Astronomical Society Meeting Abstracts, Vol. 181, American Astronomical Society Meeting Abstracts #181, 116.05

Chandler, C. J., Carlstrom, J. E., Scoville, N. Z., Dent, W. R. F., & Geballe, T. R. 1993, ApJ, 412, L71, doi: 10.1086/186943

Connelley, M. S., & Greene, T. P. 2010, AJ, 140, 1214, doi: 10.1088/0004-6256/140/5/1214

Contreras Peña, C., Lucas, P. W., Kurtev, R., et al. 2017, MNRAS, 465, 3039, doi: 10.1093/mnras/stw2802

Coronado, J., Hełminiak, K. G., Vanzi, L., et al. 2015, Monthly Notices of the Royal Astronomical Society, 448, 1937, doi: 10.1093/mnras/stv010

Corporon, P., Lagrange, A. M., & Beust, H. 1996, A&A, 310, 228

Covey, K. R., Greene, T. P., Doppmann, G. W., & Lada, C. J. 2005, AJ, 129, 2765, doi: 10.1086/429736

Czekala, I., Andrews, S. M., Torres, G., et al. 2017, ApJ, 851, 132, doi: 10.3847/1538-4357/aa9be7

Davis, C. J., Scholz, P., Lucas, P., Smith, M. D., & Adamson, A. 2008, MNRAS, 387, 954, doi: 10.1111/j.1365-2966.2008.13247.x

Deacon, N. R., Liu, M. C., Magnier, E. A., et al. 2014, ApJ, 792, 119, doi: 10.1088/0004-637X/792/2/119

Doppmann, G. W., Greene, T. P., Covey, K. R., & Lada, C. J. 2005, AJ, 130, 1145, doi: 10.1086/431954

Dunham, M. M., Stutz, A. M., Allen, L. E., et al. 2014, in Protostars and Planets VI, ed. H. Beuther, R. S. Klessen, C. P. Dullemond, & T. Henning, 195

Dunham, M. M., Allen, L. E., Evans, Neal J., I., et al. 2015, ApJS, 220, 11, doi: 10.1088/0067-0049/220/1/11

Durisen, R. H., Yang, S., Cassen, P., & Stahler, S. W. 1989, ApJ, 345, 959, doi: 10.1086/167965

Eggleton, P. P., & Kiseleva—Eggleton, L. 2001, The Astrophysical Journal, 562, 1012, doi: 10.1086/323843

Enoch, M. L., Young, K. E., Glenn, J., et al. 2006, ApJ, 638, 293, doi: 10.1086/498678

Evans, D. F. 2018, Research Notes of the American Astronomical Society, 2, 20, doi: 10.3847/2515-5172/aac173

Evans, D. W., Riello, M., De Angeli, F., et al. 2018, A&A, 616, A4, doi: 10.1051/0004-6361/201832756

Evans, Neal J., I., Dunham, M. M., Jørgensen, J. K., et al. 2009, ApJS, 181, 321, doi: 10.1088/0067-0049/181/2/321

Fazio, G. G., Hora, J. L., Allen, L. E., et al. 2004, ApJS, 154, 10, doi: 10.1086/422843

Fedriani, R., Caratti o Garatti, A., Koutoulaki, M., et al. 2020, A&A, 633, A128, doi: 10.1051/0004-6361/201936748

Fiorellino, E., Manara, C. F., Nisini, B., et al. 2021, arXiv e-prints, arXiv:2103.03863. https://arxiv.org/abs/2103.03863

Folha, D. F. M., & Emerson, J. P. 2001, A&A, 365, 90, doi: 10.1051/0004-6361:20000018

Fuhrmann, K., Chini, R., Kaderhandt, L., & Chen, Z. 2017, The Astrophysical Journal, 836, 139, doi: 10.3847/1538-4357/836/1/139

Furlan, E., Fischer, W. J., Ali, B., et al. 2016, ApJS, 224, 5, doi: 10.3847/0067-0049/224/1/5

Geballe, T. R., & Persson, S. E. 1987, ApJ, 312, 297, doi: 10.1086/164873

Getman, K. V., Broos, P. S., Kuhn, M. A., et al. 2017, ApJS, 229, 28, doi: 10.3847/1538-4365/229/2/28

Gomez Gonzalez, C. A., Wertz, O., Absil, O., et al. 2017, AJ, 154, 7, doi: 10.3847/1538-3881/aa73d7

Gómez Maqueo Chew, Y., Hebb, L., Stempels, H. C., et al. 2019, Astronomy & Astrophysics, 623, A23, doi: 10.1051/0004-6361/201833299

Gredel, R., & Dalgarno, A. 1995, ApJ, 446, 852, doi: 10.1086/175843

Greene, T. P., Barsony, M., & Weintraub, D. A. 2010, ApJ, 725, 1100, doi: 10.1088/0004-637X/725/1/1100

Greene, T. P., Gully-Santiago, M. A., & Barsony, M. 2018, ApJ, 862, 85, doi: 10.3847/1538-4357/aacc6c

Greene, T. P., & Lada, C. J. 2002, AJ, 124, 2185, doi: 10.1086/342861

Grosso, N., Hamaguchi, K., Principe, D. A., & Kastner, J. H. 2020, A&A, 638, L4, doi: 10.1051/0004-6361/202038185

Guerrero, C. A., Orlov, V. G., Monroy-Rodríguez, M. A., & Borges Fernandes, M. 2015, AJ, 150, 16, doi: 10.1088/0004-6256/150/1/16

Hartmann, L., Herczeg, G., & Calvet, N. 2016, ARA&A, 54, 135, doi: 10.1146/annurev-astro-081915-023347

Hartmann, L., Hewett, R., & Calvet, N. 1994, ApJ, 426, 669, doi: 10.1086/174104

Hillenbrand, L. A., Zhang, C., Riddle, R. L., et al. 2018, The Astronomical Journal, 155, 51, doi: 10.3847/1538-3881/aaa01e

Horch, E. P., van Belle, G. T., Davidson, James W., J., et al. 2015, AJ, 150, 151, doi: 10.1088/0004-6256/150/5/151

Houck, J. R., Roellig, T. L., van Cleve, J., et al. 2004, ApJS, 154, 18, doi: 10.1086/423134

Husser, T. O., Wende-von Berg, S., Dreizler, S., et al. 2013, A&A, 553, A6, doi: 10.1051/0004-6361/201219058

Jensen-Clem, R., Duev, D. A., Riddle, R., et al. 2017, The Astronomical Journal, 155, 32, doi: 10.3847/1538-3881/aa9be6

Jiménez-Esteban, F. M., Solano, E., & Rodrigo, C. 2019, AJ, 157, 78, doi: 10.3847/1538-3881/aafacc

Johns-Krull, C. M. 2007, ApJ, 664, 975, doi: 10.1086/519017

Johns-Krull, C. M., Greene, T. P., Doppmann, G. W., & Covey, K. R. 2009, ApJ, 700, 1440, doi: 10.1088/0004-637X/700/2/1440

Jørgensen, J. K., van Dishoeck, E. F., Visser, R., et al. 2009, A&A, 507, 861, doi: 10.1051/0004-6361/200912325

Kellogg, K., Prato, L., Torres, G., et al. 2017, ApJ, 844, 168, doi: 10.3847/1538-4357/aa7c60

Kim, S.-H., Martin, P. G., & Hendry, P. D. 1994, ApJ, 422, 164, doi: 10.1086/173714

Kirk, H., Johnstone, D., & Di Francesco, J. 2006, ApJ, 646, 1009, doi: 10.1086/503193

Knapp, W., & Nanson, J. 2018, Journal of Double Star Observations, 14, 503

Kounkel, M., & Covey, K. 2019, AJ, 158, 122, doi: 10.3847/1538-3881/ab339a

Kounkel, M., Hartmann, L., Loinard, L., et al. 2017, ApJ, 834, 142, doi: 10.3847/1538-4357/834/2/142

Kounkel, M., Covey, K., Moe, M., et al. 2019, The Astronomical Journal, 157, 196, doi: 10.3847/1538-3881/ab13b1

Kristensen, L. E., Ravkilde, T. L., Field, D., Lemaire, J. L., & Pineau Des Forêts, G. 2007, A&A, 469, 561, doi: 10.1051/0004-6361:20065786

Kryukova, E., Megeath, S. T., Gutermuth, R. A., et al. 2012, AJ, 144, 31, doi: 10.1088/0004-6256/144/2/31

Lafrenière, D., Marois, C., Doyon, R., & Barman, T. 2009, ApJ, 694, L148, doi: 10.1088/0004-637X/694/2/L148

Laos, S., Stassun, K. G., & Mathieu, R. D. 2020, ApJ, 902, 107, doi: 10.3847/1538-4357/abb3fe

Law, N. M., Morton, T., Baranec, C., et al. 2014, The Astrophysical Journal, 791, 35, doi: 10.1088/0004-637X/791/1/35

Lawrence, A., Warren, S. J., Almaini, O., et al. 2007, MNRAS, 379, 1599, doi: 10.1111/j.1365-2966.2007.12040.x

Lee, K. I., Dunham, M. M., Myers, P. C., et al. 2016, ApJ, 820, L2, doi: 10.3847/2041-8205/820/1/L2

Lindegren, L. 2018, in IAU Symposium, Vol. 330, Astrometry and Astrophysics in the Gaia Sky, ed. A. Recio-Blanco, P. de Laverny, A. G. A. Brown, & T. Prusti, 41–48

Maíz Apellániz, J., & Weiler, M. 2018, A&A, 619, A180, doi: 10.1051/0004-6361/201834051

Mardling, R. A., & Aarseth, S. J. 2001, Monthly Notices of the Royal Astronomical Society, 321, 398, doi: 10.1046/j.1365-8711.2001.03974.x

Matijevič, G., Prša, A., Orosz, J. A., et al. 2012, The Astronomical Journal, 143, 123, doi: 10.1088/0004-6256/143/5/123

Maury, A. J., André, P., Hennebelle, P., et al. 2010, A&A, 512, A40, doi: 10.1051/0004-6361/200913492

Maury, A. J., André, P., Testi, L., et al. 2019, A&A, 621, A76, doi: 10.1051/0004-6361/201833537

McAlister, H. A., Hartkopf, W. I., Hutter, D. J., & Franz, O. G. 1987, AJ, 93, 688, doi: 10.1086/114353

Mclean, I., Steidel, C., Epps, H., et al. 2012, Proc. SPIE, 8446, doi: 10.1117/12.924794

McLean, I. S., Steidel, C. C., Epps, H., et al. 2010, in Ground-based and Airborne Instrumentation for Astronomy III, ed. I. S. McLean, S. K. Ramsay, & H. Takami, Vol. 7735, International Society for Optics and Photonics (SPIE), 568 – 579. https://doi.org/10.1117/12.856715

Megeath, S. T., Gutermuth, R., Muzerolle, J., et al. 2012, AJ, 144, 192, doi: 10.1088/0004-6256/144/6/192

Moe, M., & Kratter, K. M. 2018, The Astrophysical Journal, 854, 44, doi: 10.3847/1538-4357/aaa6d2

Morales-Calderón, M., Stauffer, J. R., Hillenbrand , L. A., et al. 2011, ApJ, 733, 50, doi: 10.1088/0004-637X/733/1/50

Muzerolle, J., Calvet, N., & Hartmann, L. 1998, ApJ, 492, 743, doi: 10.1086/305069

Nagy, Z., Menechella, A., Megeath, S. T., et al. 2020, A&A, 642, A137, doi: 10.1051/0004-6361/201937342

Najita, J., Carr, J. S., Glassgold, A. E., Shu, F. H., & Tokunaga, A. T. 1996a, ApJ, 462, 919, doi: 10.1086/177205

Najita, J., Carr, J. S., & Tokunaga, A. T. 1996b, ApJ, 456, 292, doi: 10.1086/176649

Poglitsch, A., Waelkens, C., Geis, N., et al. 2010, A&A, 518, L2, doi: 10.1051/0004-6361/201014535

Prochaska, J. X., Hennawi, J. F., Westfall, K. B., et al. 2020, arXiv e-prints, arXiv:2005.06505. https://arxiv.org/abs/2005.06505

Prša, A., Guinan, E. F., Devinney, E. J., et al. 2008, The Astrophysical Journal, 687, 542, doi: 10.1086/591783

Raghavan, D., McAlister, H. A., Henry, T. J., et al. 2010, The Astrophysical Journal Supplement Series, 190, 1, doi: 10.1088/0067-0049/190/1/1

Rebull, L. M. 2015, AJ, 150, 17, doi: 10.1088/0004-6256/150/1/17

Reipurth, B., & Mikkola, S. 2012, Nature, 492, 221, doi: 10.1038/nature11662

Riddle, R. L., Tokovinin, A., Mason, B. D., et al. 2015, The Astrophysical Journal, 799, 4, doi: 10.1088/0004-637X/799/1/4

Rieke, G. H., Young, E. T., Engelbracht, C. W., et al. 2004, ApJS, 154, 25, doi: 10.1086/422717

Roberts, L. C., & Mason, B. D. 2018, MNRAS, 473, 4497, doi: 10.1093/mnras/stx2559

Robitaille, T. P., Whitney, B. A., Indebetouw, R., & Wood, K. 2007, ApJS, 169, 328, doi: 10.1086/512039

Robitaille, T. P., Whitney, B. A., Indebetouw, R., Wood, K., & Denzmore, P. 2006, ApJS, 167, 256, doi: 10.1086/508424

Romanova, M. M., Ustyugova, G. V., Koldoba, A. V., & Lovelace, R. V. E. 2012, MNRAS, 421, 63, doi: 10.1111/j.1365-2966.2011.20055.x

Rucinski, S. M., Pribulla, T., & van Kerkwijk, M. H. 2007, The Astronomical Journal, 134, 2353, doi: 10.1086/523353

Sana, H., Le Bouquin, J.-B., Lacour, S., et al. 2014, The Astrophysical Journal Supplement Series, 215, 15, doi: 10.1088/0067-0049/215/1/15

Sandell, G., & Knee, L. B. G. 2001, ApJ, 546, L49, doi: 10.1086/318060

Schaefer, G. H., Prato, L., Simon, M., & Zavala, R. T. 2012, ApJ, 756, 120, doi: 10.1088/0004-637X/756/2/120

Segura-Cox, D. M., Looney, L. W., Tobin, J. J., et al. 2018, ApJ, 866, 161, doi: 10.3847/1538-4357/aaddf3

Shu, F., Najita, J., Ostriker, E., et al. 1994, ApJ, 429, 781, doi: 10.1086/174363

Shu, F. H., Lizano, S., Ruden, S. P., & Najita, J. 1988, ApJ, 328, L19, doi: 10.1086/185152

Shu, F. H., Najita, J., Ostriker, E. C., & Shang, H. 1995, ApJ, 455, L155, doi: 10.1086/309838

Siringo, G., Kreysa, E., Kovács, A., et al. 2009, A&A, 497, 945, doi: 10.1051/0004-6361/200811454

Siringo, G., Kreysa, E., De Breuck, C., et al. 2010, The Messenger, 139, 20

Skrutskie, M. F., Cutri, R. M., Stiening, R., et al. 2006, AJ, 131, 1163, doi: 10.1086/498708

Soummer, R., Pueyo, L., & Larkin, J. 2012, ApJ, 755, L28, doi: 10.1088/2041-8205/755/2/L28

Southworth, J. 2015, DEBCat: A Catalog of Detached Eclipsing Binary Stars

Stassun, K. G., Ardila, D. R., Barsony, M., Basri, G., & Mathieu, R. D. 2004, AJ, 127, 3537, doi: 10.1086/420989

Stassun, K. G., Feiden, G. A., & Torres, G. 2014, New Astronomy Reviews, 60-61, 1, doi: 10.1016/j.newar.2014.06.001

Stassun, K. G., & Torres, G. 2016, AJ, 152, 180, doi: 10.3847/0004-6256/152/6/180

Stephens, I. W., Dunham, M. M., Myers, P. C., et al. 2017, ApJ, 846, 16, doi: 10.3847/1538-4357/aa8262

Stephens, I. W., Bourke, T. L., Dunham, M. M., et al. 2019, ApJS, 245, 21, doi: 10.3847/1538-4365/ab5181

Stutz, A. M., Tobin, J. J., Stanke, T., et al. 2013, ApJ, 767, 36, doi: 10.1088/0004-637X/767/1/36

Tobin, J. J., Hartmann, L., Chiang, H.-F., et al. 2012, Nature, 492, 83, doi: 10.1038/nature11610

Tobin, J. J., Chandler, C. J., Wilner, D. J., et al. 2013, ApJ, 779, 93, doi: 10.1088/0004-637X/779/2/93

Tobin, J. J., Looney, L. W., Li, Z.-Y., et al. 2018, ApJ, 867, 43, doi: 10.3847/1538-4357/aae1f7

Tobin, J. J., Sheehan, P. D., Megeath, S. T., et al. 2020, ApJ, 890, 130, doi: 10.3847/1538-4357/ab6f64

Tokovinin, A. 2014a, AJ, 147, 86, doi: 10.1088/0004-6256/147/4/86

—. 2014b, AJ, 147, 87, doi: 10.1088/0004-6256/147/4/87

Tokovinin, A. 2018, The Astrophysical Journal Supplement Series, 235, 6, doi: 10.3847/1538-4365/aaa1a5

Tokovinin, A., Thomas, S., Sterzik, M., & Udry, S. 2006, Astronomy & Astrophysics, 450, 681, doi: 10.1051/0004-6361:20054427

Torres, G., Andersen, J., & Giménez, A. 2010, The Astronomy and Astrophysics Review, 18, 67, doi: 10.1007/s00159-009-0025-1

Troup, N. W., Nidever, D. L., Lee, N. D., et al. 2016, The Astronomical Journal, 151, 85, doi: 10.3847/0004-6256/151/3/85

Wang, S., Liu, J., Qiu, Y., et al. 2016, ApJS, 224, 40, doi: 10.3847/0067-0049/224/2/40

Wilgenbus, D., Cabrit, S., Pineau des Forêts, G., & Flower, D. R. 2000, A&A, 356, 1010

Woollands, R. M., Pollard, K. R., Ramm, D. J., Wright, D. J., & Böhm, T. 2013, MNRAS, 432, 327, doi: 10.1093/mnras/stt468

Ziegler, C., Law, N. M., Morton, T., et al. 2017, The Astronomical Journal, 153, 66, doi: 10.3847/1538-3881/153/2/66

Ziegler, C., Law, N. M., Baranec, C., et al. 2018, AJ, 155, 161, doi: 10.3847/1538-3881/aab042